ADAPTIVE ACQUISITION TECHNIQUES FOR SPHERICAL NEAR-FIELD ANTENNA MEASUREMENTS

by

Vincent Beaulé

A thesis submitted to the Faculty of Graduate and Postdoctoral Studies

In partial fulfillment of the requirements for the degree of

Master of Applied Science (M.A.Sc.) in Electrical Engineering

Ottawa-Carleton Institute for Electrical and Computer Engineering

School of Electrical Engineering and Computer Science

Faculty of Engineering

University of Ottawa

Abstract

This thesis presents a practical approach to reduce the overall testing time in a spherical near-field (SNF) antenna measurement environment. The premise of this work is that the acquisition time is mostly dominated by the mechanical movement and the processing electronic. Moreover, it is assumed that the transformation time to go from the near-field domain to the far-field domain (NF-FF transform) is small compared to the acquisition time. Thus this operation can be done repeatedly while the acquisition is on-going without significantly affecting the overall test time.

This situation allows to continuously evaluate the far-field (FF) of the antenna under test (AUT), so that certain decision functions based on the radiation pattern of the antenna can be monitored. Such decision functions are based on the antenna specification, such as the gain, the side lobe level, etc.

We do not proceed with a complete scan of the measurement sphere but effectively allow the probe to follow a directed path under control of an acquisition rule, so that the sampled near-field (NF) datapoints constitute an acquisition map on the sphere. The acquisition can then be terminated based on decision function values, allowing the smallest amount of data needed to ensure accurate determination of the AUT performance measures.

Acknowledgements

No work of this sort can be created from vacuum; I therefore cannot let this opportunity pass without expressing my deep obligations to the generous assistance which I have received from my supervisors Dr. D.A. McNamara and Prof. D.J.V. Rensburg, as well as from Dr. L. Shafai at the Canadian Space Agency (CSA-DFL). Derek, the rigor, the knowledge and the patience you provided at each of our encounter does, I hope, reflect in this work. Daniel, the wisdom and the experience you have acquired in the antenna measurement domain, and now share, was invaluable to conduct this research. Leili, thanks for the support and the latitude you have provided for our work to take place and expand. To all three, I sincerely thank you for the role you played to shape this work. I am very proud of that small drop this work is adding to the pool of knowledge.

À ma femme Caroline et notre garçon Xavier, merci d'avoir été aussi patients; les longs soirs et les fins de semaine partagés entre vous et l'Université est maintenant chose du passé. Ce travail d'envergure m'a fait grandir, maintenant c'est à moi de vous rendre la pareille.

BEAR IN MIND THAT THE WONDERFUL THINGS YOU LEARN IN YOUR SCHOOLS ARE THE WORK OF MANY GENERATIONS, PRODUCED BY ENTHUSIASTIC EFFORT AND INFINITE LABOR IN EVERY COUNTRY OF THE WORLD. ALL THIS IS PUT INTO YOUR HANDS AS YOUR INHERITANCE IN ORDER THAT YOU MAY RECEIVE IT, HONOR IT, ADD TO IT, AND ONE DAY FAITHFULLY HAND IT ON TO YOUR CHILDREN. THUS DO WE MORTALS ACHIEVE IMMORTALITY IN THE PERMANENT THINGS WHICH WE CREATE IN COMMON.

IF YOU ALWAYS KEEP THAT IN MIND YOU WILL FIND A MEANING IN LIFE AND WORK AND ACQUIRE THE RIGHT ATTITUDE TOWARD OTHER NATIONS AND AGES.

A. Einstein – 1934

Publications

V. Beaulé, D.A. McNamara, D.J.V. Rensburg, L. Shafai & S. Mishra, “Exploration of the Feasibility of Adaptive Spherical Near-field Antenna Measurements”, in Proc. Antenna Measurement Techniques Association Conf. (ATMA), Seattle, USA, Oct. 2012

V. Beaulé, D.A. McNamara, D.J.V. Rensburg & L. Shafai, “Exploration of the Feasibility of Adaptive Spherical Near-Field Antenna Measurements – Part II”, in Proc. Antenna Measurement Techniques Association Conf. (ATMA), Columbus, USA, Oct. 2013

Table of Contents

List of Figures

Chapter 1 – Introduction

As antenna performance complexity increases, so does the suite of measurements that is needed to confirm whether a given antenna satisfies the required performance. Such more elaborate testing implies that these measurements will be more time-consuming. Test time in an antenna measurement facility is a precious resource since the number of such facilities is usually limited in any organisation. It is important to realize that it is not the speed with which electronic instrumentation is able to operate that is of concern. When it comes to antenna testing this aspect occupies only a small portion of the time involved. Rather, it is the acquisition time related to the three-dimensional movement of the antenna under test (AUT), or the acquisition probe, during measurement that is the main contributor. The aim of this research is to explore a method for reducing the data capture burden in antenna spherical near-field (SNF) measurements. With modern desktop computers, the far-zone field computation time is negligible compared to the data acquisition time even if such computation is done repeatedly (while data is being acquired). This fact does not yet appear to have been exploited. We propose that such computations be used as part of an adaptive algorithm intent on reducing the amount of data that has to be acquired, and hence the overall antenna testing time. This work represents a step towards building feedback/adaptivity into SNF measurements. The goal is to have such techniques allow us to reduce test times by only acquiring those SNF data sets actually needed to ensure that the quantities being sought are within the accuracy we require, no more and no less.

Initial work on these concepts has been described in [Beau 12] and [Beau 13]. The present thesis describes the examination of these ideas in simulation, in physical implementation, and the conclusions reached.

Chapter 2 provides a brief review of near-field measurements with a particular emphasis on the SNF type, which is the topic of this thesis. We describe the planar near-field measurement (PNF), the cylindrical near-field measurement (CNF) and the spherical near-field measurement (SNF) techniques. This helps to put into perspective the work done in this thesis.

Chapter 3 explores the fundamentals of SNF measurements that are required to set the basis of the adaptive acquisition. We start by exploring the acquisition process on the spherical measurement surface. Next the computation of the near-field to the far-field (NF-FF) transformation is explained. We then review approaches that use only a portion of the measurement sphere. Rather than the complete one.

In Chapter 4 we lay the concepts needed for the adaptive algorithm. The intended schema is presented and we define the acquisition rule and decision function ideas.

Chapter 5 presents the plan to study adaptive SNF methods. Section 5.2 outlines the simulation software that is required to assess the concepts proposed in Chapter4. Then the acquisition rules devised, and the decision functions defined, are detailed in Section 5.3 and 5.4, respectively. At the end of this chapter we present the concept of NF pre-conditioning. This helps to settle some parameters faster during operation of the adaptive SNF approach.

Chapter 6 presents the outcome of simulation done on the various acquisition rules, decision functions and pre-conditioning functions devised in Chapter 5. These results are then used for the realisation of a practical implementation of the adaptive SNF acquisition method.

General conclusions are reached in Chapter 7 to summarize the contribution this work brings to the SNF measurement domain, and direct the path of some future works.

Chapter 2 – Near-field Measurement Fundamentals

The measurement of antenna characteristics continues be a topic of importance. A large body of literature on this topic is available (e.g. [Bala 05], [Vola 07], [Stut 97], [Appe 86]). There are two broad classes of antenna measurement techniques - far-field (FF) and near-field (NF). Both approaches are used to determine the far-field characteristics of an antenna. Note that in general it is preferable to measure the electric field rather than the magnetic field since suitable probes are available.

Far-field techniques, being historically the first type of measurements to be performed, require the antenna under test (AUT) and the acquisition probe to be separated by a sufficiently large distance. That is, the incoming wave front must appear locally as a plane wave to the probe. No transformation is required for these types of measurement; one directly obtains the far-field characteristics as the transmit antenna and the receive antenna are both in each other's far-zone.

Near-field measurement techniques use a probe that is located much closer to the antenna, in its radiating near-field. Formulations based on fundamental electromagnetic (EM) theory are then used to predict the far-field radiation from the field value acquired in the near vicinity of the AUT.

NF techniques themselves can be divided into three sub-classes: planar near-field techniques (PNF), cylindrical near-field techniques (CNF) and spherical near-field techniques (SNF). These classes refer to the respective surface on which the acquisition probe samples near-field data. In the 1960's D.M.Kerns of the National Bureau of Standards[1] in the United States published work toward developing what is known as free-space scattering matrix theory [Kern 60]. His work serves as a theoretical basis for near-field antenna measurements. In essence, scattering matrix theory allows one to represent the field transmitted by a particular AUT in terms of a spectrum of waves. These wave spectrums can take many forms:

- Plane waves, used in planar near-field (PNF) measurements
- Cylindrical waves/modes for cylindrical near-field (CNF) measurements
- Spherical waves/modes for spherical near-field (SNF) measurements.

[1] Now called NIST

Use of the scattering matrix theory allows one to measure the radiation of an AUT in the near-field region and perform a transformation the near-field to far-field, or NF-FF, transformation to obtain the resulting far-field patterns. Measurements are performed on a near-field scan surface; the geometry of the scan surface depends on the near-field technique class. After many years of development and industry evaluation, near-field testing has become the preferred approach for characterizing antennas for a broad range of frequencies. These systems are capable of measuring side lobes as low as 50 dB down from the pattern peak and can provide sub-milliradian alignment accuracies [NSI 06]. The different types of near-field systems each have their strengths and weaknesses, as outlined below.

While near-field techniques may in the past have seemed less appealing because of the computational burden of the NF-FF transformation processing step, the latter is no longer a problem issue. Furthermore, repeatability and quality control arguments play in favor of near-field techniques as well. FF techniques are subject to environmental constraints and require a large physical deployment. The setup required to perform NF measurements usually can occur in much smaller facilities, and thus, in a controlled environment.

Since the present work is on SNF measurements, most of the content of the rest of this chapter (and the next) is devoted to this type of NF measurement. However, to place it into perspective, the following sections present an overview of the three classes of NF measurement.

2.1.1. Planar Near-Field (PNF) Measurements

PNF measurements were the first of the near-field measurement geometries to become commonplace in industry. In a PNF scan, the field measuring probe will typically measure field values at specified positions along an XY grid, while the AUT is placed at a fixed measurement distance from the probe along the z-axis. A sketch of this measurement geometry, along with a typical probe scan pattern is shown in Figure 1. In this figure, the probe measures the field at several points along a line in Y, a vertical cut, before stepping to the next position in X and repeating the vertical cut. Once vertical cuts have been completed for all positions in X, the full set of near-field data can be transformed to the far-field using plane wave spectrum theory.

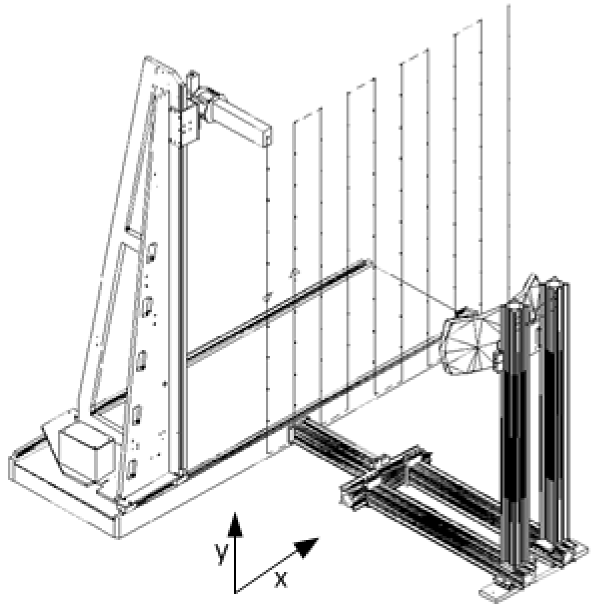

FIGURE 1 - TYPICAL PLANAR NEAR-FIELD MEASUREMENT SYSTEM (AFTER [NSI 06])

Rigorous electromagnetic theory [Bala 12, Section 7.8], namely the surface equivalence principle, indicates that a fundamental requirement is that the measurement surface must completely enclose the AUT. In a PNF measurement, the term “closed measurement surface” implies that the scan plane be infinitely long in both X and Y. However, since this is clearly not practical in a measurement system, one must use a finite scan plane sufficiently large to capture most of the AUT’s radiated energy. Since low gain antennas tend to radiate broadly, in practice one finds that PNF systems are best suited for antennas with a directivity of 15 dBi or greater. One understands easily that this figure is a function of the possible scan size and must only be used as a “rule of the thumb”. The measurement speed and low system cost make the PNF system an appropriate option for a wide range of problems, provided the AUT has sufficiently high directivity.

2.1.2. Cylindrical Near-Field (CNF) Measurements

Similar to a PNF measurement, the CNF range allows fields to be measured over an open measurement surface in the AUT’s near-field region. Figure 2 shows a typical CNF measurement geometry and cylindrical scan surface. The AUT is mounted on top of an azimuth-axis rotator at the center of this scan surface and the probe is translated along the Y-axis for a full vertical cut. Next, the AUT is rotated in azimuth by a specified amount and the probe performs a second vertical cut. Once vertical cuts have been completed for all azimuth positions, cylindrical wave mode theory can be used to transform the near-field grid data to the far-field. Again, since an open measurement window was used, only antennas with very little energy radiating in the regions not enclosed by the measurement surface should be considered for CNF scans, such as base station antennas.

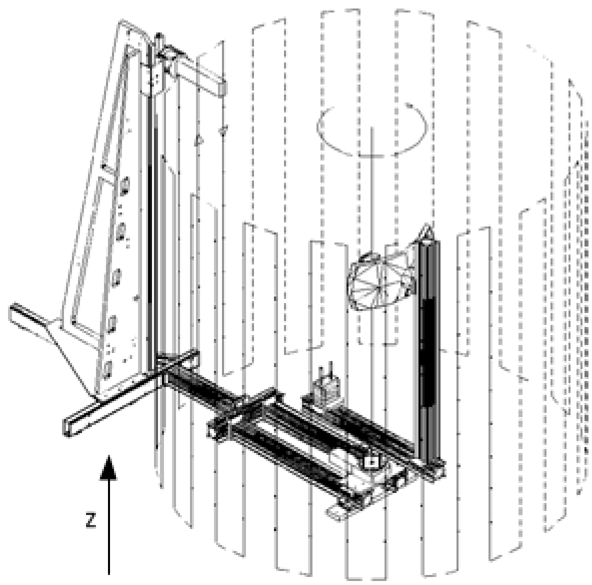

FIGURE 2 - TYPICAL CYLINDRICAL NEAR-FIELD MEASUREMENT SYSTEM (AFTER [NSI 06])

2.1.3. Spherical Near-Field (SNF) Measurements

The SNF geometry is of special interest at this point, since the whole of this thesis is primarily involved in the development of adaptive techniques for this type of near-field system. While there are various ways of mechanically implementing SNF scanning, the fundamental requirement is that data be acquired on a spherical surface enclosing the AUT. A typical SNF system is shown in Figure 3. The AUT can be seen at the origin of the measurement sphere, mounted on two separate positioners. Together, these positioners must allow the AUT to rotate in such a way that the probe can record field values over the entire measurement sphere. For the measurement geometry depicted in Figure 3, the AUT will first perform a complete azimuth cut (about the θ-axis). In other words, the AUT, along with the entire structure that the AUT is mounted on, will rotate a full 360˚ and return to its starting position. Next, the AUT will rotate a specified amount in ϕ and repeat the 360˚ azimuth cut. Once azimuth cuts have been completed for all ϕ positions, spherical wave mode theory can be used to transform the spherical near-field measured data to a far-field pattern.

Although the "scattering matrix theory" approach in [Kern 60] formed the basis of near-field testing work from the very beginning, there is a theoretical viewpoint that is perhaps more fundamental, but of course equivalent. This is the surface equivalence principle. In the form in which it is required for the present work this principle states that if one is able to measure the tangential electric and magnetic fields over any closed surface *S* surrounding the AUT (assumed to be transmitting), these can very simply be converted into equivalent electric and magnetic current densities over *S*. These radiate in free space and so can be used with the free space Green's function to determine the radiated fields of the AUT. In SNF measurements surface *S* is chosen to be a sphere. We in fact need to measure the tangential electric field only; we are still able to find the far-field patterns through use of a spherical wave expansion form of the free space Green's function. Knowing both the scattering matrix theory and surface equivalence viewpoints is important since some newer near-to-far field transformations adopt an approach that is more easily understood via the surface equivalence principle.

This type of near-field system has several advantages over conventional far-field, PNF and CNF systems. The spherical near-field (SNF) antenna measurement system is the only one for which the scanning surface is actually completely closed, and for which there is thus no inherent truncation error. Therefore SNF measurements can be used for any antenna type. Because of this, the SNF system can more universally meet different types of antenna measurement requirements, namely low and medium gain antennas whose patterns are broad, as well as high gain antennas. These systems provide the best side lobe measurement performance since fields are measured in all directions, with the exception of the mounting structure blocking the AUT's backward radiation.

Finally, probe compensation[2] is far less critical with SNF because at any point on the scanning surface the probe is always pointed directly toward the AUT.

Since this technique is of prime importance for this work, the next chapter is devoted to the elaboration of SNF fundamentals and its various computational aspects.

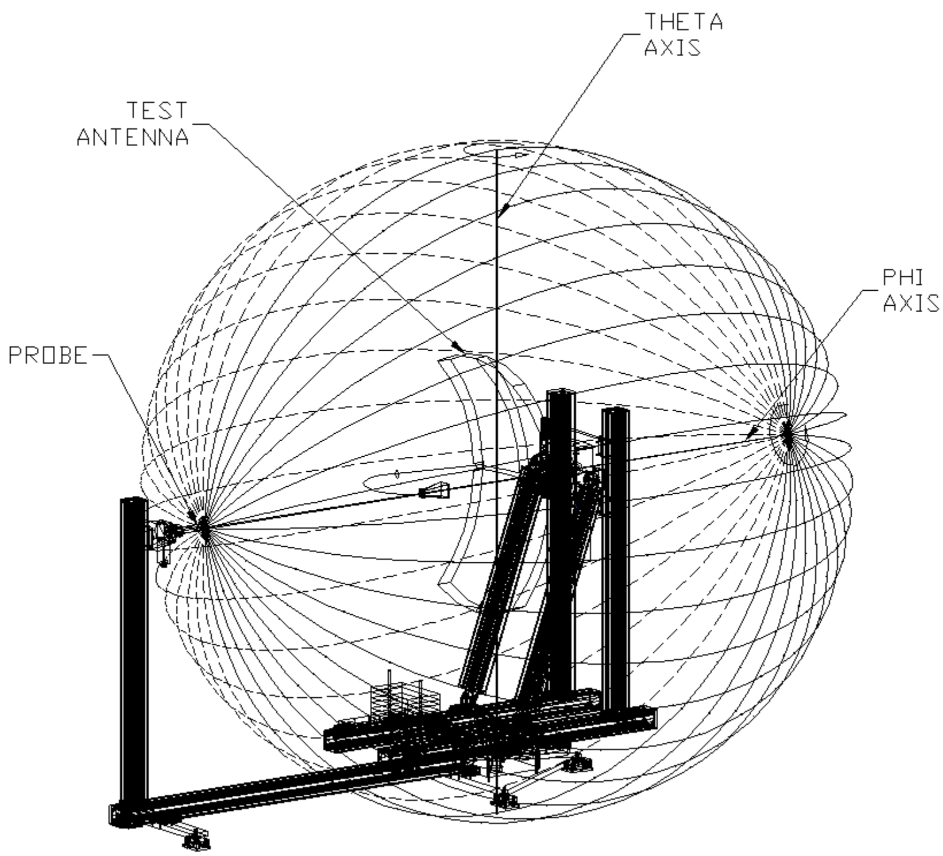

FIGURE 3 - TYPICAL SPHERICAL NEAR-FIELD MEASUREMENT SYSTEM (AFTER [NSI 06])

[2] A technique that accounts for the probe pattern in the measurement of the fields. We do not measure the fields at a single point, but rather on region shaped by the probe's radiation pattern [Paris 78]

Chapter 3 – Spherical Near-field Fundamentals and Computational Aspects

3.1 - SWE Fundamentals Applied to SNF Measurements

The details underlying the description provided in this chapter are given in Appendix A – Spherical Wave Expansion (SWE) Fundamentals. In this chapter only those expressions needed a "user's" point of view – which is the viewpoint of the chapter - are presented.

A given AUT has a sphere of minimum radius that is able to completely enclose it. As the AUT size increases so does the radius of the minimum sphere. This is accompanied by an increase in the number of spherical harmonics (N) needed[3] to represent the field. As an empirical rule [Hans 88, pp.21], the number of meaningful modes are determined using

$$N = k\rho_0 + n_1 \tag{3.1}$$

where k is the wavenumber, ρ_0 the radius of the minimum sphere enclosing the antenna, and n_1 an integer factor based on the location of the AUT in the coordinate system and the accuracy required. The total number of modes required is

$$2N(N+2) \tag{3.2}$$

Historically n_1 was usually set equal to 10, or in some cases to $(k\rho_0)^{1/3}$, which was related to the computing power available. Recent development has linked an expression of n_1 to the acceptable power truncation error [Jens 04], further details are given in Appendix A. As the number of required modes N increases, the sampling density needed to reconstruct the fields without modal aliasing increases as well. The steps in θ and ϕ needed to satisfy the sampling criteria are

$$\Delta\theta = 2\pi/(2N+1) \tag{3.3}$$

and

[3] Note that an infinite number of modes are needed to perfectly represent the fields, but only few of them carry significant power and do not decay exponentially.

$$\Delta\varphi = 2\pi/(2N+1) \tag{3.4}$$

As can be seen, if the minimum sphere is large (i.e. the AUT antenna is electrically large) the steps in θ and ϕ become small, and a large number of points must be measured.

Once the required angular separation ($\Delta\theta$, $\Delta\phi$) between sampling points has been determined, the near-field data is acquired at a pre-determined set of points on the measurement sphere enclosing the AUT. Such uniform sampling (in angle) is needed in order to apply the standard numerical processing algorithms (based on spherical wave expansions) to rapidly compute the far-zone radiation patterns of the AUT from the acquired near-field data. The problem is that this results in crowding of data points as one approaches the poles of the near-field measurement sphere. Many of these points, while being needed to apply the spherical wave expansion based near-field to far-field transformations, might be redundant from the point of view of the surface equivalence principle. Some recent advances are trying to reduce such redundancy are discussed in [Dire 12], [Bucc 03] and [Cost 11].

3.2 - SNF Antenna Measurement System Definition and Acquisition

Obviously the preferred coordinate system for spherical near-field measurement is the spherical coordinate system, as defined in Figure 4.

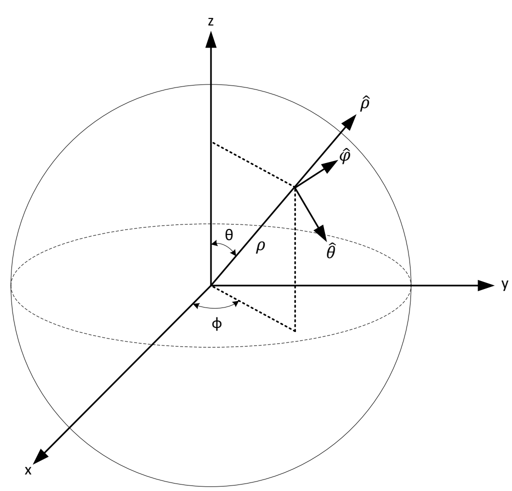

FIGURE 4 - COORDINATE SYSTEM USED FOR SNF MEASUREMENTS

Multiple ways are possible to acquire the samples on the measurement sphere, as described in what follows.

3.2.1 - 180-Phi Data Set

This refers to the resulting data set acquired using a SNF measurement where the AUT rotates 360˚ in θ but only 180˚ in ϕ. This means that the AUT will illuminate all four walls of the chamber throughout the measurement. For a 180-Phi measurement acquired with M sampling points in θ and N sampling points in ϕ, data will be measured at the following points:

$$\theta_m = -180° + (m-1)\left(\frac{360°}{M-1}\right) \quad m = 1,2,\dots,M \tag{3.5}$$

$$\varphi_n = (n-1)\left(\frac{180°}{N-1}\right) \quad n = 1,2,\dots,N \tag{3.6}$$

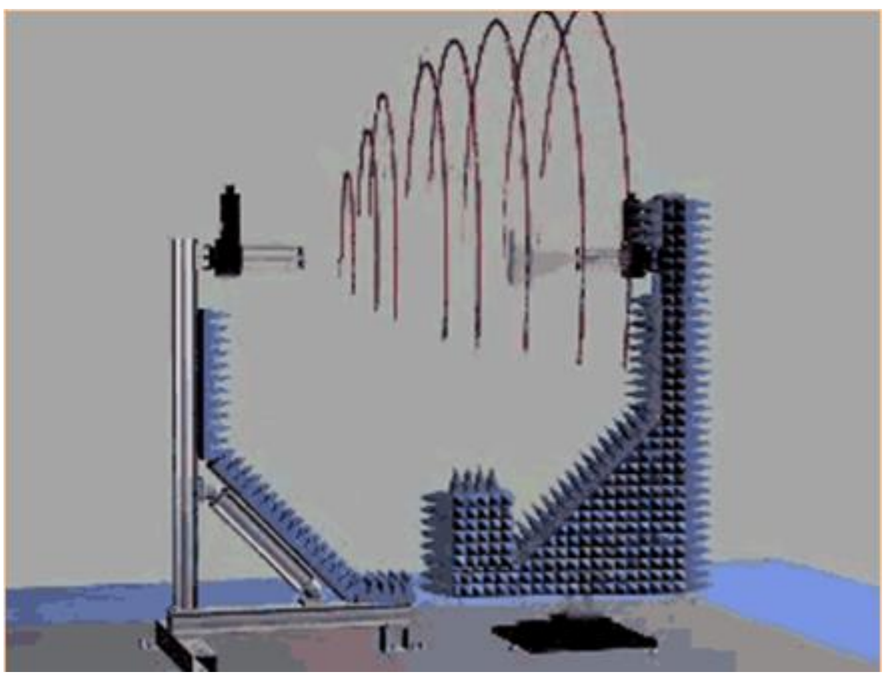

FIGURE 5 - EXAMPLE OF A 180-PHI SNF ACQUISITION (AFTER [HIND 06])

3.2.2 - 360-Phi Data Set

This refers to the resulting data set acquired using a SNF measurement where the AUT only rotates 180˚ in θ and 360˚ in ϕ. This now means that the AUT will no longer see one of the chamber's walls (the wall illuminated by the AUT at θ = 180˚). For a 360-Phi measurement acquired with M sampling points in θ and N sampling points in ϕ, data will be measured at the following points:

$$\theta_m = (m-1)\left(\frac{180°}{M-1}\right) \quad m = 1,2,\dots,M \tag{3.7}$$

$$\varphi_n = (n-1)\left(\frac{360°}{N-1}\right) \quad n = 1,2,\dots,N \tag{3.8}$$

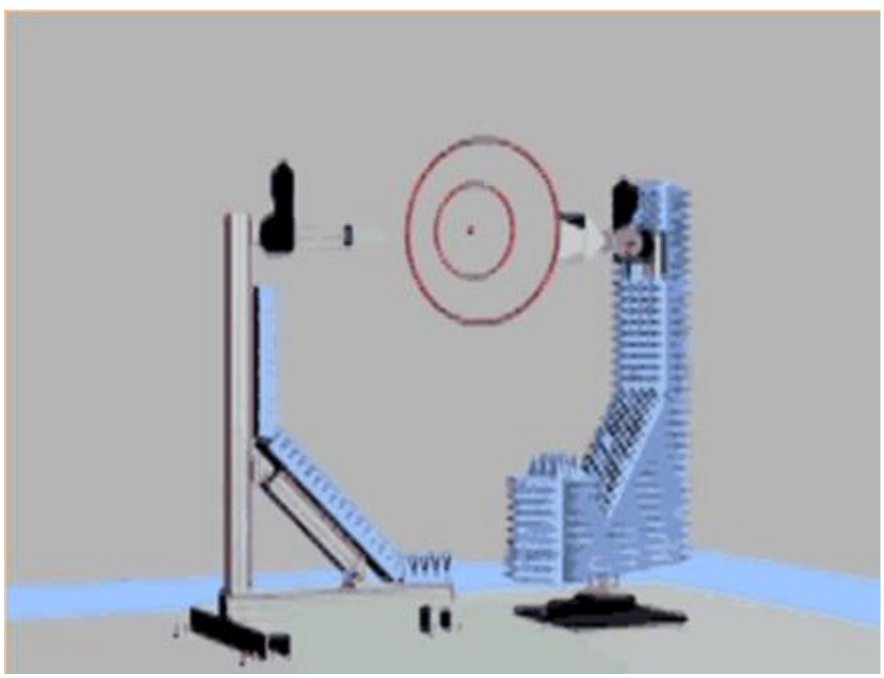

FIGURE 6 - EXAMPLE OF A 360-PHI SNF ACQUISITION (AFTER [HIND 06])

3.2.3 - Redundant Theta/Phi Data Set

In this case the resulting data set is acquired using a SNF measurement where the AUT rotates a full 360˚ in both θ and ϕ. The AUT will illuminate all 4 walls of the chamber throughout the course of the scan. Since both axes rotate a full 360˚, two complete AUT data subsets are contained within the redundant data set. For such a redundant measurement acquired with M sampling points in θ and N sampling points in ϕ, data will be measured at the following points:

$$\theta_m = -180° + (m-1)\left(\frac{360°}{M-1}\right) \quad m = 1,2,\dots,M \tag{3.9}$$

$$\varphi_n = (n-1)\left(\frac{360°}{N-1}\right) \quad n = 1,2,\dots,N \tag{3.10}$$

Averaging the two subsets (180-Phi and 360-Phi), one may acquire what is known as a "redundant theta/phi" data set.

TABLE 1: SUMMARY OF SPHERICAL NEAR-FIELD SCANNING GEOMETRIES

Terminology	Description
180-phi Scan	Measurement sphere acquired with AUT rotation of 0˚ ≤ ϕ ≤ 180˚, -180˚ ≤ θ ≤ 180˚.
360-Phi Scan	Measurement sphere acquired with AUT rotation of 0˚ ≤ ϕ ≤ 360˚, 0˚ ≤ θ ≤ 180˚.
Redundant Scan	Measurement sphere acquired with AUT rotation of 0˚ ≤ ϕ ≤ 360˚, -180˚ ≤ θ ≤ 180˚. This will produce two complete AUT data sets, which can be averaged to produce a single, redundant radiation pattern.

3.2.4 –Note on Scanning Set

While it might be confusing, one must note that scanning either in 180-phi or in 360-Phi will acquire the same sample points in space, and the same will region is scanned. The only difference is the order by which the points are acquired and displayed to the user.

One can of course find various other ways to acquire samples on the measurement sphere such as, instead of scanning in ϕ, the scan motion can be in θ. While not providing significant advantages compared to the previously discussed standard acquisition for conventional SNF measurements, such freedom in the manner in which NF data is acquired will be used extensively in this work on adaptive SNF techniques.

3.3 - Computation of SNF Near-to-Far Field Transformations

The standard approach used for NF-FF transformation in SNF testing is based on the spherical wave expansion (SWE) method. This approach is used in NSI2000[4] and discussed in Appendix A – Spherical Wave Expansion (SWE) Fundamentals. Two other approaches have also been touted in the research literature, mainly from research groups in Europe. These are the source reconstruction method (SRM) and the multipole algorithm method; these are the subject of Section 3.3.2 and Section 3.3.3, respectively. We further propose a reciprocity based method in Section 3.3.4. Methods used to reduce truncation error when using NF data from only portions of the measurement sphere are reviewed in Sections 3.4.1 through 3.4.4.

3.3.1 – Conventional SWE Approach

The use of spherical wave modes in antenna engineering actually preceded the development of SNF antenna measurement techniques, as evidenced in [Pott 67] and [Pott 74].

[4] NSI2000 is the antenna measurement software produced by Nearfield Systems Inc. (NSI). As we will see through the rest of this work, this software is at the heart of the simulations and the implementations.

In essence, with reference to Figure 7, we measure $\vec{E}_{tan}$ on the spherical measurement surface S_{meas} surrounding the AUT and use a near-field to far-field (NF-FF) transformation to compute the FF radiation patterns. The NF-FF transformation for SNF measurements has principally been based on the spherical wave expansion (SWE) approach. The principal references are [Hans 88], [Yagh 86] and [Appe 86]. Expressions are given in these references for the SWE coefficients as integrals consisting of the scalar product of $\vec{E}_{tan}$ and the SWE functions. The integration is performed over the measurement sphere. These days the evaluation of such integrals numerically is not a difficult task and can be performed efficiently. The SWE approach is used in commercial SNF systems, which usually use the NIST software that implements the NF-FF transformation, although alternative commercial versions of such routines exist (eg. SNIFTD [Ticr]).

As stated above, we measure only $\vec{E}_{tan} = \hat{n}\ x\ \vec{E}_{meas}$ on the spherical measurement surface S_{meas}, where $\vec{E}_{meas}$ is the electric field at the measurement surface. However, the surface equivalence principle dictates that we need to know both $\vec{E}_{tan} = \hat{n}\ x\ \vec{E}_{meas}$ and $\vec{H}_{tan} = \hat{n}\ x\ \vec{H}_{meas}$ on S_{meas} in order to be able to determine the fields over any other surface (e.g. at observation points in the far field). This is because the surface equivalence principle requires that we know both $\vec{M}_s = -\hat{n}\ x\ \vec{E}_{meas}$ and $\vec{J}_s = \hat{n}\ x\ \vec{H}_{meas}$ on S_{meas}. In order to be able to use only $\vec{E}_{tan}$ to compute the FF patterns some rigorous electromagnetic theory based "trick" must be used. The SWE approach provides a very direct and convenient way to do this, since once the coefficient of the spherical wave modes are determined in terms of the electric field they can be used to compute the magnetic field. Refer to (a.10) and (a.11) to appreciate the coefficient swapping needed.

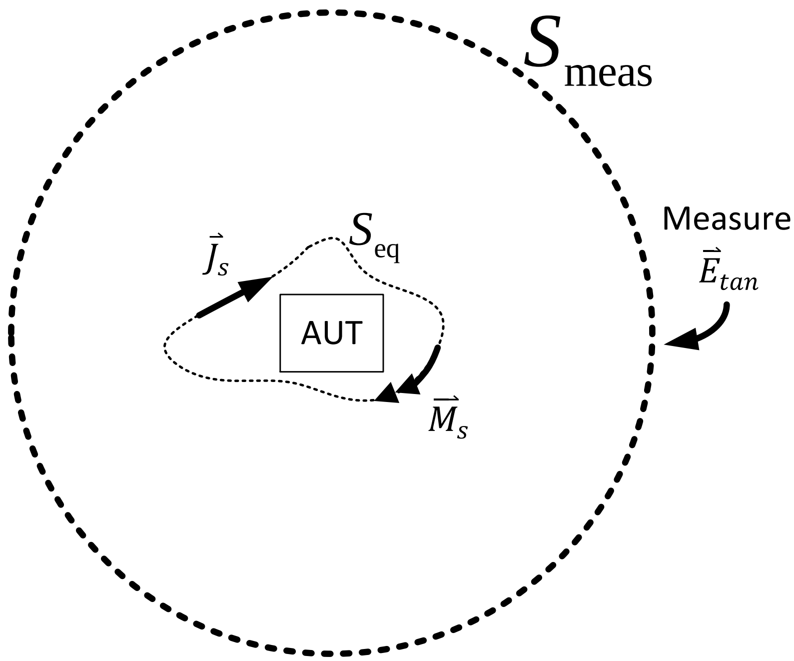

FIGURE 7 – SWE NF-FF TRANFORM FROM THE POINT OF VIEW OF SURFACE EQUIVALENCE PRINCIPLE

The present adaptive SNF work uses the conventional SWE approach to perform NF-FF transformation. This is the preferred way since it is computationally efficient, well-tested and part of the NSI2000 system already. However, should it in the future turn out that some chosen acquisition rule[5] results in non-smooth convergence of FF quantities as NF data is adaptively acquired we might need to use an alternative transformation method. Possibilities are discussed in the remainder of this chapter for completeness.

3.3.2 – Source Reconstruction Approach

The source reconstruction method (SRM) is an integral equation based approach that is easily understood with reference to Figure 7. The tangential electric field is measured at points on S_{meas} as usual. Thus we can write that we know $\hat{n}\ x\ \vec{E}_{meas}(\vec{\rho})$ at observation points $\vec{r} \in S_{meas}$. We know that this electric field is actually due to a physical electric current densities plus appropriate polarization current densities on the AUT structure. However, the surface equivalence principle allows us to replace these actual current density sources by equivalent electric and

[5] This is dealt with in Chapter 5.

magnetic surface current densities $\vec{J}_s$ and $\vec{M}_s$ respectively, on a fictitious surface S_{eq} that surrounds the AUT. The latter current densities exist at points $\vec{r} \in S_{eq}$. If we know $\vec{J}_s$ and $\vec{M}_s$ then we can use the free space Green's function to find the field $\vec{E}(\vec{r}, \vec{J}_s, \vec{M}_s)$ due to these current densities at any point $\vec{r}$ external to S_{eq}. If everything is to be self-consistent we must have

$$\hat{n}\, x\, \vec{E}\left(\vec{r}, \vec{J}_s, \vec{M}_s\right) = \hat{n}\, x\, \vec{E}_{meas}(\vec{r}) \quad \vec{r} \in S_{meas} \tag{3.11}$$

The expression for $\vec{E}(\vec{r}, \vec{J}_s, \vec{M}_s)$ will consist of integrals taken over S_{eq}. The SRM approach replaces the AUT by equivalent sources $\vec{J}_s$ and $\vec{M}_s$ by solving an integral equation for $\vec{J}_s$ and $\vec{M}_s$ using the method of moments. Once $\vec{J}_s$ and $\vec{M}_s$ are known the fields of the AUT can be predicted at observation points $\vec{r}$ both inside S_{meas} (but outside S_{eq}.) or outside S_{meas} (i.e. in the far zone) using the same superposition integral $\vec{E}(\vec{r}, \vec{J}_s, \vec{M}_s)$ used in the integral equation. If turns out that use of the SRM is not necessary in the adaptive SNF of this thesis and so is not used, as the processing time is much longer, as shown in Figure 8.

The SRM approach has been studied by many authors. We list here only those that have considered the use of the technique with SNF testing:

[Alva 06]	[Alva 07a]	[Alva 07b]	[Alva 08]	[Las 97]	[Las 99a]
[Las 99b]	[Las 06]	[Lope 08]	[Mart 11]	[Petre 91]	[Ponn 91a]
[Ponn 91b]	[Sark 99]	[Taag 96]			

One reason to use the SRM approach is more for antenna diagnostics than as a near-field to far-field transform. This is an important topic for practical antenna testing; many authors are still working on such topics. The surface S_{eq} can be chosen so that it coincides with the radiating aperture of the AUT. Then, the equivalent currents can provide information on the AUT operation or defect. Also, S_{eq} can be selected so that it coincides with the surface on which the AUT is mounted during testing. Therefore, the contributions of these equivalent currents can be omitted from the predicted FF, hence seeing the FF patterns without the test jig contribution.

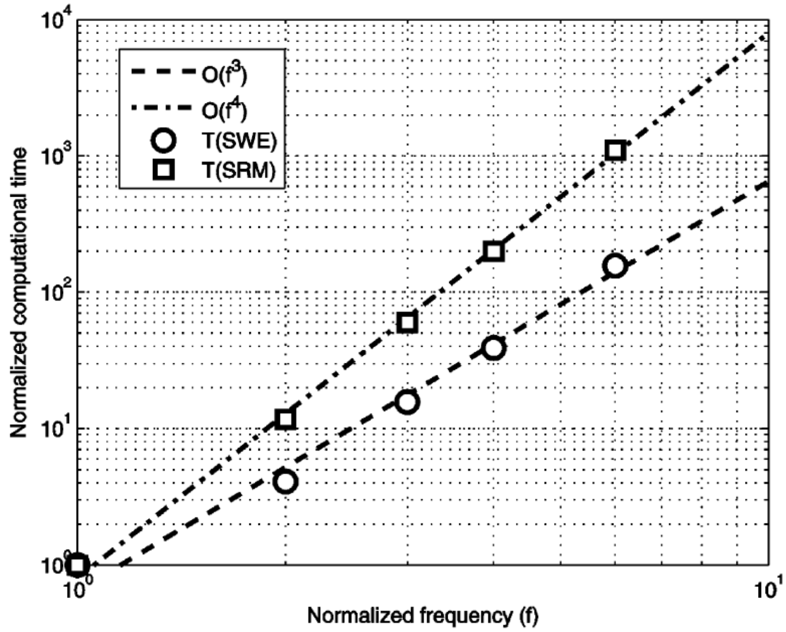

FIGURE 8 - COMPARISON OF TIMES FOR NF-FF TRANSFORMATION USING SWE AND SRM APPROACHES (AFTER [ALVA 08])

If one is using a pre-assigned partial SNF scan then it is of course of little consequence if the NF-FF transformation process takes longer than the SWE-based one. One can even argue that an AUT can be tested and then removed while its NF-data is being processed into FF-data, so freeing up the SNF range for the next AUT. In practice it is more likely that engineers would want to see what the performance is before dismounting the AUT; this is especially true when the SNF range is being used as a diagnostic tool or an antenna is being calibrated or fine-tuned in some way. At any rate, an excessive NF-FF processing time would not be acceptable if we wish to use an adaptive SNF approach. The amount of time taken by the SRM approach is compared to the SWE approach in Figure 8. As seen on the logarithmic chart, as problem size increases, the SRM approach will take much more time than the SWE method.

3.3.3 – Plane-Wave Spectrum Transformation

This technique was initially developed [Schm 08] to enable rapid implementation of higher-order probe correction in SNF testing (in fact for any surface which is a body of revolution). It does not use the SWE modes directly. Instead the SWE modes are expanded in propagating plane waves. More recent attempts at speeding up the transformation computationally have been described in

[Schm 10] and [Schm 11b]. Of more interest to the adaptive SNF work is the related publication [Schm 11a] by the same authors. The latter describes the use of the technique for cases where irregular sampling might be advantageous. This includes (a). combinations of canonical scanning surfaces such as cylindrical and spherical, and (b). irregular sample-point distributions with a higher sampling density in regions of fast field variations (eg. near NF data nulls), and lower sampling density in regions where the NF data is more gradually varying, in order to reduce the overall number of measurement points. This does not appear to offer any advantage as far as adaptive SNF algorithms are concerned, and so has not been studied in detail in this thesis because the traditional SWE based method is already fast enough.

3.3.4 – Reciprocity Based Method

If we were able to measure both $\vec{M}_s = -\hat{n}\, x\, \vec{E}_{meas}$ and $\vec{J}_s = \hat{n}\, x\, \vec{H}_{meas}$ on S_{meas}, we could use the conventional free space Green's function integrals to find the FF radiation patterns. But of course we do not measure $\vec{J}_s = \hat{n}\, x\, \vec{H}_{meas}$. One way of removing the latter from the picture is to argue that, since the surface equivalence principle (as applied here) produces zero fields inside S_{meas} we can introduce, as a theoretical artifice, a conducting sphere inside S_{meas} without changing the external fields predicted. This would mean that $\vec{J}_s = \hat{n}\, x\, \vec{H}_{meas}$ would not radiate, and so would not be needed. However, we would now need to determine the field $\vec{M}_s = -\hat{n}\, x\, \vec{E}_{meas}$ radiating in the presence of a perfectly conducting sphere of radius ρ_{meas}, as shown in Figure 9. A possible way to do this is proposed here for the first time.

The reciprocity theorem relates the electromagnetic fields and sources of one situation to the fields and sources of a second situation. We take the one source to be an infinitesimal magnetic dipole $\vec{M}_a = \hat{p}_{pol}\delta(\vec{\rho} - \vec{\rho}_\infty)$ at infinity, where $\hat{p}_{pol}$ is the polarisation of the FF pattern we eventually wish to compute from the NF data. This source thus produces a plane wave incident on the sphere. For a conducting sphere of radius *a* centred at the origin of the coordinate system, and a plane wave incident along the z-axis, the scattered magnetic field can be written as a spherical wave expansion with the coefficients [Blad 07]

$$a_n = -j2^{2n}\frac{(n-1)!\,(n+1)!}{(2n)!\,(2n+1)!}(ka)^{2n+1} \tag{3.12}$$

$$b_n = j2^{2n} \frac{(n!)^2}{(2n)!\,(2n+1)!} (ka)^{2n+1} \tag{3.13}$$

Thus we are able to calculate the electric field $\vec{H}_a(\vec{\rho})$ at points on the conducting sphere (that is, at $\vec{\rho} = \rho_{meas}$) due to the idealized source $\vec{M}_a$ at infinity. The second source is the "patch", or whatever sub-domain expansion function is selected in the expansion for the measured magnetic current density (that is, the measured tangential electric field), of magnetic current density $\vec{M}_b$ that resides on the surface of the conducting sphere, and whose far-zone field $\vec{H}_b(\vec{\rho})$ we wish to determine. In this scenario the reciprocity theorem reduces to the statement

$$\vec{H}_b(\bar{\rho}_{far-zone}).\hat{p}_{pol} = \iint\limits_{S_{meas}} \vec{H}_a(\rho_{meas}).\vec{M}_b(\rho_{meas})dS \tag{3.14}$$

In the far-zone the magnetic field is easily related to the electric field via the intrinsic impedance of free space. This will allow the NF-FF transformation to be performed if it is deemed necessary to use a sub-domain approach in adaptive SNF measurements.

Direct use of modern quadrature algorithms specifically devised for numerical integration over spherical surfaces might allow rapid multiple-evaluation of (3.14) and allow less restricted selection of sample points than SWE-based NF-FF transformation algorithms, which is bounded to a spherical grid. If one would be using Gauss quadrature, then the algorithm will require specific sample points, but this might not be convenient in practice.

As the work on adaptive SNF techniques progressed, it became clear that the reciprocity based method just suggested is not in fact needed, and so it has not been studied in more detail.

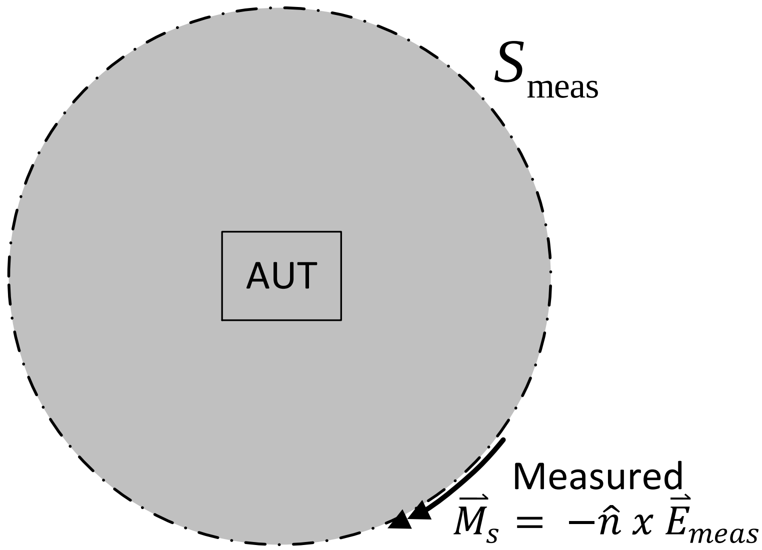

FIGURE 9 - MAGNETIC SURFACE CURRENT DENSITY AT SURFACE OF MEASUREMENT SPHERE

3.4 - Partial SNF Scan – Truncation of the Measurement Sphere

As can be seen from (3.3) and (3.4), if the minimum sphere is electrically large (i.e. the AUT antenna is electrically large), the steps in θ and ϕ become small, and a large number of points must be acquired. Of course, since an electrically large antenna will usually be directive, most of the energy is concentrated in a region of space. In such cases engineers have found it is worthwhile to consider truncating the scan area and restraining the probe to only sample a specified sector of the complete sphere. The fields outside the limited area are assumed to be zero. Such deliberate truncations have the potential to reduce the acquisition time.

The electromagnetic theory upon which the SNF technique is based requires the scan area to be a closed surface surrounding the AUT, in this case a spherical surface. Scanning only over a part of the spherical surface (so that we have partially-scanned SNF data) results in the so-called truncation error[6]. A number of authors have proposed methods for reducing the truncation error that results from using partial SNF measurement data. The underlying reasons given in such work to pursue the use of partial scans have been the following:

[6] Not only is the AUT radiation pattern not known outside the measured angular sector (a method of estimating the reliable angular region is given below), but there is also some truncation error within the "reliable" sector.

(a). Physical limitations on the AUT.

(b). Limitations of the SNF measurement system.

(c). Prohibitively long data acquisition time for full SNF scans.

It is reason (c) that is the driver for the present work, namely we are interested in the possibility of using partial SNF data in order to achieve the test time reductions associated with having to require fewer NF data points.

Conventionally, in partial scans the truncation of the measurement sphere is accomplished by selecting a spherical cap defined by an angle from the center of minimal sphere – the truncation angle. Such a cap must be selected to be in the same direction as the expected far-field pattern maximum so that the cap captures most of the power from the AUT. Thus the cap must be large enough and correctly located. The truncation angle limits the validity angle of the predicted far-field pattern to an opening angle narrower than the truncation angle – such angle is determined from a geometrical viewpoint to be

$$\theta_v = \theta_t - \theta_{tf} = \theta_t - \sin^{-1}(\rho_0/\rho_{sph}) \tag{3.15}$$

The meaning of the symbols in (3.15) is clear from Figure 10. Quantity ρ_{meas} is the measurement sphere radius and ρ_0 is the radius of the minimum sphere completely enclosing the AUT. Angle θ_v is the maximal validity angle and θ_t the truncation angle.

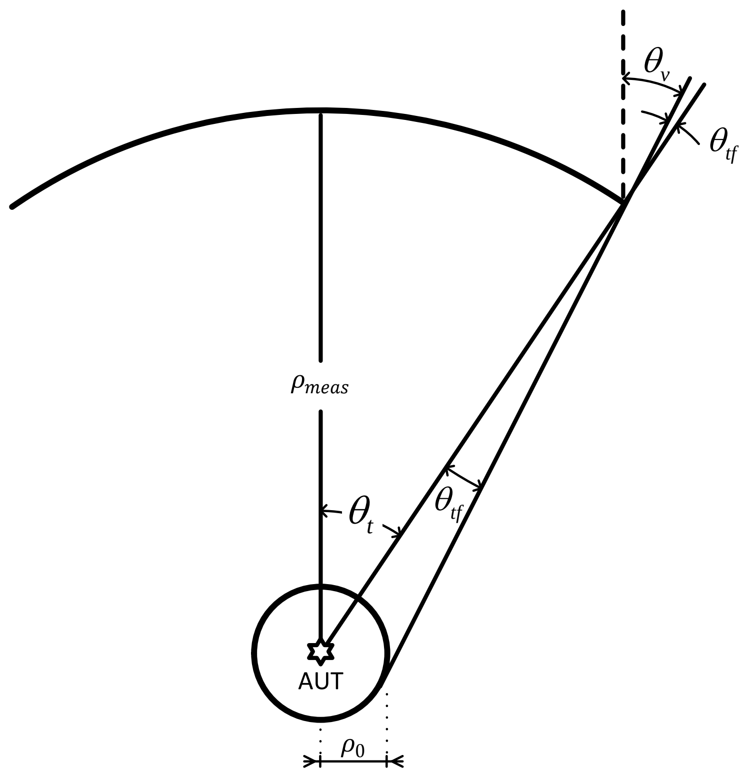

FIGURE 10 - TRUNCATION OF SPHERICAL NEAR-FIELD MEASUREMENT SPHERE

Several authors have been trying to seek ways to reduce truncation error effect, and/or increase the angle of validity compare to the angle of truncation. The next sub-sections are devoted to describing such techniques.

3.4.1 – Direct Matrix Approach

This approach [Yang 11] is actually intimately related to the conventional SWE method of Section 3.3.1, but is best classified separately, since it offers some flexibility that might have application in adaptive SNF approaches. The formulation is obtained by deriving a matrix form of the transformation that we can write symbolically as

$$[SWE\ Coefficients] = [Matrix\ of\ Mode\ Coupling\ Coefficients] x\ [NF\ Values\ of\ E - field]$$

Once we have the required number of SWE coefficients, determined as suggested in expression (3.1), we have the transformed FF data. This means that we need a sufficient number of NF data values in order that the above matrix equation has as many unknowns as equations. If we have acquired sampled NF values over only a portion of the measurement sphere then we could still solve the under-determined matrix equation in a least-squares (pseudo-inverse) sense. Alternatively, as done in [Witt 02], the partial recovery of the missing information can be obtained by estimating the spherical harmonic coefficients by a least-squares approach using data that is oversampled over the truncated scanning region (over-determined matrix equation). It is stated in [Yang 11] that the number of necessary sample points can be determined by examining the rank of the mode coupling coefficient matrix. This might be very useful in adaptive SNF work and could even form one of the decision functions whose concept is discussed in Section 4.5. However, further investigation would be needed since hard quantitative details are not provided in [Yang 11]. At any rate, the existing NF-to-FF transformation (based on spherical wave expansion theory) used in NSI2000 turns to be so fast that there was no reason to use the direct matrix approach in the work of this thesis.

3.4.3 – Non-Redundant Sampling Theory Approach

[Bucc 06] describes a technique to reduce truncation error (resulting from performing only a partial scan), which applies to any type of scanning surface, based on the concept of the information content of the field. This will not be discussed further here since we believe it is not applicable to the adaptive SNF work. The most important reason it is that it requires one to sample the NF data at points along selected axes perpendicular to the scanning surface. One could do this with SNF testing by performing a second partial scan over a measurement sphere of different radius. However, this will not decrease testing time. It would be useful in those cases where only a partial scan is possible for reasons other than test time reduction.

3.4.4 – Alternating Projections Approach

This technique had been applied to PNF testing, and only recently to the SNF case in [Mart 11] and [Cano 11]. The latter authors use slightly different implementations of what is generally known as the method of alternating projections [Star 98].

[Cano 11] uses a particular implementation of the method of alternating projections referred to as the Gerchberg-Papoulis algorithm. The SWE coefficients are found and FF data calculated on a (θ, ϕ) grid and then converted to a regular (k_x, k_y) grid[7]. We thus have the plane wave spectrum (PWS). The unreliable portion of the PWS is filtered out and is then back-projected (inverse Fourier transform) to the AUT aperture plane. All points on the aperture plane that lie outside the AUT aperture are set to zero, and the plane wave spectrum then found from this constrained aperture distribution as before. This plane wave spectrum will in turn have points outside the reliable region. These are retained. However, the new plane wave spectrum samples that lie in the original reliable region are replaced by their original starting values. These are then projected back to the aperture plane and the steps mentioned earlier repeated. And so on, iteratively, until some convergence criteria are met.

In [Mart 11] the projection algorithm consists of iteratively imposing matching of the computed NF with the actual measured NF samples and performing spectral filtering in the SWE mode domain, based on a knowledge of which SWE modes will be significant for the AUT of known physical extent.

Although the method of alternating projections is a powerful technique that has been used in many antenna applications, its application must be “supervised” (that is, users must be knowledgeable of the method) since it is susceptible to so-called traps and tunnels, and may not always converge [Star 98]. This would not be acceptable in an antenna measurement environment. Further testing of the method might reveal that convergence is almost always achieved for this specific application of the method, but with the limited cases checked in the mentioned publications one cannot be certain of this. It is too early to accept or discount the method as a useful technique for truncation error reduction in SNF testing using partial scans. None of these

[7] Although it also references other possible spherical wave expansion to plane wave expansion (SWE-to-PWE) conversions methods that can be used.

techniques have yet gained widespread acceptance as a mainstream solution in industry. Also, a fundamental resistance to "computing additional measured data", irrespective of its theoretical correctness, will likely continue to limit the application of any single method in the short term.

3.4.5 – Interpolation of Field Variation Approach

A technique using adaptively denser sampling regions when the fields have rapid spatial variations, and low density otherwise, was recently presented in [Qure 12]. In order to determine where the rapid variation occurs, for the SNF case, the authors proceed as follows:

- One or a few rings of NF samples are acquired
- A ring is skipped and the fields are measured and interpolated over the next ring
- The difference between the interpolated field and the measured field is then assessed
- A criterion is used to evaluate if the difference is high enough across the measured ring to require measurements on the skipped ring. This is evaluated at each point so that if only sparse points along the ring must be measured they can be sampled individually.

An example of an acquisition map[8] obtained using this technique is presented in [Qure 12], and is reproduced in Figure 11. While this technique is elegant for simulated data, and exhibits good results in theory, it is of absolutely no practical use the physical world. In fact it is believed that, using this technique, it would take much more time to measure an antenna than a conventional approach scanning the complete sphere. This becomes clear when we follow the movement of a probe if this approach were to be used. First, the probe must acquire at very least 50% of the complete NF array in a standard fashion, and then the probe must come back to points already acquired to sample sparse data in-between rings. The mechanical movement of the probe being the main culprit in acquisition time, the acquisition time needed to physically move the probe using this approach would outweigh, by far, the advantage realised by skipping some points.

[8] This terminology was introduced by the present author in [Beau 12], as part of the work on which this thesis is based, and will be described in Chapter 4 through 6.

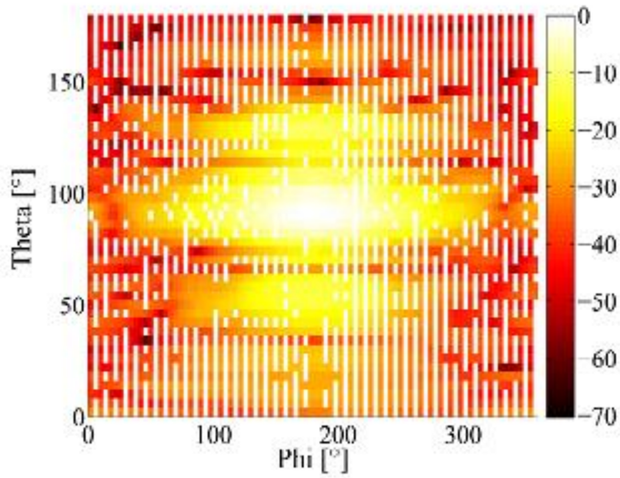

FIGURE 11 - NF ACQUISITION MAP FROM EXTRAPOLATION OF FIELD VARIATION (AFTER [QURE 12])

Also, apparently this method needs an irregular grid to work and uses the fast irregular antenna field transformation algorithm (FIAFTA) (the essentials of which are presented in [Schm 09]). In spite of this, given the few details given in [Qure 12], it seems that [Qure 12] applies a standard regular θ-ϕ NF grid anyway, thus removing the need for using the FIAFTA algorithm. This point could only be clarified if further details became available. This was not pursued since, due to its practical implementation limitations, this technique won't be used in this work.

Chapter 4 – The Adaptive SNF Concept

4.1 - Introduction

Section 4.2 presents the ideas behind the adaptive SNF technique that has been devised as part of this work. Three concepts are introduced to enable adaptive SNF algorithm development: the fact that NF-to-FF transformations can be performed while the acquisition is on-going, acquisition rules, and decision functions. Some guidelines are enunciated for all these in Sections 4.3 through 4.5, respectively. The implementation of these concepts will be discussed in Chapter 5, and the results of application of such adaptive SNF concepts will be shown in Chapter 6.

4.2 - Principles of the Adaptive SNF Approach

We assume that we have an existing conventional SNF facility and operation. The goal is to reduce near-field data acquisition time by requiring fewer data points than what is used on a conventional SNF approach.

We recognise that the NF-FF transformation computation time is small compared to the data acquisition time even if such computation is done repeatedly (while data is being acquired). This fact does not appear to have been previously explicitly recognised or exploited. The idea is that such computations be used as part of an adaptive algorithm intent on reducing the amount of data that has to be acquired, and hence the overall antenna testing time.

Full SNF scans are those described in Section 3.1. Partial SNF scans of the kind needed for adaptive SNF approaches will not cover the complete sphere, but can be the spherical caps described in Section 3.4 and other to be described in Section 5.3. Instead we will need to specify the locus of points that the probe must follow on the measurement sphere (until it is “told” to stop), so defining a particular partial scan whose shape will depend on the particular AUT. We will call the directed path to be followed by the probe the acquisition map that is controlled by the acquisition rule. Irrespective of the particulars of the acquisition map, we can think of any acquisition map in terms of a number of iterations, $n = 1, 2, \ldots, N$. We are of course at liberty to define the end of the n^{th} stage as we wish; indeed we could in the extreme define the acquisition of each new data point as the end of a new iteration (although we will not do this as the burden of computation can become large compared to the acquisition). At the end of each iteration we need to calculate the NF-FF transform, and compute a decision function value (discussed in Section 5.4) to decide whether to terminate the SNF data acquisition or not. If the decision is to continue with measuring NF data, the acquisition rule will use all the NF data acquired up to that iteration to determine the next portion of the probe's itinerary.

If we can define decision functions so that they provide a measure of the accuracy with which an identified performance index (e.g. directivity of the main beam; maximum side lobe level; root-mean-square side lobe level) is being determined at each iteration, then the SNF data acquisition can be terminated when the desired accuracy is reached. In this way we can acquire the smallest amount of data in order to achieve the desired accuracy of the selected performance measure of the AUT, thus minimizing the amount of testing time.

An acquisition rule (which uses NF data and results in an “acquisition map” of sample points) used in conjunction with a decision function constitutes an adaptive acquisition algorithm.

In principle all acquisition maps should be such that, if we use a decision function that always says "keep acquiring NF data", they terminate when the complete sphere has been covered – that is, in a full SNF scan. When they terminate they should not have acquired more data than that required by a full scan.

Probe correction need not be done during the adaptive procedure. Only once the final scan size has been reached, and data acquisition terminated, do we need to do probe correction to obtain the final radiation pattern.

For the acquisition rules to be developed, we must formulate some guidelines. This is discussed in Section 4.4. We also need to define possible decision functions to be used in the adaptive SNF techniques that will enable us to decide when to cease SNF data acquisition. Guidelines for decision functions are outlined in Section 4.5.

4.3 - Providing Measurement Feedback

In conventional SNF acquisition, which follows the flowchart shown in Figure 12, a large number of samples are acquired and processed only once to obtain the final FF characteristics. As previously mentioned, this method doesn't provide any feedback to the test engineer during the acquisition process. This can lead to the acquisition of an unnecessary number of NF data points that don't contribute significantly to the radiation pattern features of the antenna, computed through the NF-FF transformation, that are of interest for a particular AUT.

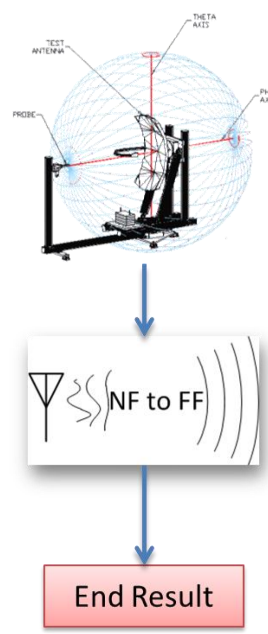

FIGURE 12 - CONVENTIONAL SNF MEASUREMENT PROCESS

The proposed adaptive concept, presented in Figure 13, allows use of a form of feedback loop as the acquisition is performed. A small number of samples are acquired; the samples to pick are dictated by the acquisition rule. This small dataset is then processed through a NF-FF transform. In the version of the adaptive SNF approach implemented in this work the NF-FF transform uses the thoroughly tested method found in the commercial software NSI2000. As already mentioned, this transformation is based on the SWE. The FF pattern obtained from the transformation of the small dataset is then evaluated by the decision functions. This operation looks at some desired characteristics of the antenna (directivity, side lobes, etc.) and decides whether the acquisition of NF samples should continue or halt. If the decision is to continue, then another small set of samples is acquired, processed through the NF-FF transformation and re-evaluated by the decision function. This is repeated until the decision function reaches its desired accuracy or the complete sphere of NF data is acquired. At this stage, the acquisition is stopped and some post-processing can occur if needed (graph plotting, derived parameters, automated report writing, etc.).

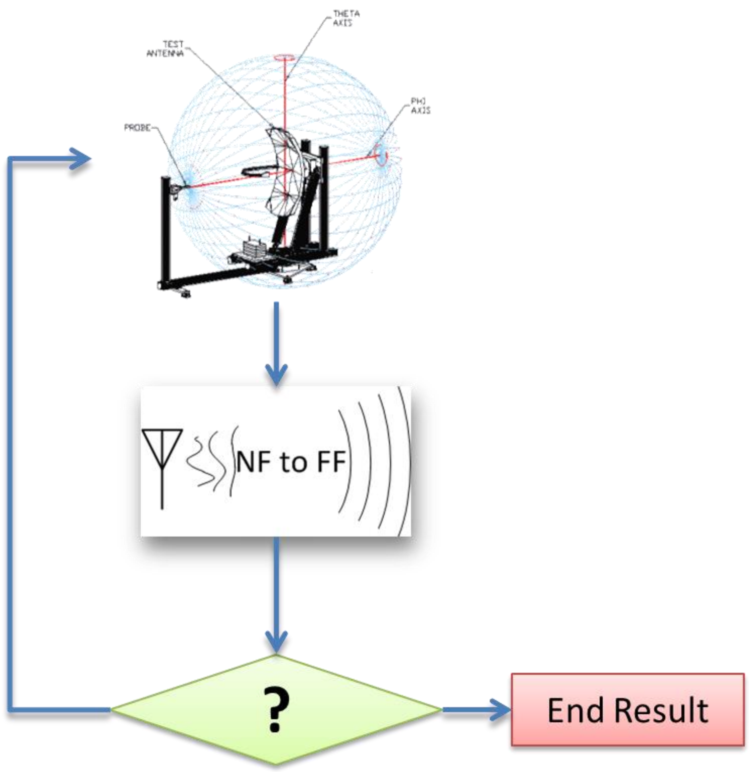

FIGURE 13 - PRESENTED SNF MEASUREMENT PROCESS

The value of showing, to the test engineer, the FF pattern evolution as the acquisition proceeds cannot be underestimated. A good example of where such feedback loop can be valuable is when the operator must verify if a directive AUT is properly aligned in the chamber. While not requiring excellent amplitude accuracy, this task only requires seeing if the main beam has an offset from the desired boresight direction. Instead of acquiring the full measurement sphere and losing precious time, only a small portion of that sphere might be necessary to detect the “beam squint”. Thus, the operator will appreciate the evolution of the FF as the acquisition is on-going, which can lead to error finding and diagnosis much sooner.

4.4 - Guidelines for Adaptive Acquisition Rules

By repeatedly computing the NF-FF transform from an increasing NF dataset we can observe the evolution of the FF pattern. Not only is this feedback useful for an operator, but it can also be used to modify the path of the probe for the next iteration. The objective of shaping the probe path is to get the fastest convergence of the FF parameters to a desired accuracy using the minimum number of acquired NF data samples.

The acquisition map is dictated by the acquisition rule, and the acquisition rule can be based on feedback received from the previous iteration. The principal goal for the acquisition rule is to acquire the samples that present the highest electrical field amplitude first, while maintaining mechanically efficient scanning[9]. The mechanical movement is of prime importance as it is considered the culprit as far as acquisition time is concerned.

We can imagine an acquisition rule (that we will eventually call rule #0) that gradually takes the highest amplitude samples in turn; this concept will be exploited to compare the developed acquisition rules but turns out (as shown in Chapter 6) to not necessarily be the most efficient one. It is understood that this acquisition rule would only be used in numerical simulation of the adaptive SNF method as *a priori* knowledge of the complete NF dataset is needed. It is not a realistic acquisition rule for practical use.

It is essential to make some assumptions in order to move forward with the development of realistic acquisition rules:

1. We assume a dual-polarized probe is being used. In those cases where test times are of the essence, engineers often use dual-polarized probes, which acquire the two orthogonal field components transverse to the sampling sphere simultaneously. Hence it is at once assumed that the two transverse field components $\vec{E}_\theta$ and $\vec{E}_\varphi$ are simultaneously acquired at each sample point on the sphere of radius.

2. We never want to move the positioner if we are not also acquiring samples at the same time.

[9] The mechanical efficiency refers to the ability to acquire samples only once, to sample the measurement sphere as the probe moves and to acquire the highest amplitude field points.

3. The specific adaptive algorithm chosen will in general depend on the type of AUT; yet ideally it would be completely antenna independent. We will classify four types of AUT :

   Class#1 - High gain antenna with main beam pointed at the North Pole.

   Class#2 - High gain antenna with main beam pointed slightly away from the North Pole

   Class#3 - Low gain antenna with a wide beam.

   Class#4 - High gain antenna with multiple beams (eg. monopulse antenna difference pattern)

4. We assume that we will always know, albeit only roughly so, the region of the NF measurement sphere where the NF data amplitude is largest. Thus the starting point on the measurement sphere for the acquisition map will be known.
5. Sampling redundancy, if any, should be minimal for any acquisition rule. Sampling the same point multiple times will increase the acquisition time for no reason.
6. The least favorable case for an acquisition rule is to sample the whole measurement sphere. If the acquisition rule is used in a sub-optimal scenario, it should acquire the complete measurement sphere; which is the current accepted standard for SNF measurements.

It was initially thought [Beau 12] that we shall always set the ϕ-value and acquire data by scanning over θ-values. Experience showed that the penalty of doing otherwise was actually small, and therefore this restriction was removed from the criteria the acquisition rules should satisfy. Also, even though classes of antennas are listed, it doesn`t mean that the acquisition rule must be antenna dependent; ideally the system should be antenna-independent and thus find its way no matter what AUT is present in the chamber. The formulation of these acquisition rules will be presented in Section 5.3.

4.5 - Guidelines for Decision Functions

There are two general requirements that a decision function must satisfy:

1. It must have a behaviour that allows us to boldly apply a stopping-criterion (that is, take an unambiguous decision as to the next step the SNF data acquisition must take).

2. It must be such that, when we apply a stopping-criterion, we end up with what we actually want. That is, a measurement proportional to the desired accuracy.

The most useful decision functions will be those directly related to antenna performance measures. These could be formed from the antenna specifications most important to a particular AUT. This will always be possible since, if it were not, then the performance specification measures could not be obtained from any antenna measurement technique! It will thus be feasible, no matter how specific an AUT performance specification for a particular application may be, to set up appropriate decision functions and use the adaptive SNF approach. The aim is that in this way, no matter how unique the application, we would be able to acquire the smallest amount of data in order to achieve the desired accuracy of the selected performance measure of the AUT. This will minimize the amount of testing time while simultaneously exhibiting real-time quality assessment of the measurements. The rapid NF-FF transformation capability should enable us to perform such computations repeatedly (and continuously monitor the decision functions whose values are computed continually) while data is still being acquired. We suggest examples of possible decision functions in Section 5.4.

4.6 - Concluding Remarks

In this chapter, the basis upon which to build the adaptive acquisition algorithm has been laid. Three founding concepts for adaptive work were introduced. The ability to observe the evolution of the FF as the acquisition is on-going is the crucial result for introducing feedback in the measurement process. This is possible with the processing power of modern computers; the time to process the NF-FF transformation is now small compared to the acquisition time. With the provided feedback, the shape of the locus the probe will follow (the acquisition rule) can be modified based on the measured near-field data at any stage. The acquisition should then halt once the selected accuracy of some key parameters, namely the decision functions, has been reached. These concepts are defined in detail in Chapter 5 and their performance studied in Chapter 6.

Chapter 5 – Implementation Plan for the Adaptive SNF Method

5.1 - Introduction

A necessary part in the development of the adaptive SNF algorithm is to build a flexible software interface that allows one to study and use various acquisition rules, decision functions and other techniques related to SNF adaptive acquisition through simulation. The interface must also be capable of being altered to perform actual physical acquisition once the outcome of the simulation study is complete. Such an interface is discussed in Section 5.2.

In Section 5.3, the acquisition rules developed are detailed and presented along with the reasoning behind them.

Section 5.4 presents the decision functions properly formulated. Some comments will be made as to why each decision function is of importance.

The inherent truncation that is introduced with use of an adaptive SNF algorithm creates a sharp discontinuity between known and unknown points in a NF array; recall that the unknown points are taken to be zero. To "soften" the discontinuity and provide a faster convergence, an interesting idea is to initially acquire NF data over two or three orthogonal cuts on the measurement sphere and interpolate the unknown NF datapoints from the cuts. That idea emerges from [Rens 11] and [Rens 12], which was implemented for PNF systems. Work done in this area for the more complex SNF application is presented in Section 5.5.

5.2 – General Software Implementation Details

The software framework developed for this work is mainly the combination of two software packages widely used in the antenna measurement community: NSI2000 and Matlab. The idea is to pass NF and FF data between both programs to get best of both worlds. It is easier to develop the acquisition rules and decision functions in, and to present non-standard graphical output using, Matlab rather than NSI2000 scripts. For instance, at each iteration of the adaptive SNF algorithm we will pass both the NF data and the transformed FF data from NSI2000 to Matlab. The selected decision function evaluation will take place in Matlab, which will then issue acquisition map instructions to NSI2000 based on the acquisition rule it has been instructed to apply. If a NF-to-FF transformation other than the SWE method is deemed necessary for some adaptive SNF algorithm, such a transformation can be implemented in Matlab. It was found that such transformation is not needed since the SWE approach is already fast enough.

Complete measured SNF data sets for individual AUTs will be used in the development and simulation of the complete adaptive SNF algorithm. In this work the performance of adaptive SNF algorithms will be examined using a software code to emulate a scanning sequence by simply extracting data points from the full SNF data set in the order in which it would be sequentially acquired in practice if the adaptive method were being used. Note that the NF datasets used here were acquired through measurement on actual antennas. We must emphasise this point since noise, mechanical defects, vibrations and other imperfections are present in these data sets. Thus, the presented algorithms are examined on "real-world" NF data and not simulated data.

An extension to this software framework enables a proper physical implementation, as opposed to simulated implementation. This is presented in Section 5.6.

5.2.1 - Framework Software

The general layout behind the framework code is presented in Appendix B, with the file tree presented in Appendix C. As seen, the majority of the algorithm is controlled by the scripting interface of NSI2000.

It starts with the setting of some simulation parameters, namely the type of AUT studied, the AUT test file to retrieve, which acquisition rule to use, and some flags setting the output type required. Then the appropriate directories are set so that the file system is created; refer to Appendix C for the file tree used. These settings have to be established by the user, but the rest of the script is automated. Once the initial parameters have been set, the appropriate file containing the complete measured data is loaded and processed for the first time; the NF and the FF data sets are generated within NSI2000. The script then initializes the appropriate files to receive results, and initializes the Matlab workspace file. The FF from the complete data set[10] is sent to Matlab as a reference and to find the position (and level) of the second highest peak that is the largest sideobe, the main lobe being the highest first peak. The method used to find the side lobe will be discussed in Section 5.4.4. At this point we must emphasise that the transfer from NSI2000 to Matlab is not trivial. A data array conversion is performed on the full NF and FF datasets to be sent to Matlab. NSI2000 uses a single precision number representation while Matlab works in double precision. The complete NF data array is saved in a temporary array so we can clear the NF arrays that NSI2000 is using to process the fields. By putting to zero the NF data array, we clear the values to simulate a new acquisition. Every time the algorithm acquires a point, the value from the temporary array, composed of the complete original NF, is copied to the same position in the current NF array. At this point, with the clean NF array, the algorithm can perform the NF pre-conditioning[11] to smooth the discontinuities.

Once the initialization is completed, the algorithm can perform acquisition and study the decision functions. Initially the acquisition rules were made the responsibility of Matlab. In the current more evolved version, the acquisition is now under the control of NSI2000. The reasoning behind this decision is that the repetitive transfer of NF matrices, involving array conversion, processing via Matlab, and a second array conversion put an un-necessary computing load on the algorithm. By taking the acquisition to NSI2000, the simulation time is greatly shortened. To perform the acquisition and the study of decision functions, multiple acquisition rules were devised to account for various acquisition patterns of the original data (ϕ-180, ϕ-360); these will be explained in Section 5.3. Irrespective of the acquisition rule selected, the acquisition algorithm performs a loop, and runs through the following steps at each iteration :

- Acquire a small number of samples in accordance with the acquisition rule
- Compute the FF from these NF samples
- Send the FF array to Matlab
- Send parameters (directivity, % data set, % complete sphere, amplitude peak value and iteration number) to Matlab
- Matlab determines the location and level of the highest side lobe

[10] Recall that in the simulation studies performed in this work we start with a complete NF data set and then simulate actual acquisition by picking up these points in a way that emulates actual acquisition.
[11] Pre-conditioning is discussed in Section 5.5.

- Process the modal content to display graphically the coefficients, refer to Section 5.2.2.
- Display the iteration evolution and the decision functions

5.2.2 – Mode Processing

Since NSI2000 uses SWE techniques to perform the NF-FF transformation, it is possible to visualize and extract the coefficients used. A function that extracts SWE coefficients and formats them for Matlab was written. In NSI2000 the SWE coefficients are file-based, thus the file must be parsed properly [Betj 12]. Then the coefficients must be correctly assigned to an array that can be sent to Matlab. Note that in the current implementation of the Matlab script, only the coefficient amplitudes are sent; the phase can be sent as well if deemed necessary with minor modifications.

Also, with the current version of NSI2000, the modal coefficients can be extracted but not modified and re-inserted. Hence, we can observe the coefficients but not adjust them for re-processing. The decision was therefore taken to leave mode filtering for future work should it turn out to be of interest for adaptive SNF algorithms.

5.2.3 – Timing Tests on processing operations

Time reduction being the end goal of adaptive SNF methods, it is of interest to quantify the time needed to perform various portions of the adaptive acquisition. It is relevant to grasp the trend of some crucial software functions used by the adaptive algorithm; some test routines were written in order to do so. The results are summarized in Appendix D. These tests were performed with a 2005 processor AMD X2 4600+ with 2 GB of RAM and a Windows 7 32-bits operating system. Brief definitions of the tests performed are as follows:

<u>Test 1 - NSI NF processing</u> : Open AUT file and process NF data

<u>Test 2 – NSI FF processing</u> : Open AUT file and process FF data

<u>Test 3 – Send NF to Matlab</u> : Send NF array to Matlab

Test 4 – Get NF from Matlab : Retrieve NF array from Matlab and assign it to current NF array

Test 5 – Send FF CoPol Amp to Matlab : Send FF copolarized amplitude array to Matlab

Test 6 – Send FF Dir to Matlab + Compute Diff + Get Results : Send directivity value to Matlab, perform a simple arithmetic subtraction operation in Matlab initiated from NSI2000, and retrieve the result

Test 7 – Run SidelobeFinder in Matlab on FF sent + Retrieve max val : Using previously sent FF data, use the function SidelobeFinder (refer to Section 5.4.4) to locate the side lobe, and send the position and amplitude to NSI2000

Test 8 – Compute Error Function in Matlab on FF sent + Retrieve max val : Compute error function in Matlab and retrieve result with NSI2000

As seen from Appendix D, Tests 1-6-7-8, are relatively independent of the data set size and are fast to perform. While Tests 3 and 4 are linear with respect to the number of NF samples, and Test 2 seems to exhibit a logarithmic trend, as seen in Figure 14. Five AUTs were tested to obtain the results shown. Even though it is independent of the data set size, one can also note the time taken to send the FF array to Matlab (Test 5) is around 5 seconds here. The reason why it takes so long is that each point in the FF array has to be interpolated first; this slows down the operation. However, it is clear that the times are relatively small, and the assumption that the overall test time will be determined principally by actual acquisition time is a valid one.

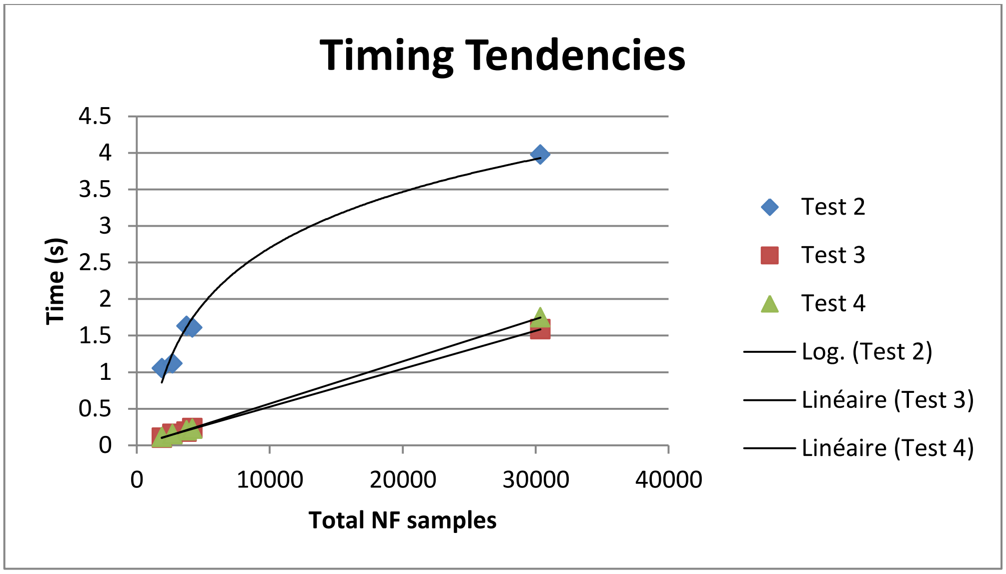

FIGURE 14 - TIMING TENDENCIES OF EACH PROCESSING TEST PERFORMED

5.3 – Acquisition Rules

Here we define the acquisition rules developed. In the early stages of this work many such rules were considered. Now, with appropriate criteria defined, some previously defined rules were found to be inapplicable, mostly due to mechanical constraints and inefficient acquisition, and are not included here. Also note that for each acquisition rule devised, a ϕ-180 and a ϕ-360 version has been written in order to accommodate various antenna acquisition schemes.

5.3.1 – Acquisition Rule #0 – Highest Samples First

The choice to number this acquisition rule with 0 is deliberate as it is not a practical acquisition rule but one that we hoped would serve as a basis against which to compare other acquisition rules. This rule can only be used in simulation, since it requires *a priori* information about the fields on the complete measurement sphere. At each iteration, a threshold is set and any NF points with an amplitude value higher than this threshold is acquired. This threshold is lowered at each subsequent iteration, e.g. at iteration *n* the threshold is at -10dB, and then at iteration (n+1) the threshold is -15dB. This is done until the complete NF array is acquired. Therefore, only the highest value points are acquired first. It was believed that in these circumstances, any other acquisition cannot converge faster that this one. This turns out not to be the case, comments being to this effect made in Section 6.3.1.

5.3.2 – Acquisition Rule #1 – Increasing Cap

Acquisition rule #1 results in an acquisition map (illustrated in Figure 15) that is similar as that of the conventional partial scan method described in Section 3.4. In other words, the rule results in a growing cap of sample points, with scanning in ϕ. The truncation angle θ_t is increased after each iteration by an amount Δθ. Note the first iteration has θ = 0° and the probe completes a 360° rotation about the z-axis. The second iteration has θ = Δθ° and the probe again completes a 360° rotation in ϕ. The n-th iteration encompasses the sampling points of all previous iterations. While not using information from previous iterations to shape itself, this acquisition rule will be shown to be of importance; it is a very simple acquisition rule that satisfies all the criteria mentioned in our guidelines.

Note that in Figure 15, the dots are possible sample points and the coloured lines represent the probe movement, and thus the acquired samples. The different colours represent different iterations.

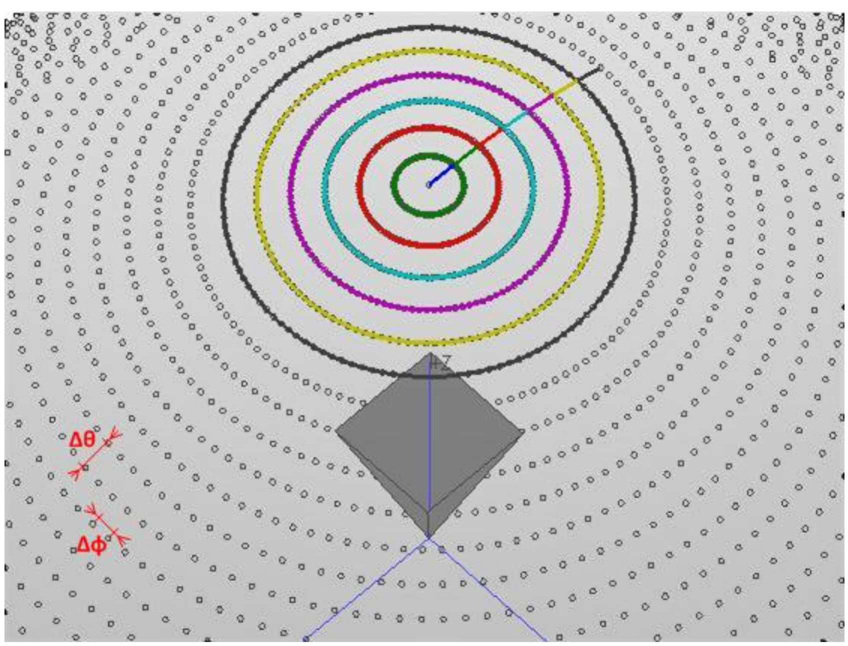

FIGURE 15 - ACQUISITION RULE #1: INCREASING CAP

5.3.3 – Acquisition Rule #2 – Guided Threshold

The second acquisition rule is a two-fold process. The first iteration of this rule proceeds as follows: The probe starts at θ = ϕ = 0°, and then scans in θ until a sampling point is reached where the total measured electrical field amplitude

$$\left|\vec{E}_{NF}\right| = \sqrt{\left|E_{NF_\theta}\right|^2 + \left|E_{NF_\varphi}\right|^2} \qquad (5.1)$$

is less than a pre-defined threshold value. The probe then increments its position by Δϕ and scans back to the centre of the measurement sphere in θ to increment again its position by Δϕ. These steps are repeated until ϕ has gone from 0 to 360°. The second and subsequent iterations of this rule then proceed as follows: Each iteration adds NF data acquired at all sample points lying within a user-defined band of width mΔθ circumscribing the acquisition map created during the previous iteration. Integer m sets the width of this band that will follow the acquisition map created during the previous iteration. This process will favour particular regions of higher electric field magnitude and therefore allow for a level of adaptation as the process evolves. The described process is illustrated in Figure 16. Note that no sample point is missed between iterations.

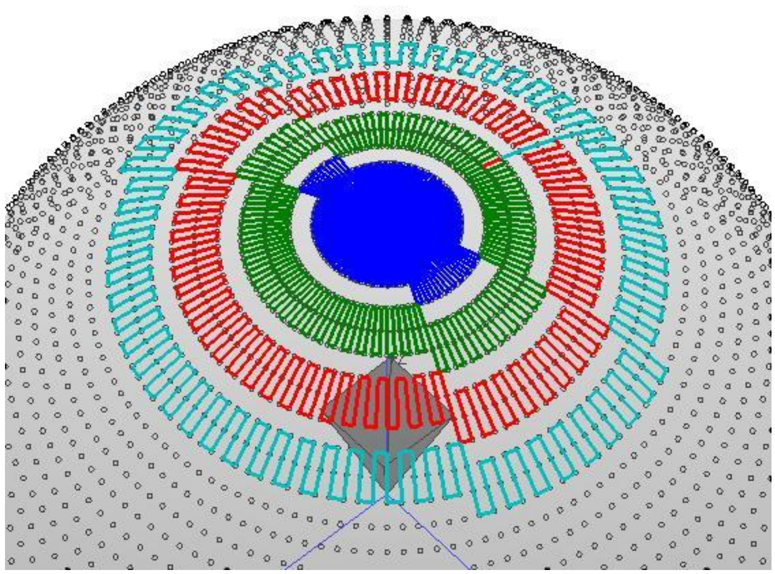

FIGURE 16 – ACQUISITION RULE #2: GUIDED THRESHOLD

5.4 – Decision Functions

5.4.1 – Absolute Directivity Values

The co-polarized (partial) directivity in direction (θ, φ) can be computed using

$$D_{co}(\theta, \varphi) = \frac{4\pi |E_{co}(\theta, \varphi)|^2}{2\eta_0 P_{rad}} \tag{5.2}$$

where η_0 is the free space intrinsic impedance. The total radiated power P_{rad} can be found using the SWE coefficients obtained from the NF data available at the nth iteration. An expression similar to (5.2) can of course be used for the cross-polarized case. We can observe the directivity in the direction of maximum radiation as the scan size increases. In the case of the co-polarized directivity this occurs in some expected direction, but in the cross-polarized case the direction in which the directivity is a maximum might not be known. The locations of such maxima are easily determined through simple automated searching of the numerical data at each iteration.

Both the co- and cross-polarized maximum directivity plots should converge to some steady value as the scan size increases. At some point the directivity value should change negligibly from the (n-1)th to the nth iteration. If this change is less than a certain amount, say the known accuracy within which the directivity can be determined by the measurement set-up, this can be used to terminate the SNF scan. We expect the co-polarized maximum directivity to settle down at a smaller scan size than the cross-polarized one. This is to be expected as the cross-polarized patterns are at much lower levels than the co-polarized ones, and are therefore more sensitive to measurement errors (including truncation error). If the polarisation properties are the important ones in some test then both the co- and cross-polarized directivities could be tracked. Instead of (or in addition to) the directivity maximum we could also observe the directivity in the direction of the highest side lobes. The directions of such side lobes are easily found using technique proposed in Section 5.4.4.

5.4.2 – Directivity Changes Between Scan Iterations

Alternatively, we can directly track the changes in the directivity

$$\Delta D_{co}^{n}(\theta_i,\varphi_j) = \left|10\log D_{co}^{n}(\theta_i,\varphi_j) - 10\log D_{co}^{n-1}(\theta_i,\varphi_j)\right| \tag{5.3}$$

in a specific direction (θ_0,φ_0), say, from one iteration to the next. The directivity differences would be computed here by subtracting the dBi values of the directivity. The reason is that we want the value ΔD_{co}^{n} to decrease to zero as the scan size increases. These should all taper off as the scan size enlarges with increasing scan iteration count. The scanning can be terminated once $\Delta D_{co}^{n}(\theta_0,\varphi_0)$ falls below 0.1dB, for instance. It would also be possible to observe these differences in the directions of side lobes that might determine whether the AUT satisfies its pattern specifications. We could for instance examine $\max_{i,j}\{\Delta D_{co}^{n}(\theta_i,\varphi_j)\}$, which could be the maximum difference in directivity over all directions within some specified angular range of the main beam direction. We are not interested in directivity differences in the directions of pattern dips, since these can be large and meaningless. Thus only those points (θ_i,φ_j) for which $D_{co}^{n}(\theta_i,\varphi_j) > -30dBi$ (for example) could be considered in determining $\max_{i,j}\{\Delta D_{co}^{n}(\theta_i,\varphi_j)\}$.

5.4.3 - Normalized Pattern Differences Between Scan Iterations

After the n^{th} and $(n-1)^{th}$ scan iterations we denote the far-zone co-polarized electric field value in direction (θ_i,φ_j) by $E_{co}^{n}(\theta_i,\varphi_j)$ and $E_{co}^{n-1}(\theta_i,\varphi_j)$, respectively. These are obtained at each iteration using some NF-FF transformation. The error term in direction (θ_i,φ_j) is, after the n^{th} iteration, then

$$f_{co}^{n}(\theta_i,\varphi_j) = \frac{\left|E_{co}^{n}(\theta_i,\varphi_j)\right| - \left|E_{co}^{n-1}(\theta_i,\varphi_j)\right|}{\max\limits_{i,j}\left|E_{co}^{n}(\theta_i,\varphi_j)\right|} \tag{5.4}$$

In other words, the error measure in every direction is the normalized difference between the n^{th} and $(n-1)^{th}$ patterns in that direction. Therefore, the full three-dimensional pattern is considered rather than just single pattern cuts. The normalization factor is simply the maximum field magnitude after the n^{th} iteration. Observe that the error term is direction dependent, that the values of the quantities in (5.4) are not in decibels, and that a similar quantity can be defined for the cross-polarized fields. If the normalized radiation pattern magnitude in direction (θ_i, φ_j) is E_{dB}, and we wish the uncertainty there to be $\pm\Delta_{dB}$, then we require

$$20\log\left|f_{co}^{n}\left(\theta_i, \varphi_j\right)\right| \leq E_{dB} + 20\log\left\{1 - 10^{-\Delta_{dB}/20}\right\} \tag{5.5}$$

As a decision function we could also observe the value of f_{co}^{n} in some specific direction (θ_0, φ_0) or set of directions such as the pattern maximum and important side lobes, or its maximum value in all planes out to some maximum angle, and continue scan iterations until these are sufficiently small.

5.4.4 – Side Lobe Directivity

Side lobe level is often a performance requirement for an AUT, and so needs to be associated with some decision function. Side lobes could “move around” slightly as an increasing number of NF data points are acquired during the running of the adaptive SNF process. So after each iteration we need to first locate the side lobe and then identify its level. We have used an algorithm from the field of computer vision for this purpose. It is designed to be able to quickly locate maxima out of a set of data values.

The technique is used to track several pattern peaks. The highest is assumed to be the main lobe, as will be the case with all correctly operating antennas. So with the FF represented as an array of data points, the task to track the first side lobe is to find where the second highest local maximum is within that grid of points, the first one being the main beam. The side lobe tracking must occur rapidly enough to be processed at every iteration without impacting significantly the processing time. Few algorithms are available, but we have borrowed the above-mentioned one from the computer vision discipline. Since digital images are simply an array of color levels, the FF data array can be viewed as an image as well, and any computer vision algorithm can be applied on it. Matlab implements the IMDILATE function [Matw 13a] to dilate an image. This function can be used to find local maxima by specifying a filter

$$\begin{bmatrix} 1 & 1 & 1 \\ 1 & 0 & 1 \\ 1 & 1 & 1 \end{bmatrix} \tag{1.1}$$

This filter is a so called binary morphological structuring element, where the array contains only 1's and 0's. As described in [Matw 13b], "the location of the 1's defines the neighborhood for the morphological operation". In this case the grayscale morphological operation is a binary dilatation defined as

$$(A \oplus B)(x,y) = \max\{A(x-x',y-y') + B(x',y') | (x',y') \in D_B\} \tag{5.6}$$

where,

D_B is the domain of the morphological structuring element B

A(x, y) is assumed to be -∞ outside the image domain

Commonly, with a flat structuring element (B(x, y) = 0), the operation becomes

$$(A \oplus B)(x,y) = \max\{A(x-x',y-y') | (x',y') \in D_B\} \tag{5.7}$$

More details about computer vision algorithm and image dilatation can be found in [Gonz 09]. However, it is not necessary to understand all the details to apply this Matlab function successfully; a "user's approach" has been adopted here.

The above procedure enables Matlab to list very quickly (sub-millisecond) local maxima for a moderate size FF array (401 x 401, thus 160k points). The position as well with the amplitude of the desired side lobe is then retrieved for further processing.

5.4.5 - Averaged Error Measures

We could also average the quantities $f_{co}^{n}\left(\theta_i, \varphi_j\right)$ or $D_{co}^{n}\left(\theta_i, \varphi_j\right)$ over all directions within the region of interest. These would provide curves that smoothly taper off as the scan size increases. The problem is that it might be difficult to decide on a threshold value to be used for terminating the scan iterations. The reason is that the averaged quantities are not directly related to a measure in terms of which antenna performance specifications are written or through which the accuracy of these quantities can be expressed. Also, in general, since averaging is the equivalent of a low-pass filter, the decision function might halt the acquisition later than necessary, thus acquiring slightly more samples than required.

5.5 – Near-field Matrix Pre-Conditioning

5.5.1 – Spherical Interpolation Concepts

At the beginning of this work the start values of all NF data points were assumed to be zero, implying that fields on the measurement sphere were zero everywhere. These values were then replaced by actual measured data as the acquisition proceeded. At any stage only a portion of the fields on the measurement sphere would have been sampled. This introduced a significant and ever changing truncation effect. In order to “soften” this transition an interpolation method that was implemented for adaptive planar near-field (PNF) systems in [Rens 2012], was devised here for SNF application, and referred to as pre-conditioning. The idea is to use an approximation of the NF data as a starting point instead of an empty NF array, thus avoiding the use of zero field values entirely. Two or more cuts of NF data are acquired before the adaptive SNF method is initiated, and the entries in the NF array are set to the values obtained by interpolation of the data points acquired.

Three possible orthogonal cuts on the sphere are considered; the first two cuts are referred to as longitudinal cuts while the third is referred to as an equatorial cut:

- Cut $\phi = 0°$, with θ from 0° to 360°
- Cut $\phi = 90°$, with θ from 0° to 360°
- Cut $\theta = 90°$, with ϕ from 0° to 360°

While the implementation of this concept is relatively simple for the PNF case, the SNF counterpart is geometrically more complex. The added complexity lies in the fact that the direction of the unit vectors at each point on a sphere are dependent on the position on the sphere itself. The problem to solve can be stated as follow: Provided with orthogonal cuts of the NF measured tangential E-field on a measurement sphere, estimate the tangential field at any other points on that same sphere.

Not all three orthogonal cuts are required to interpolate a point. A balance has to be established between the time needed to acquire the cuts and the precision of the interpolation; the accuracy is expected to increase with more cuts. At a minimum two cuts are required to interpolate a point; if more are available then some form of averaging must be performed to accommodate the results obtained from every possible combination of interpolation pairs. The function that interpolates the fields at a point using measured points is called the interpolation function. That function must ensure that, as the interpolated point tends towards a measured point, the interpolated value converges to the known value. The three interpolation functions studied in this work are described in the Sections 5.5.2, 5.5.3 and 5.5.4 respectively. The first two methods use linear interpolation, while the third method uses the spherical wave expansion itself to provide pre-conditioning. The mathematical expressions underlying of the first two linear interpolation methods is provided in Appendix E.

In this work, and for the three methods, only two cuts are used: the longitudinal cuts at $\phi = 0°$ and at $\phi = 90°$. By selecting this minimum numbers of cuts, an interpolation is possible with minimal amount of acquisition time, as the acquisition of a cut is of course taking some time. The longitudinal cuts are preferred here for the sole reason that they are more natural to deal with data array operations; they are both at fixed ϕ, which is two rows in the θ-ϕ array.

The resulting effect of the NF pre-conditioning on the performances of the adaptive algorithm is described in Chapter 6.

5.5.2 – Method #1 : Component Interpolation

The first interpolation function is a linear interpolation of each component $\left(E_\theta^{interp}, E_\varphi^{interp}\right)$ directly from the components of the known points, $(E_\theta^1, E_\varphi^1)$ and $(E_\theta^2, E_\varphi^2)$ respectively . That is, the component E_θ^{interp} is linearly interpolated from E_θ^1 and E_θ^2, and similarly, E_φ^{interp} is interpolated from E_φ^1 and E_φ^2. Note that the two known points and the interpolated point are all along the same latitude on the measurement sphere. The linear interpolation is a function, in this case, of the position in ϕ between the two measured points.

5.5.3 – Method #2 : Projection Interpolation

The second interpolation function starts by transforming each spherical component of both known points, $(E_\theta^1, E_\varphi^1)$ and $(E_\theta^2, E_\varphi^2)$ respectively, to Cartesian components. Then, the Cartesian components of the interpolated point $(E_x^{interp}, E_y^{interp}, E_z^{interp})$ are linearly interpolated from the respective Cartesian component of the known point. Thus, E_x^{interp} is a linear interpolation based on E_x^1 and E_x^2; a similar operation is applied for E_y^{interp} and E_z^{interp}. When the Cartesian interpolation of the interpolated point are known $(E_x^{interp}, E_y^{interp}, E_z^{interp})$, a projection onto spherical components is performed to retrieve ($E_\rho^{interp}, E_\theta^{interp}, E_\varphi^{interp}$). Note that the projection must take in account which point is being interpolated since, as mentioned, the unit vectors change direction as we move on the sphere. Also, generally a small radial component E_ρ^{interp} will result when using this technique. In this case we simply set it to zero. It is believed that this fact will introduce an inherent systematic error, which will be the largest along the equator at equal distances from the known points.

5.5.4 – Method #3 : Spherical Wave Expansion Interpolation

This third method is different from the previous two; instead of using linear interpolation it uses using spherical wave expansion properties. As previously mentioned, the longitudinal cuts are acquired on a NF grid set to zero; the size of the grid being set by the maximal radial extent (MRE) of the AUT. From SWE theory, the sharp spatial discontinuities from the finite field to the null points needs a very large numbers of modes to represents this state. This is analogous to the spectral representation of a square-wave in time. By using only a relatively small number of low order modes, we eliminate the non-physical propagating fields from the solution, thus smoothing the NF array. The numbers of modes to use is dictated by the maximum radial extent (MRE) of the AUT. A relation exists between the physical size of the antenna and the numbers of modes that will propagate. This method is the equivalent of applying a low-pass filter on the spectral expansion of spherical waves.

5.6 – Concluding Remarks

The chapter began by defining the software framework needed to study, in simulation, the adaptive acquisition algorithm. That code enables us to perform simulations on each concept of adaptive acquisition algorithm independently. Some timing tests were performed against this framework to validate its use for adaptive acquisition work. It appears to be efficient enough to continue conducting work with it. Three acquisition rules were then defined: Highest samples first, increasing cap and guided threshold. Four decision functions were defined. Based on the absolute directivity, the delta directivity, the pattern error and/or the side lobe directivity, we will halt the acquisition. These acquisition rules and decision functions will be studied using the software framework in the next chapter.

Chapter 6 – Simulation Results and Physical Implementation

With the suggested technique and the tools devised, the adaptive algorithm is here applied to some NF datasets. These datasets were obtained from actual antenna measurements. As mentioned in Section 5.2, in this study we use datasets acquired over complete measurement spheres, and then emulate the acquisition of adaptive acquisition maps in software by selecting the datapoints picked by the acquisition rule. In practice the complete sphere datasets would not actually be acquired, and only those points identified by the acquisition map as the algorithm progresses would be sampled.

Section 6.1 gives a brief overview of the antennas used for assessment of the adaptive algorithm. The FF and the NF data arrays are also presented. In Section 6.2 the NF pre-conditioning is studied and the reason for using this technique is explained. The acquisition rules are compared for the various AUTs in Section 6.3. Section 6.4 deals with the comparison of the four decision functions. Finally, Section 6.5 summarises the conclusions of the above study and describes the physical implementation of the adaptive SNF technique that followed.

6.1 – AUT Presentation

In this chapter, when we will refer to a particular antenna, the antenna's acronym designation will be used (i.e. FAN, ISO, BSA or SGH).

Antenna Designation	**Type**	**Frequency of Operation**	**AUT Size**	**Directivity**	**Sidelobe Level Relative to Main Lobe**
FAN	Fan Beam	3.3 GHz	2.4 λ x 6.2 λ	17.34 dBi	-6.32 dB
ISO	Isoflux	14.15 GHz	6.1 λ x 6.1 λ	6.98 dBi	-0.02 dB (Not a Sidelobe proper)
BSA	Base Station	1.705 GHz	2.3 λ x 8.1 λ	20.65 dBi	-15.54 dB
SGH	Standard Gain Horn	8.2 GHz	3.9 λ x 5.3 λ	21.55 dBi	-9.88 dB

TABLE 1 - AUT CONSIDERED IN THIS WORK

The next subsections briefly present the AUT NF and FF patterns on a spherical grid (either θ-ϕ or azimuth-elevation), as well as some comments on the reasons for the selection of these particular antennas.

6.1.1 – Fan Beam Antenna

The fan beam antenna NF data was acquired with the antenna field maximum pointing towards the North Pole of the measurement sphere. This antenna is a Class #1 type antenna according to the classification used in Section 4.4. Its NF data is shown in Figure 17 as a function of (θ, φ) over the complete sphere. By 'normalised energy' we actually simply mean the amplitude of the tangential electric field. After NF-to-FF transformation using NSI2000 we obtain the results shown in Figure 18. The wider beamwidth (of the 'fan') occurs in the azimuth plane.

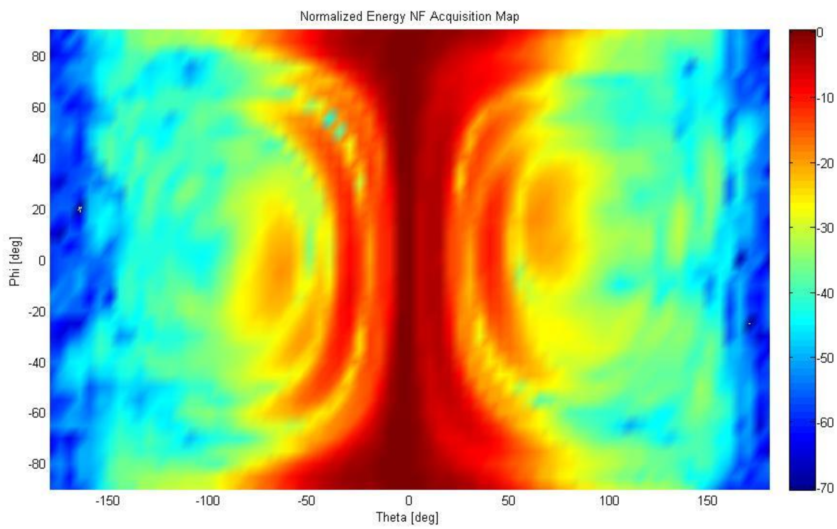

FIGURE 17 - FAN BEAM ANTENNA NF PATTERN

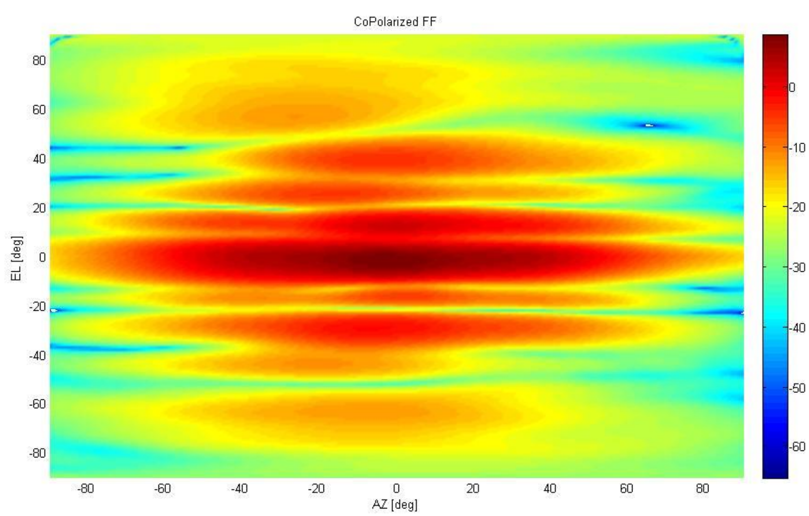

FIGURE 18 – FAN BEAM ANTENNA FF PATTERN

6.1.2 – Isoflux Antenna

The isoflux antenna NF data was acquired with the antenna mechanical boresight pointing towards the North Pole of the measurement sphere, but its main lobe maximum lies on a ring surrounding this direction. This antenna is a Class#3 type antenna according to the classification used in Section 4.4. Its NF data is shown in Figure 19 as a function of (θ, φ) over the complete sphere. After NF-to-FF transformation using NSI2000 we obtain the results shown in Figure 20.

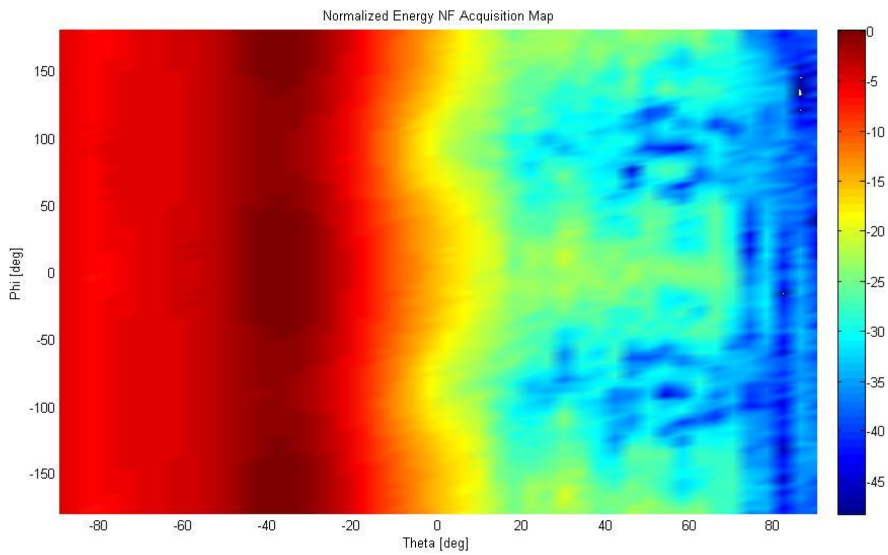

FIGURE 19 - ISOFLUX ANTENNA NF PATTERN

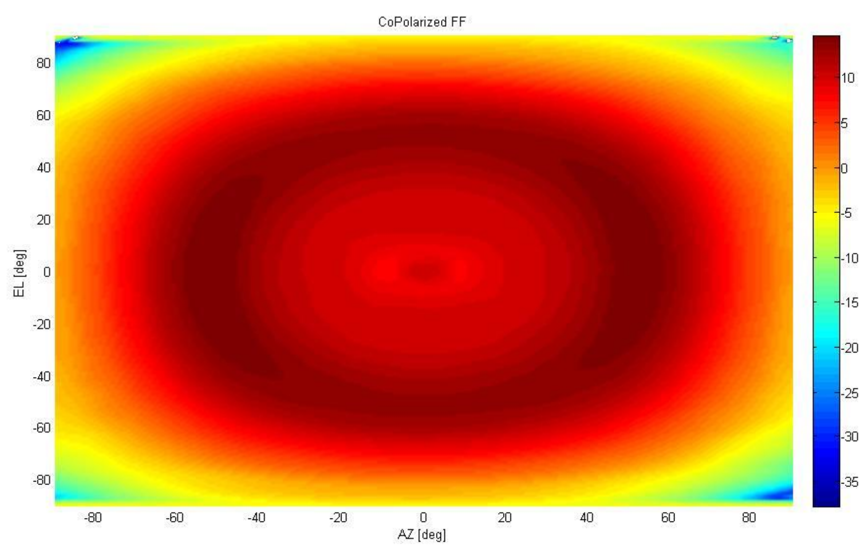

FIGURE 20 - ISOFLUX ANTENNA FF PATTERN

6.1.3 – Base Station Antenna

The base station antenna NF data was acquired with the antenna field maximum pointing away from North Pole direction. The main beam is shifted to -10 degrees in elevation and + 25 degrees in azimuth. This antenna is a Class#2 type antenna according to the classification used in Section 4.4. Its NF data is shown in Figure 21 as a function of (θ, φ) over the complete sphere. After NF-to-FF transformation using NSI2000 we obtain the results shown in Figure 22.

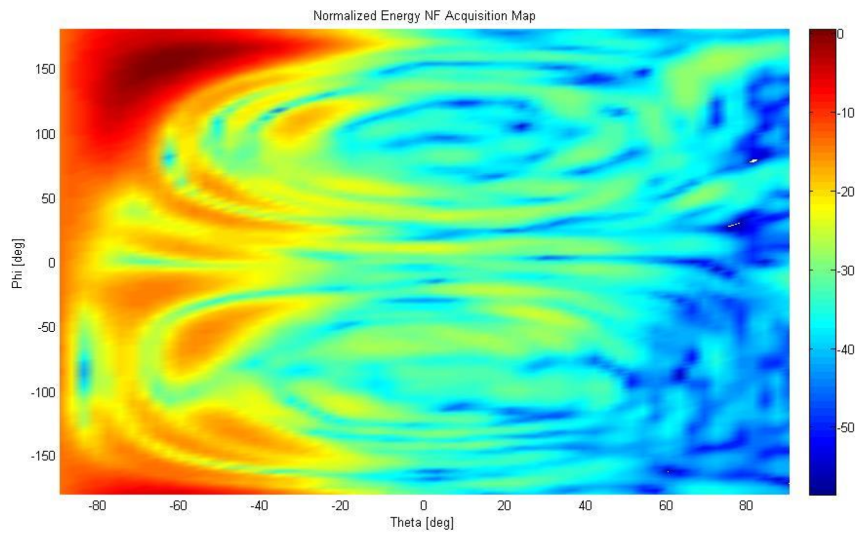

FIGURE 21 - BASE STATION ANTENNA NF PATTERN

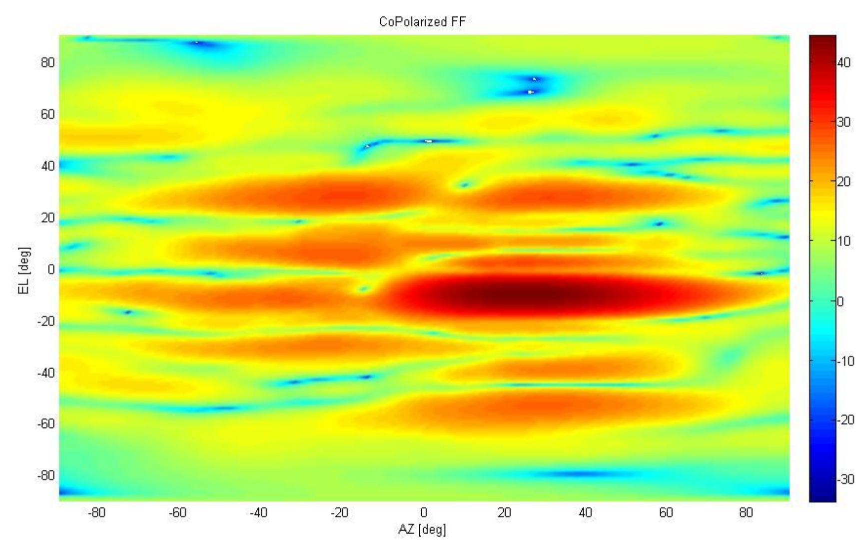

FIGURE 22 – BASE STATION ANTENNA FF PATTERN

6.2 – NF Pre-Conditioning Study

We next examine the impact of NF pre-conditioning using Methods #1 to #3, as presented in Sections 5.5.2 to 5.5.4, respectively. First, since Method #1 and #2 both use linear interpolation, we compare these two methods in Section 6.2.1. We use the FAN AUT as a test case to compare these first two methods. The foundations for Method #1 and #2 are described in Section 5.5 and in Appendix E. It was discovered that the truncation of the radial component that is necessary in Method #2 introduces an inherent amplitude error; this is illustrated in Section 6.2.2.

In Section 6.2.3, Method #3, which uses a SWE approach to perform pre-conditioning, is studied. Since this method gave poor results with the BSA, the method was assessed using a supplemental standard gain horn to validate the obtained results.

Section 6.2.4 provides some conclusions as to why pre-conditioning should be used, and which of the above methods is preferred, irrespective of the decision function used.

6.2.1 – Comparison of the Linear Interpolation Methods for Pre-Conditioning

The FAN antenna, whose NF pattern is presented in Figure 17, is acquired without NF pre-conditioning, using Method #1 and using Method #2. To compare the quality of the interpolation on the spherical grid, an error function is defined between the exact NF and the interpolated NF at every point in space; the expression[12] used is

$$f_{NF_{error}}(\theta_i, \varphi_j) = \frac{\left|E_{NF}^{exact}(\theta_i, \varphi_j)\right| - \left|E_{NF}^{interp}(\theta_i, \varphi_j)\right|}{\left|E_{NF}^{exact}(\theta_i, \varphi_j)\right|} \tag{6.1}$$

$$F_{NF_{error}} = 10 \log f_{NF_{error}} \tag{6.2}$$

where,

[12] Note that this is merely being used to assess the effectiveness of the pre-conditioning methods. This is not a decision function in the sense of Section 4.5.

$$\left|E_{NF}^{exact}(\theta_i,\varphi_j)\right| = \left|\sqrt{E_\theta^{exact}(\theta_i,\varphi_j)^2 + E_\varphi^{exact}(\theta_i,\varphi_j)^2}\right|$$

$$\left|E_{NF}^{interp}(\theta_i,\varphi_j)\right| = \left|\sqrt{E_\theta^{interp}(\theta_i,\varphi_j)^2 + E_\varphi^{interp}(\theta_i,\varphi_j)^2}\right|$$

Using these expressions, Figure 23 and Figure 24 were produced, respectively for pre-conditioning using Methods #1 and #2. Plots (a) in each case represent the interpolated electric field amplitude using pre-conditioning. Plots (b) show the actual acquired electric field amplitude. Plots (c) show $F_{NF_{error}}$ determined from expression (6.2) in decibel.

We can see for both methods that the region where the largest NF amplitudes ("hot spots") are located are reasonably well approximated. Looking at both methods' amplitude error, we can see the fact that there is no amplitude error when ϕ is fixed to 0° and 90° (the error is –∞ dB); this is expected since these two cuts are actual acquired values needed to carry out the pre-conditioning. When we look at the Method #2 amplitude error plot, we see that when θ is fixed to 0°, the North Pole, a very low error is present. This is desirable since the pole should be a single vector value – the pole being a single point in space. As we can see, this is not the case for Method #1, where an error is present all along θ=0°. Thus at the pole, Method #2 is better than Method #1 since it gives a single vector, which is not the case for Method #1. Note that this effect is inherent to the interpolation method.

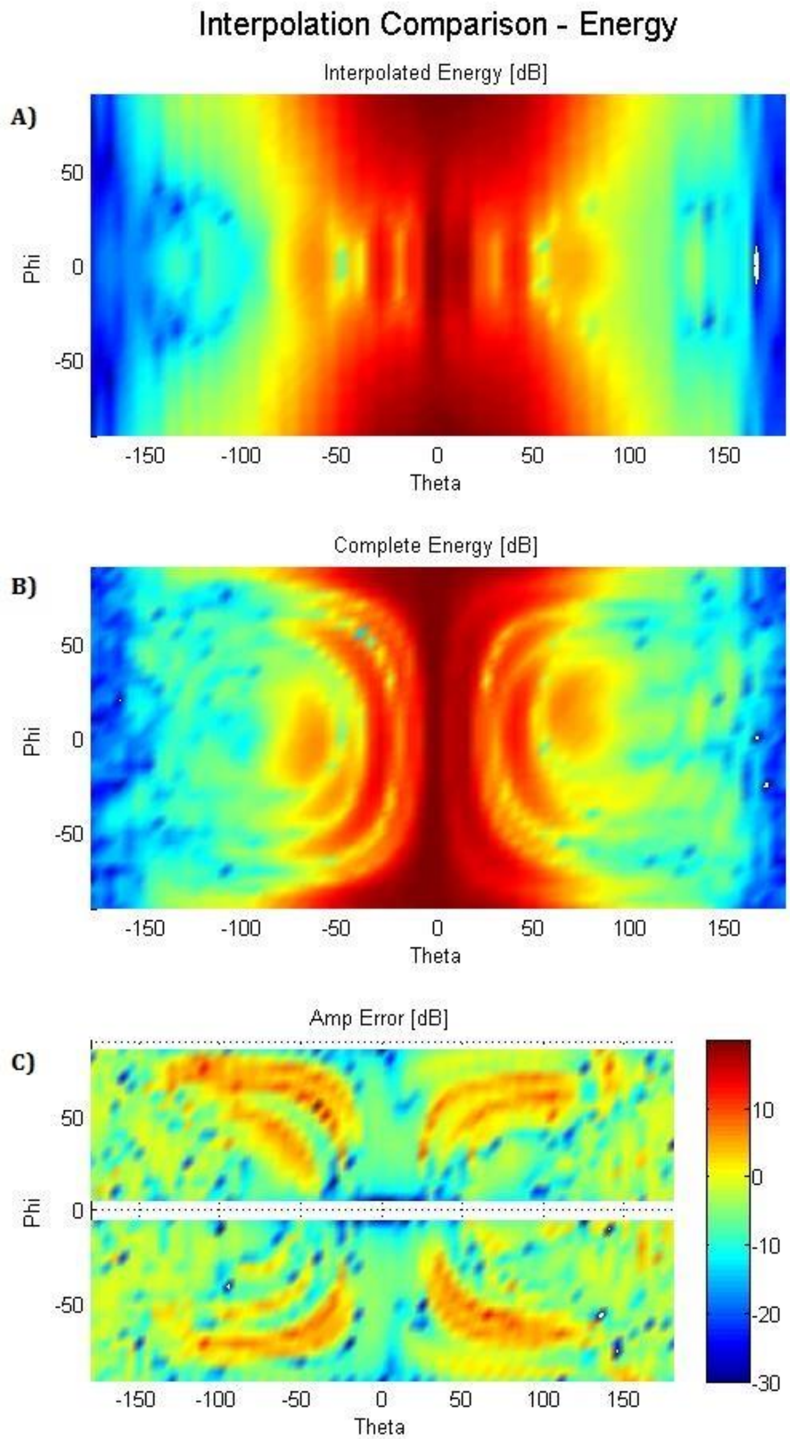

FIGURE 23 – NF PRE-CONDITIONING METHOD #1 AMPLITUDE COMPARISON. A) INTERPOLATED NF ELECTRIC FIELD AMPLITUDE USING METHOD #1, B) ELECTRIC FIELD AMPLITUDE OF THE ACTUAL ACQUIRED NF DATA, C) ERROR FUNCTION DEFINED IN EXPRESSION (6.2)

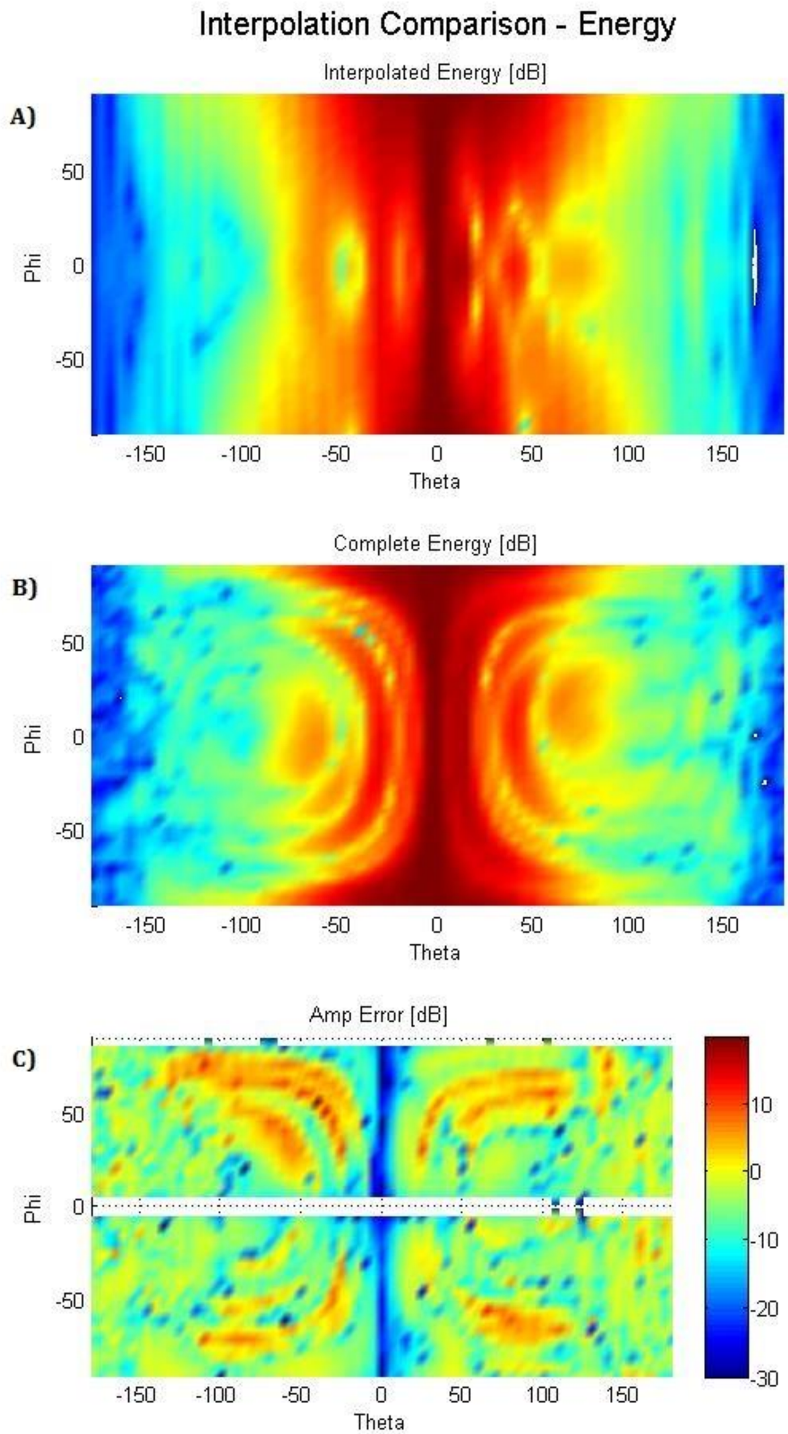

FIGURE 24 - NF PRE-CONDITIONING METHOD #2 AMPLITUDE COMPARISON. A) INTERPOLATED NF ELECTRIC FIELD AMPLITUDE USING METHOD #2, B) ELECTRIC FIELD AMPLITUDE OF THE ACTUAL ACQUIRED NF DATA, C) ERROR FUNCTION DEFINED IN EXPRESSION (6.2)

6.2.2 - Comparative Behavior of Pre-Conditioning Methods #1 and #2 in the Adaptive SNF Algorithm

We next examine the behaviour of the four different decision functions (directivity, change in directivity, maximum pattern error and first side lobe directivity) as the FAN NF data is acquired. It is important to note that the samples acquired from the orthogonal cuts are not counted when computing the percentage of the measurement sphere for the FAN and the SGH. Adding these points will increase the numbers we will later quote by at most 5% of the measurement sphere. The sample count for the BSA does account for the orthogonal cuts. As seen in Figure 25, all three approaches[13] show convergence towards the same final directivity value. Also, we see that even after only a small portion of the measurement sphere is acquired, the directivity computed with NF pre-conditioning used is much closer to its final value than without pre-conditioning.

The convergence is similar in Figure 26, where we also see fewer erratic changes from iteration to iteration when pre-conditioning is employed.

Instead of looking directly at patterns between each iteration, we can have a global overview of the patterns in Figure 27 by looking at the maximum error. We see that when using no pre-conditioning we have the fastest convergence to the final pattern, but the difference is not significant. It is not clear why this is so.

Another interesting parameter to examine is the first side lobe level relative to the main beam level, as presented in Figure 28. The values obtained with pre-conditioning used are more stable and closer to the final value than without pre-conditioning.

Generally the pre-conditioning Method #2 produces more stable values for main beam directivity and the side lobe levels, when compared to Method #1, or without pre-conditioning.

[13] No pre-conditioning ("No Cond"), pre-conditioning using the first method ("Method 1"), and pre-conditioning using the second method ("Method 2").

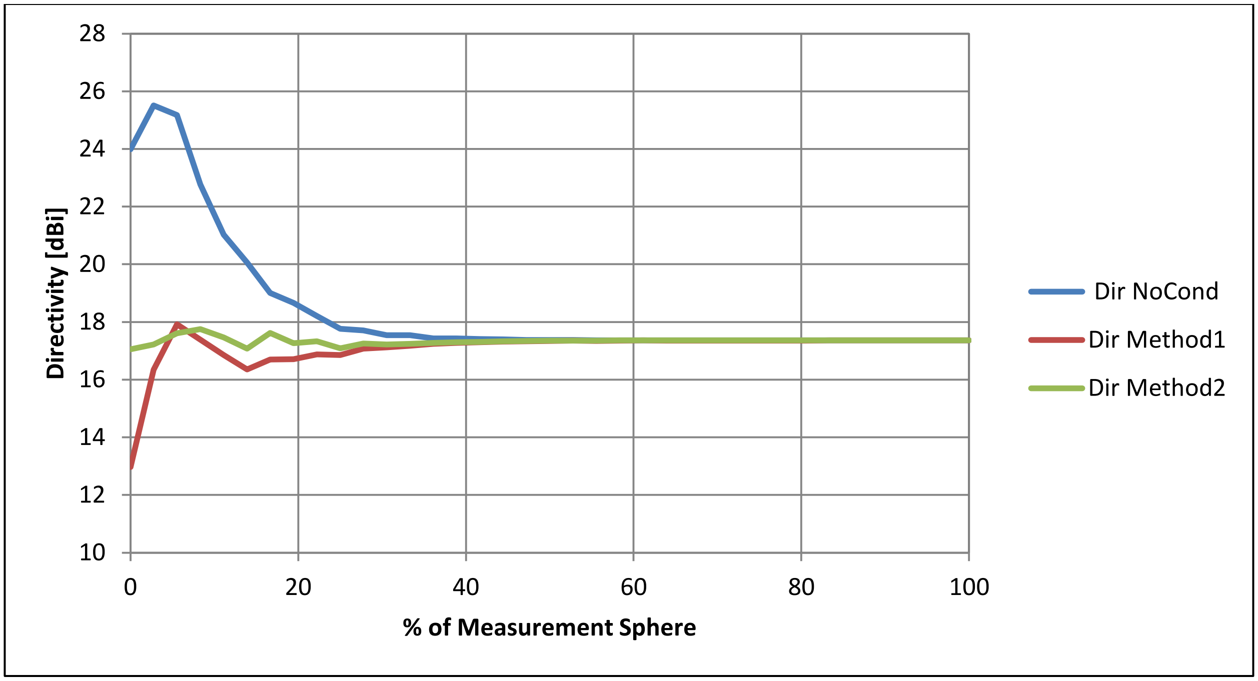

FIGURE 25 - DIRECTIVITY NF PRE-CONDITIONING COMPARISON FOR FAN

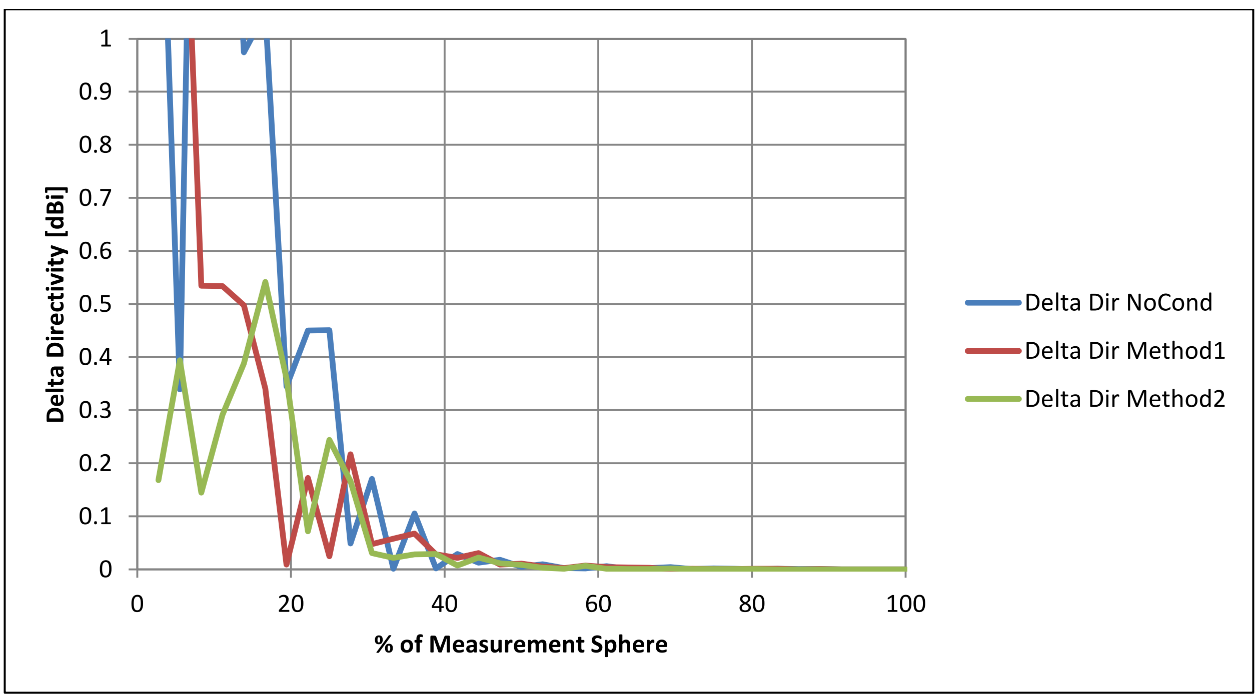

FIGURE 26 - DELTA DIRECTIVITY NF PRE-CONDITIONING COMPARISON FOR FAN

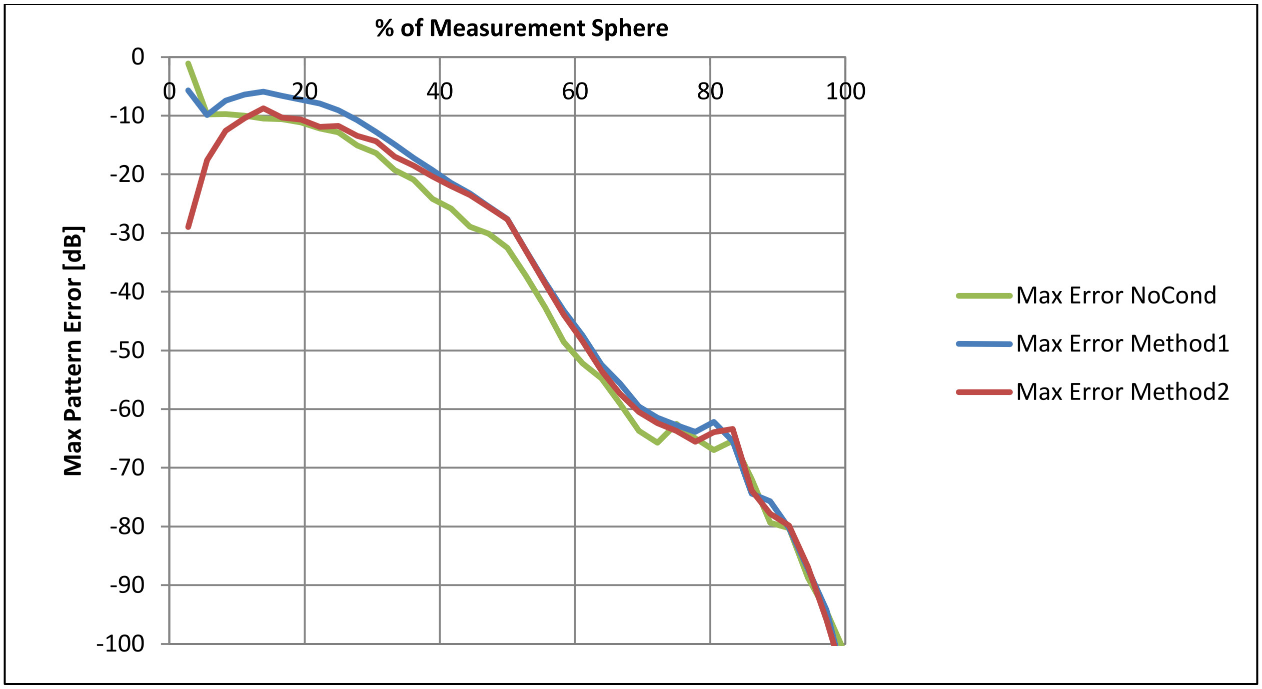

FIGURE 27 - MAXIMAL PATTERN ERROR NF PRE-CONDITIONING COMPARISON FOR FAN

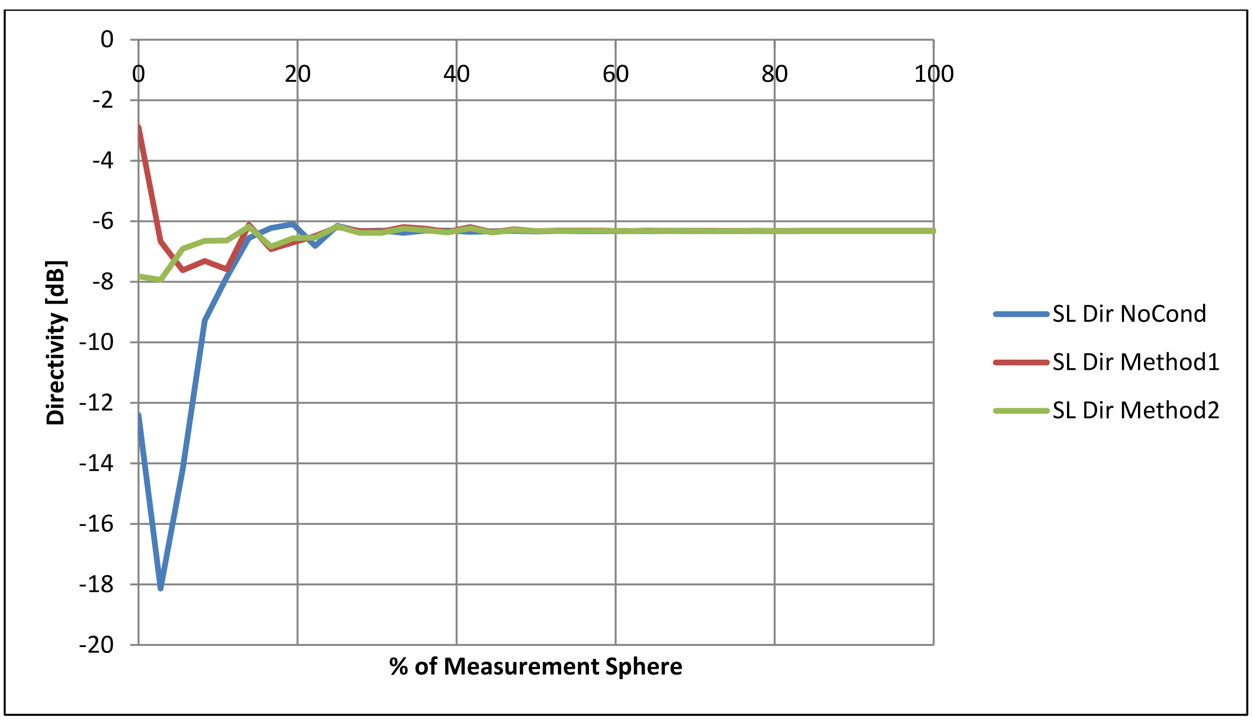

FIGURE 28 - SIDE LOBE DIRECTIVITY NF PRE-CONDITIONING COMPARISON FOR FAN

6.2.3 - Pre-Conditioned Inherent Amplitude Error

As briefly mentioned previously, pre-conditioning Method #2 introduces an inherent amplitude error. This is the case since generally a radial component of the electric field is created when interpolating Cartesian components and projecting them back to spherical components. To assess this error, an artificial NF data array was processed through the NF pre-conditioning algorithms Method #1 and Method #2. This artificial NF data array is filled with unit amplitude field values with a phase of 45°, namely $(1 + j)/\sqrt{2}$ at each NF data point.

A pre-conditioning algorithm that doesn`t create any amplitude error should interpolate perfectly this artificially generated NF data array since it`s the same value at each point. From Figure 29 we clearly see that Method #2 creates the expected amplitude error.

Note that the NF pre-conditioning Method #1 results for the artificial NF data array is not shown, since this pre-conditioning method does not introduce any amplitude error (hence any plot is unremarkable).

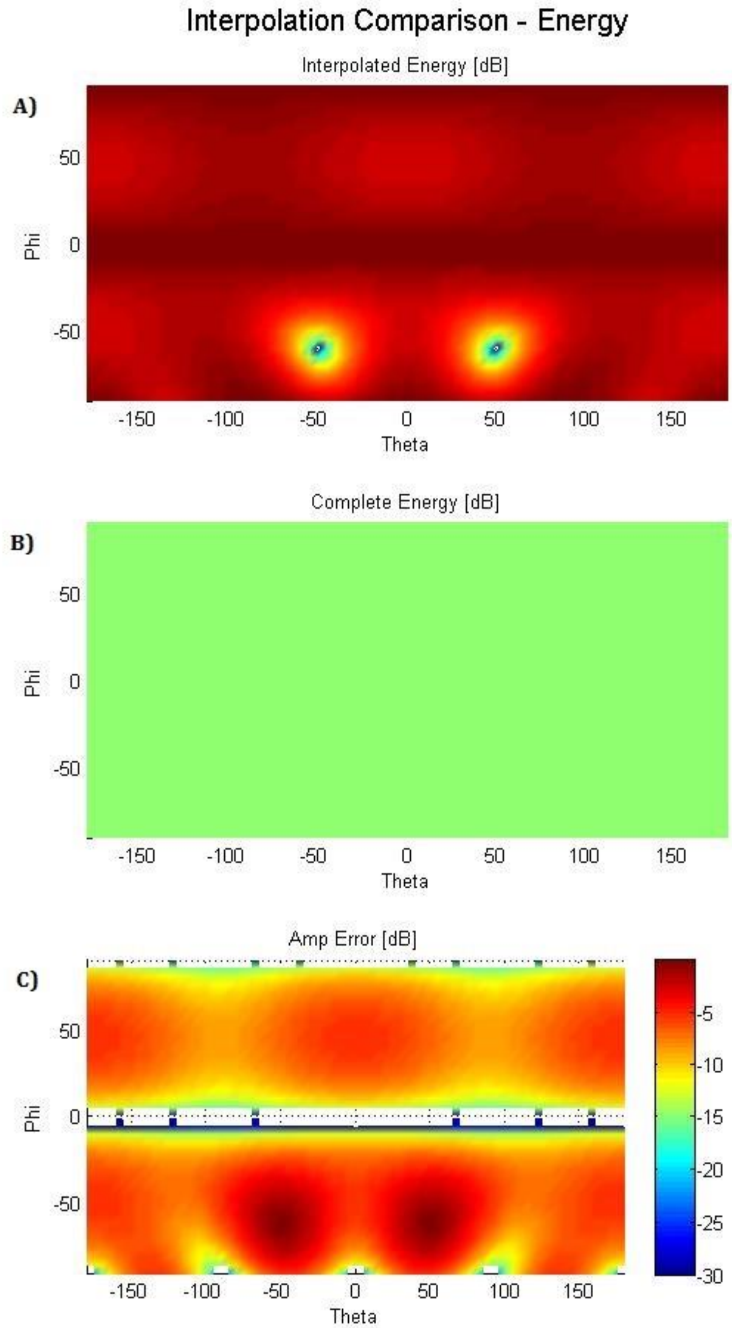

FIGURE 29 – NF PRE-CONDITIONING STUDY OF METHOD #2 USING THE ARTIFICIALLY GENERATED NF DATA ARRAY. A) INTERPOLATED NF ELECTRIC FIELD AMPLITUDE USING METHOD #2, B) ELECTRIC FIELD AMPLITUDE OF THE ACTUAL ACQUIRED NF DATA, C) ERROR FUNCTION DEFINED IN EXPRESSION (6.2)

6.2.4 - SWE Interpolation (Method #3)

The concept presented in Section 5.5.4 is here applied to a BSA in order to determine the effectiveness of this pre-conditioning function. To do so, the two orthogonal cuts are acquired, the function is applied and the pre-conditioned fields are assessed using (6.2). As we can see in Figure 30, this method cannot properly locate the highest amplitude fields on the grid. This method therefore server us little as the goal is to approximate the fields as best as possible from two cuts.

To further support this last statement, the evolution of the directivity and the maximum pattern error for the BSA and the SGH is assessed using no pre-conditioning, using linear interpolation Method #1 pre-conditioning, and using SWE Method #3 pre-conditioning.

As seen in Figure 31, Method #3 gives a similar curve shape to that of acquisition without any pre-conditioning. Since two initial orthogonal cuts were acquired for the pre-conditioning method to be possible, the performance for Method #3 is worse than the acquisition without pre-conditioning. It is clear from this figure that Method #1 is beneficial to the acquisition and that Method #3 is detrimental.

When we look at Figure 32, there is little difference in pattern error between the acquisition without pre-conditioning, the acquisition using Method #1 and the acquisition using Method #3. Therefore in this case the patterns are evolving at similar rate for all three methods.

We next look at the evolution for a different AUT, namely the SGH. Note that the acquisition for this AUT stops at 50%. This is so since only half of the measurement sphere was acquired in the SNF facility. By looking at Figure 33, we clearly see that the linear interpolation (Method #1) is giving a value much closer to the final value than when no pre-conditioning or when Method #3 is used. Method #3 follows closely the evolution of the acquisition without pre-conditioning.

As seen in Figure 34, in this case the AUT radiation pattern is settling faster using Method #1. Using no pre-conditioning or using Method #3 seems to make little difference.

Looking at these results, we can state with confidence that SWE pre-conditioning Method #3 is not beneficial to the acquisition, in some cases is in fact detrimental, and that therefore this method of pre-conditioning will not be studied further.

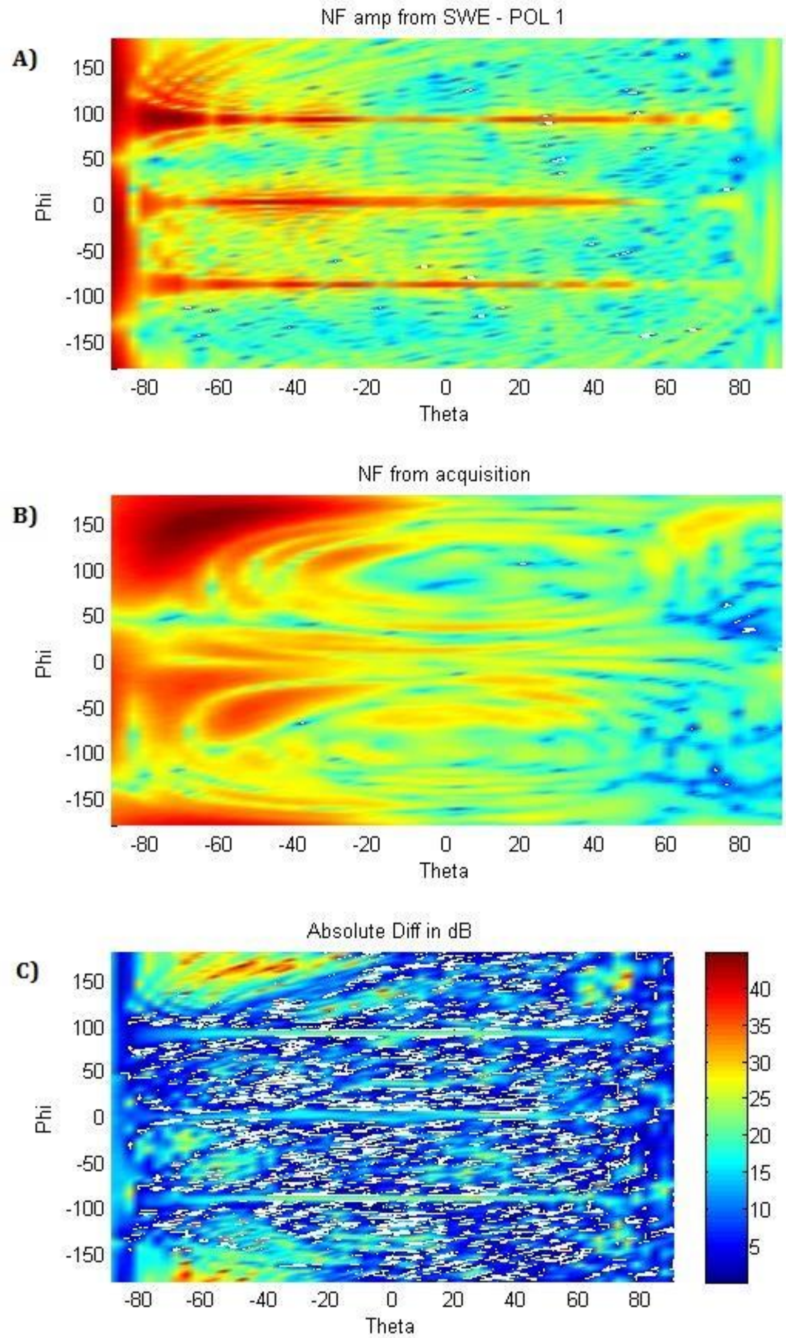

FIGURE 30 - NF PRE-CONDITIONING METHOD #3 AMPLITUDE COMPARISON. A) INTERPOLATED NF ELECTRICAL FIELD AMPLITUDE USING METHOD #3, B) ELECTRICAL FIELD AMPLITUDE OF THE ACTUAL ACQUIRED NF DATA, C) ERROR FUNCTION DEFINED IN EXPRESSIONT (6.2)

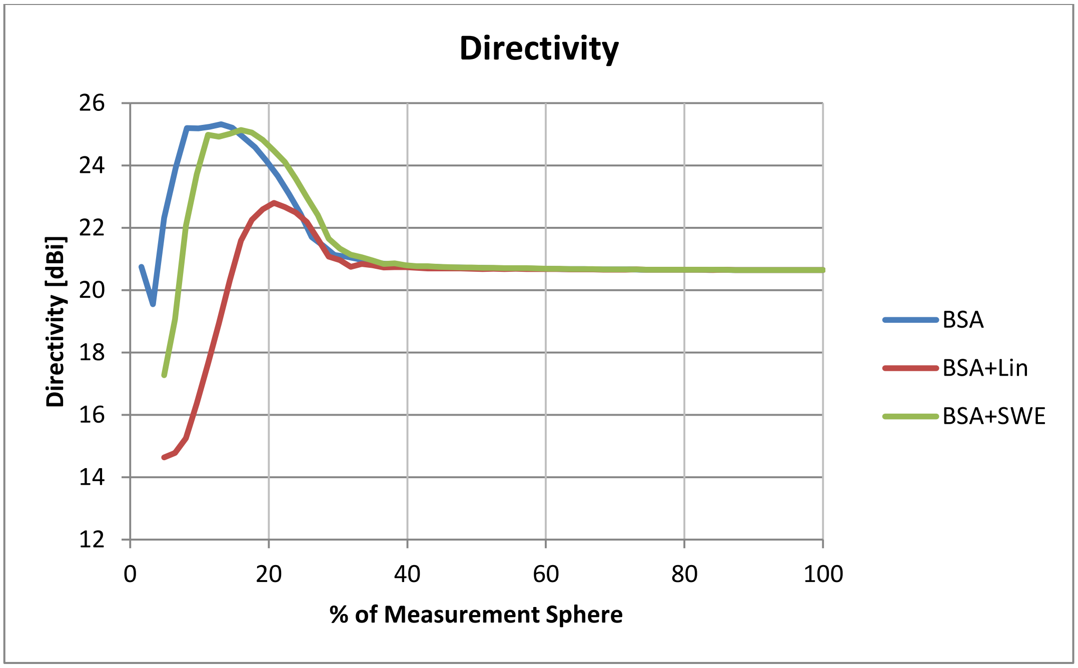

FIGURE 31 - DIRECTIVITY EVOLUTION OF BSA USING NO PRE-CONDITIONING (BSA), USING METHOD #1 (BSA+LIN) AND USING METHOD #3 (BSA+SWE)

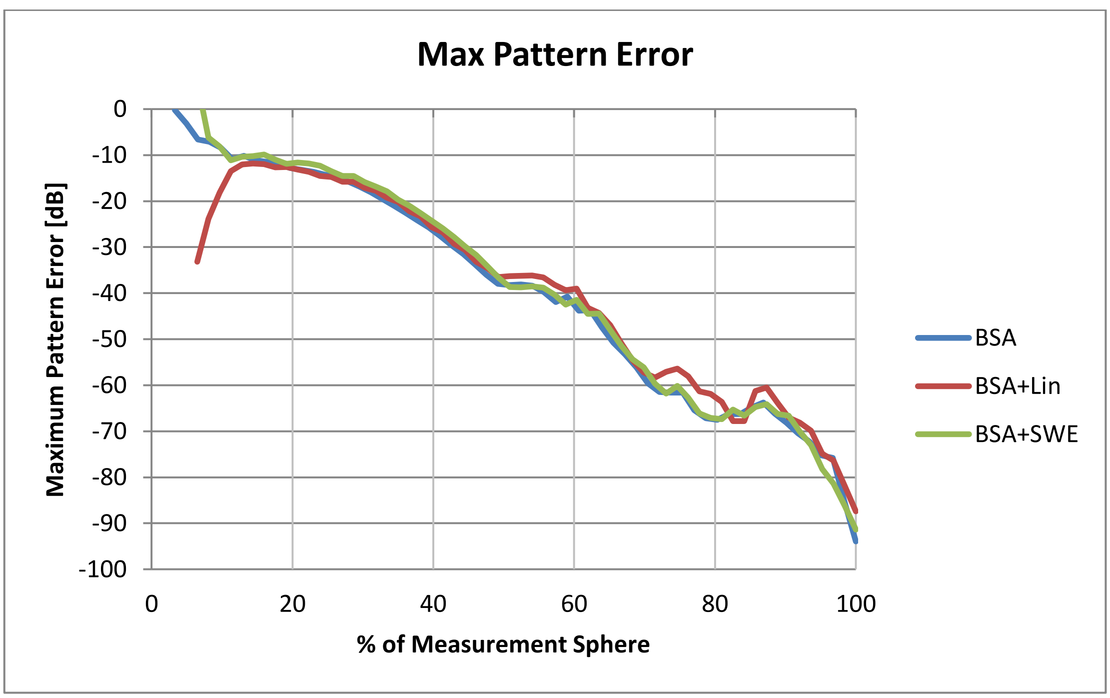

FIGURE 32 - MAXIMUM PATTERN ERROR EVOLUTION OF BSA USING NO PRE-CONDITIONING (BSA), USING METHOD #1 (BSA+LIN) AND USING METHOD #3 (BSA+SWE)

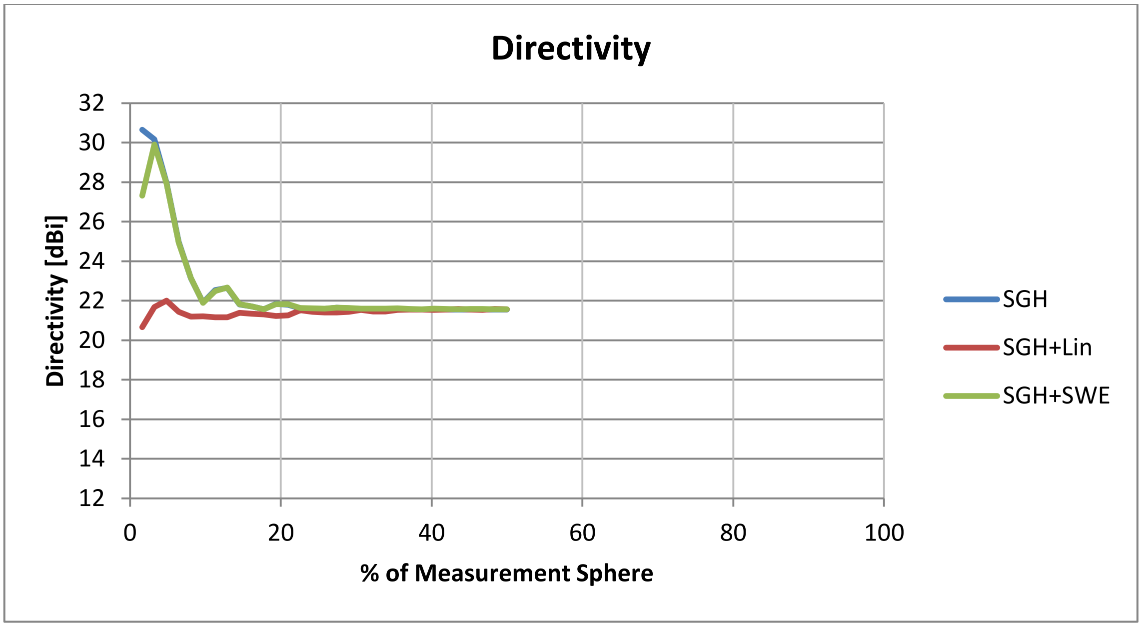

FIGURE 33 – DIRECTIVITY EVOLUTION OF SGH USING NO PRE-CONDITIONING (SGH), USING METHOD #1 (SGH+LIN) AND USING METHOD #3 (SGH+SWE)

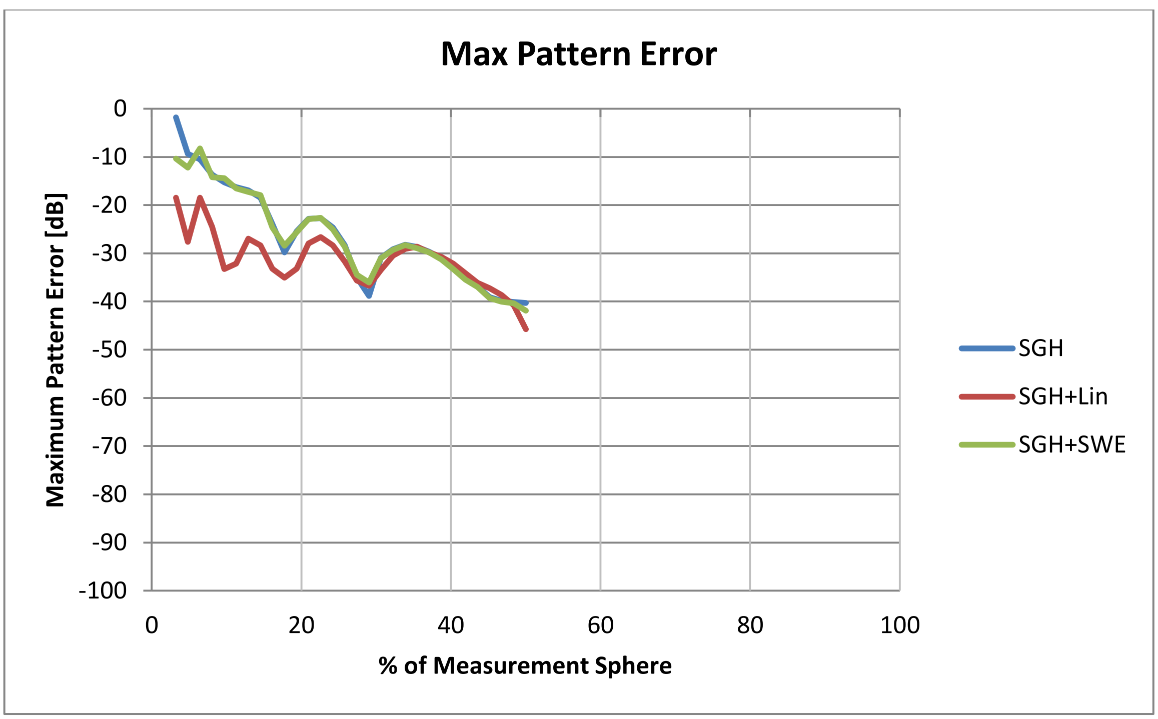

FIGURE 34 - MAXIMUM PATTERN ERROR EVOLUTION OF SGH USING NO PRE-CONDITIONING (SGH), USING METHOD #1 (SGH+LIN) AND USING METHOD #3(SGH+SWE)

6.2.5 - Conclusion on the Usage of NF Pre-Conditioning

In light of what has been observed in Sections 6.2.1, 6.2.2 and 6.2.3, we can draw some conclusions on the usage of pre-conditioning. Since Method #3 was discarded as a valid pre-conditioning function in Section 6.2.3, we now have to choose between Method #1 and Method #2, which both use linear interpolation. In the two cases the decision function values using pre-conditioning are usually closer to their final values than when pre-conditioning is not used. This latter fact might help for automated decision functions and will help to get a faster convergence. Thus the usage of pre-conditioning is recommended. Also, some acquisition rules might benefit from the knowledge of the main beam position in space for an antenna pointing away from North Pole, and this knowledge can be estimated from pre-conditioning. By looking at the differences between Method #1 and Method #2, we see that Method #2 provides values closer to the final value than Method #1 for the specific case examined. But, by looking at the inherent amplitude error, one could doubt the true value of this method in general. For that reason NF pre-conditioning with Method #1 is seen as more robust and will be used through the rest of this work to extract results for decision functions and acquisition rules.

6.3 - Acquisition Rule Comparison

To compare the acquisition rules defined in Section 5.3, we use the three AUTs selected (FAN, ISO and BSA) and perform sampling using acquisition rule #0 (Highest Samples First), #1 (Increasing Cap) and #2 (Guided Threshold). Then the results are compared using the four decision functions (main beam directivity, delta directivity of main beam, maximum pattern error and the side lobe level) described in Section 5.4. The various acquisition rules are plotted against the percentage of acquired measurement sphere.

6.3.1 - Fan Beam Antenna Acquisition Rule Comparison

Looking at the directivity results for the FAN, as seen Figure 35, we see first that all three acquisition rules converge to the final value of 17.3 dBi. Also, all three rules have the ability to acquire the complete measurement sphere in the event the decision function "tells us" to do so, as required by the design guide lines for acquisition rules. We must also note for every decision function that acquisition rule #2 starts "later" as its first iteration acquires a good portion of the measurement sphere, as explained in Section 5.3.3. Acquisition rule #2 converges the fastest (i.e. in the fewest iterations). But the difference is small compared to acquisition rules #1 and #0, and thus it is difficult to clearly state that one rule is superior to the others. We note that acquisition rule #0 does not in fact function as a lower bound , which runs counter to what we expected when defining it in Section 5.3, and is likely due to the use of NF pre-conditioning[14]. Acquisition rule #0 converge sat 41% of the full measurement sphere, acquisition rule #1 at 36% of the measurement sphere, and acquisition rule #2 at 39%.

We can see similar behavior by looking at the delta directivity in Figure 36, but this time the plot is more erratic and thus would not be useful for automated decision-taking. More will be said on this last point in Section 6.4.

Looking at the maximum pattern error (Figure 37), we see that after 40% of the sphere has been sampled the maximum pattern error for all three acquisition rules is still decreasing. When less than half the measurement sphere has been acquired acquisition rule #0 is converging faster towards the final pattern, but it stays "longer" with some small errors until it drops sharply when over 80% of the measurement sphere has been acquired. At some point acquisition rule #1 and #2 are giving patterns with less error than acquisition rule #0, with similar numbers of samples. If a maximum pattern error decision function threshold of -40dB is selected, then acquisition rule #0 would take 73% of the measurement sphere to reach it, acquisition rule #1 would take 58%, and acquisition rule #2 would take approximately 72%.

When the side lobe level is required, acquisition rule #2 exhibits faster convergence towards the final level, as seen in Figure 38. If an error of $\pm$0.1 dB is used for the side lobe level, then acquisition rule #0 requires 37% of measurement sphere, acquisition rule #1 need 44%, and acquisition rule #2 only 22%.

[14] Nevertheless, we will continue to show results using acquisition rule#0 in the sections to follow.

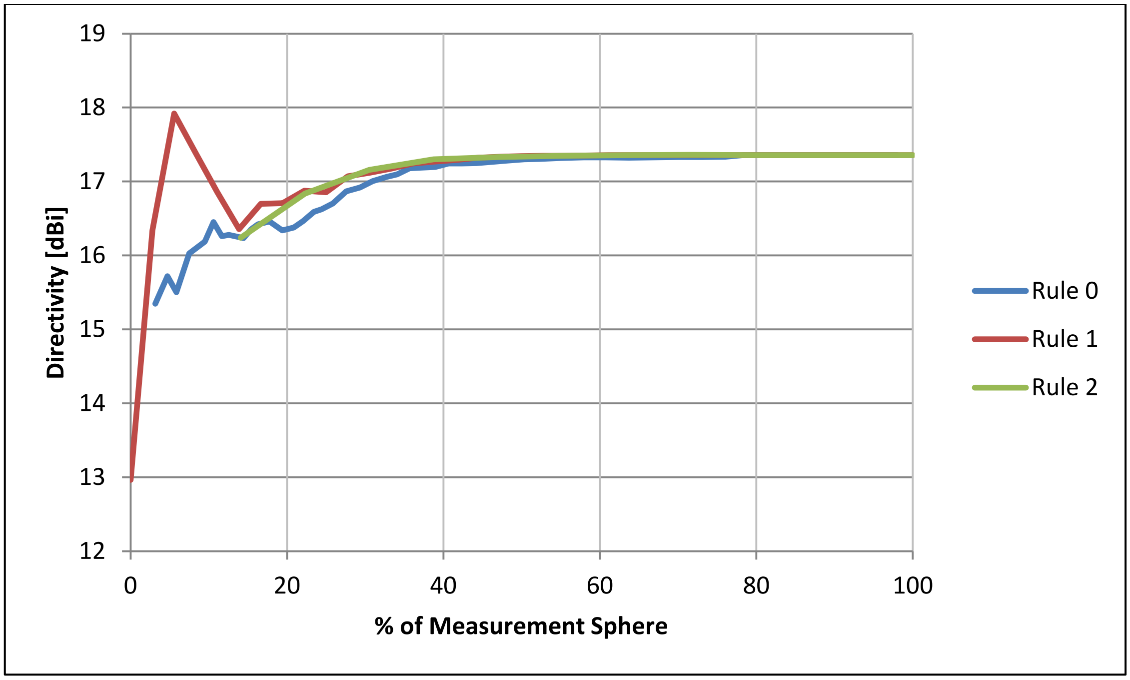

FIGURE 35 - ACQUISITION RULE COMPARISON OF DIRECTIVITY FOR FAN ANTENNA

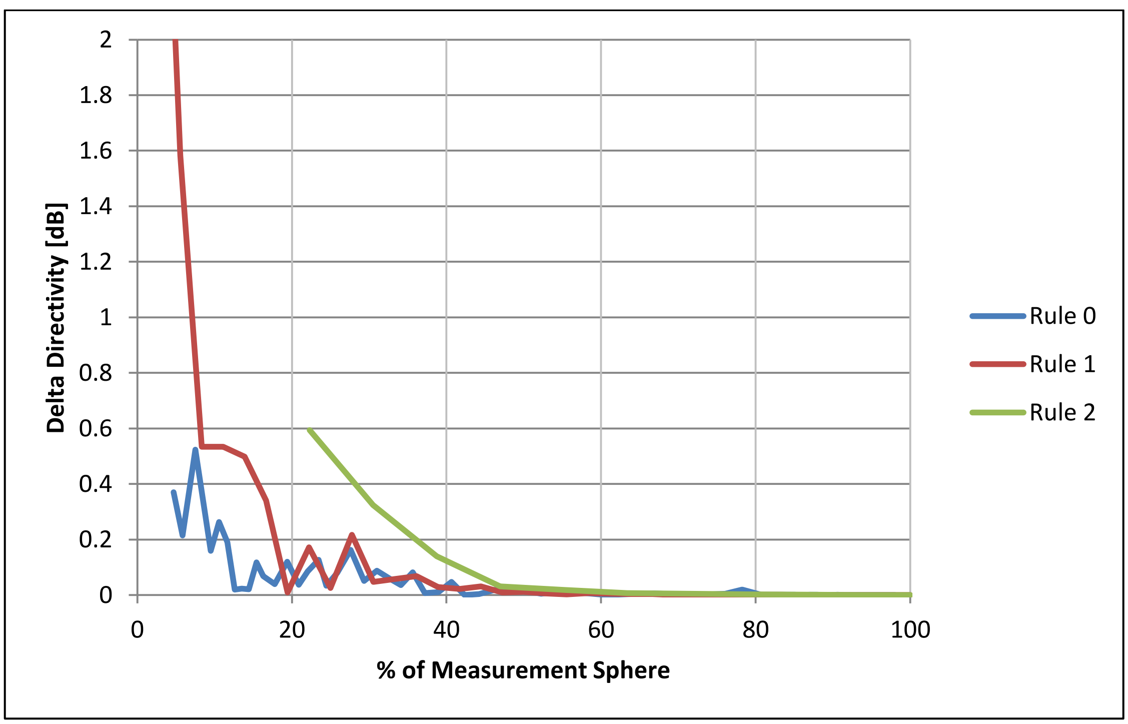

FIGURE 36 - ACQUISITION RULE COMPARISON OF DELTA DIRECTIVITY FOR FAN ANTENNA

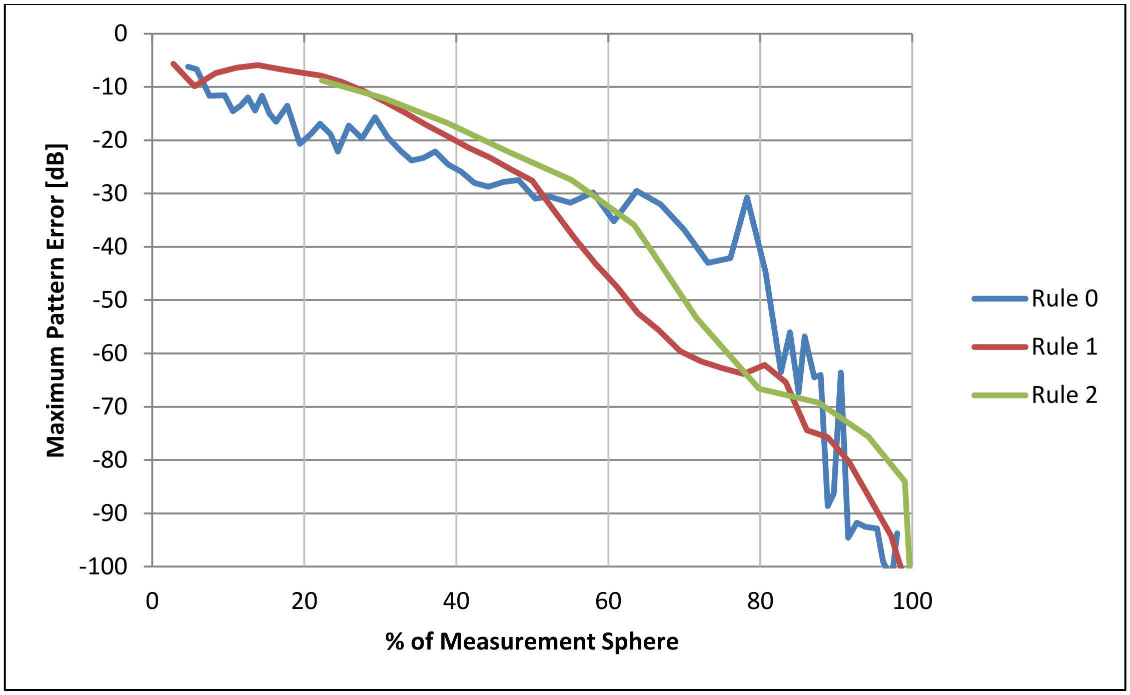

FIGURE 37 - ACQUISITION RULE COMPARISON OF MAXIMUM PATTERN ERROR FOR FAN ANTENNA

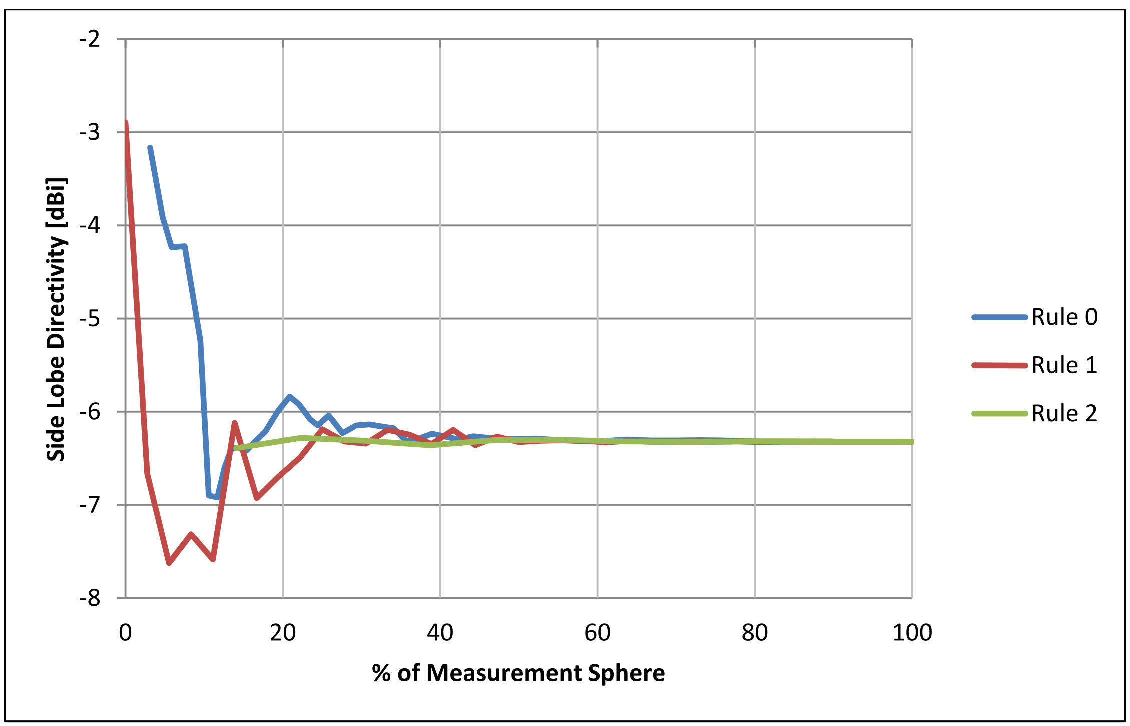

FIGURE 38 - ACQUISITION RULE COMPARISON OF SIDE LOBE DIRECTIVITY FOR FAN ANTENNA

6.3.2 - Isoflux Antenna Acquisition Rule Comparison

For the ISO antenna directivity in Figure 39, we see that all three acquisition rules converge to the final expected value of 6.98 dBi. While acquisition rule #0 converges faster towards the final value for a small number of samples, at 45% of the measurement sphere all three acquisition rules are indistinguishable. Since this antenna has a low directivity, acquisition rule #2 must acquire a large portion of the measurement sphere as its initial iteration; thus it starts iterating at 43% of measurement sphere. If the final directivity is to be determined to a tolerance of $\pm$0.1 dB, acquisition rule #0 would need 42% of measurement sphere to reach the final directivity, the acquisition rule #1 takes 44%, and acquisition rule #2 takes 43%. Indeed in this case the first iteration of acquisition rule #2 was enough to obtain the final directivity to within 0.1 dB.

In Figure 40 we see the delta directivity for the ISO antenna. After 50% of the measurement sphere has been acquired the results for all three acquisition rules do not vary by much. This suggests that the final directivity value has been reached.

The maximum pattern error, as seen in Figure 41, is very similar in behaviour for all three acquisition rules. If a threshold of -40 dB is set for this decision function, then acquisition rule #0 would halt at 61%, acquisition rule #1 at 61%, and acquisition rule #2 at 62% of the measurement sphere. Thus no one acquisition rule offers a significant advantage over the other here.

The side lobe level is shown in Figure 42. Here we can clearly see that acquisition rule #0 has a convergence towards the final value a lot faster than the two other acquisition rules. We see that acquisition rule #1 needs to reach across the side lobe position in the NF array to start converging towards the final value. Here acquisition rule #2 doesn`t provide much information as its first iteration already includes the first side lobe completely. Hence no evolution takes place.

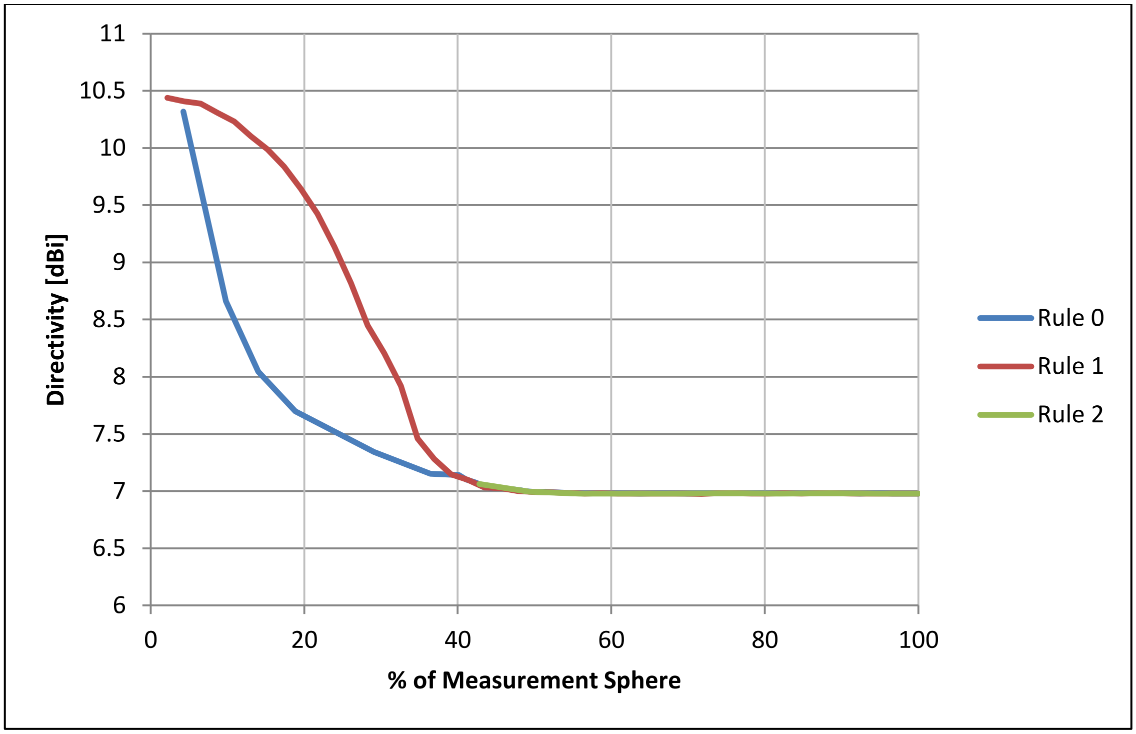

FIGURE 39 - ACQUISITION RULE COMPARISON OF DIRECTIVITY FOR ISO ANTENNA

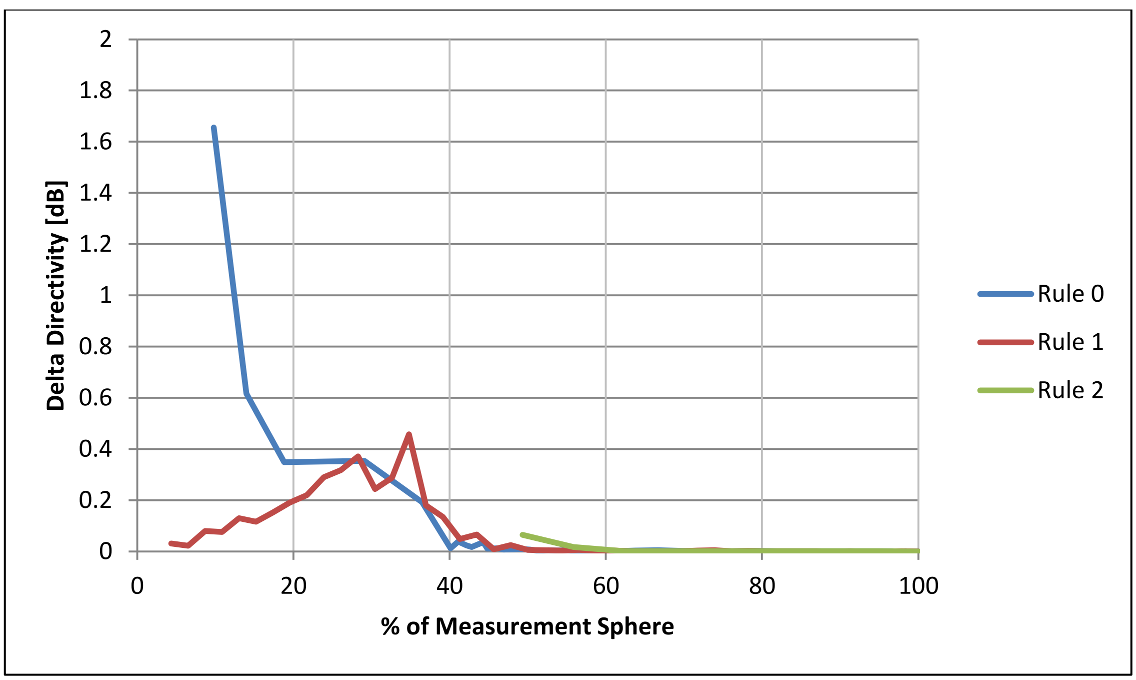

FIGURE 40 - ACQUISITION RULE COMPARISON OF DELTA DIRECTIVITY FOR ISO ANTENNA

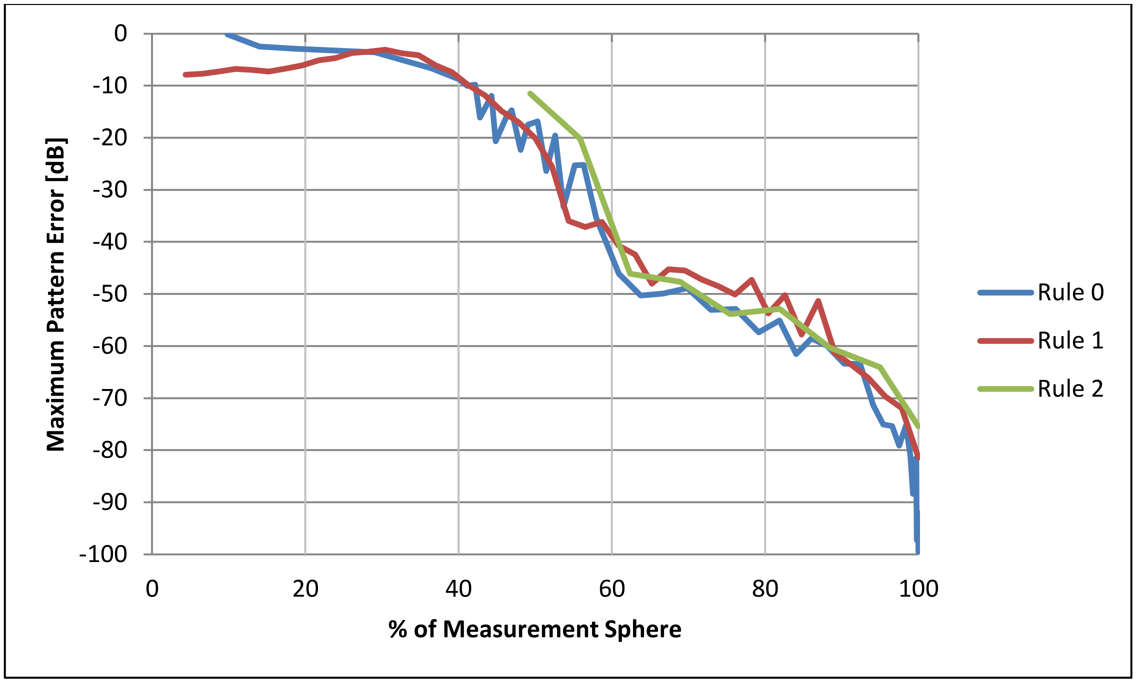

FIGURE 41 - ACQUISITION RULE COMPARISON OF MAXIMUM PATTERN ERROR FOR ISO ANTENNA

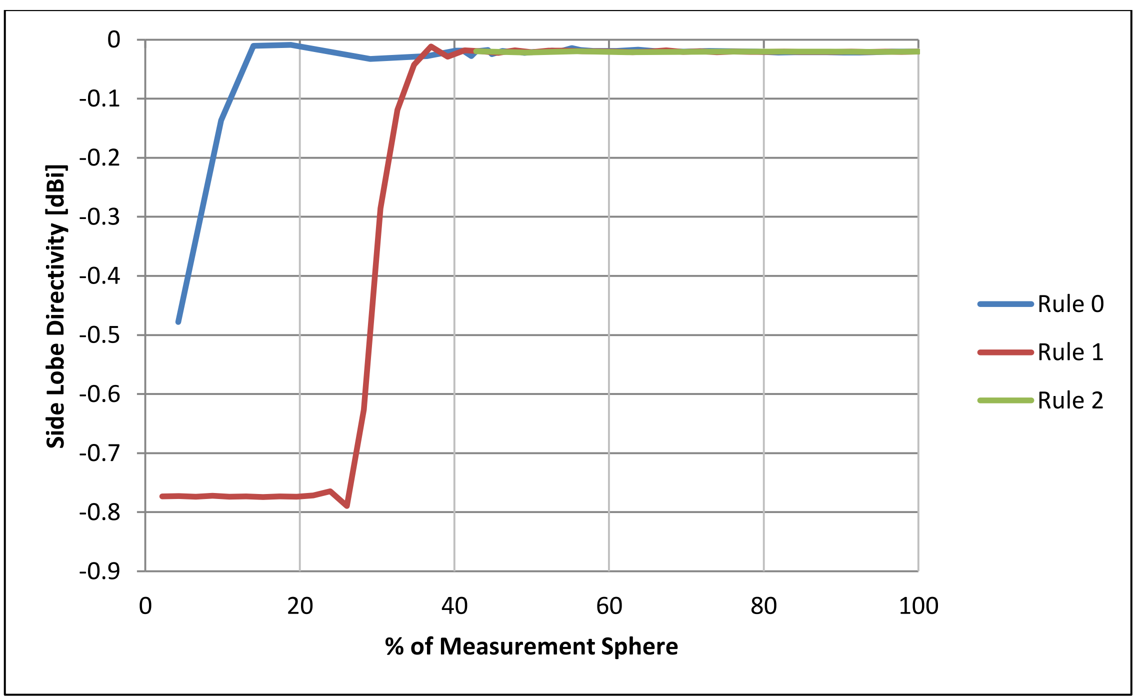

FIGURE 42 - ACQUISITION RULE COMPARISON OF SIDE LOBE DIRECTIVITY FOR ISO ANTENNA

6.3.3 - Base Station Antenna Acquisition Rule Comparison

The interesting characteristic of the BSA antenna is that it's a non-North Pole pointing antenna. This fact presents an interesting case for the acquisition rules devised here, since they all start at the North Pole. The acquisition rule #2 threshold was set high enough so the algorithm can actually "jump" across the initial gap and reach the main beam. We will show the acquisition progress for this acquisition rule #2 in a little more detail before continuing with the comparison of the three rules. This evolution is presented in Figure 43. The detailed acquisition information is presented at iteration numbers 2, 5 and 11. For each iteration the following figures are plotted:

A) The NF Acquisition Map: This surface plot is the E-field amplitude at each point on the measurement sphere. The amplitude is presented in decibels and is normalized to the NF peak value.
B) Normalized CoPol FF: The co-polarized FF based on the NF samples acquired is presented. The amplitude is normalized to the FF peak value. Note that this plot presents the 3D FF pattern of the antenna in AZ-EL fashion.
C) Azimuth CoPol Cut and Error Function: Instead of looking at 3D plots, here we present the AZ cut of the FF. The cuts (both AZ and EL cuts) are passing through the peak of the FF, in this case at AZ = +25° and EL = -10°. The cut from the error function is presented as well. From that error cut we can see that the pattern error diminish as the acquisition goes.
D) Elevation CoPol Cut and Error Function: Similar to the plot C), we present the FF co-polarized cut and the error function cut for elevation.

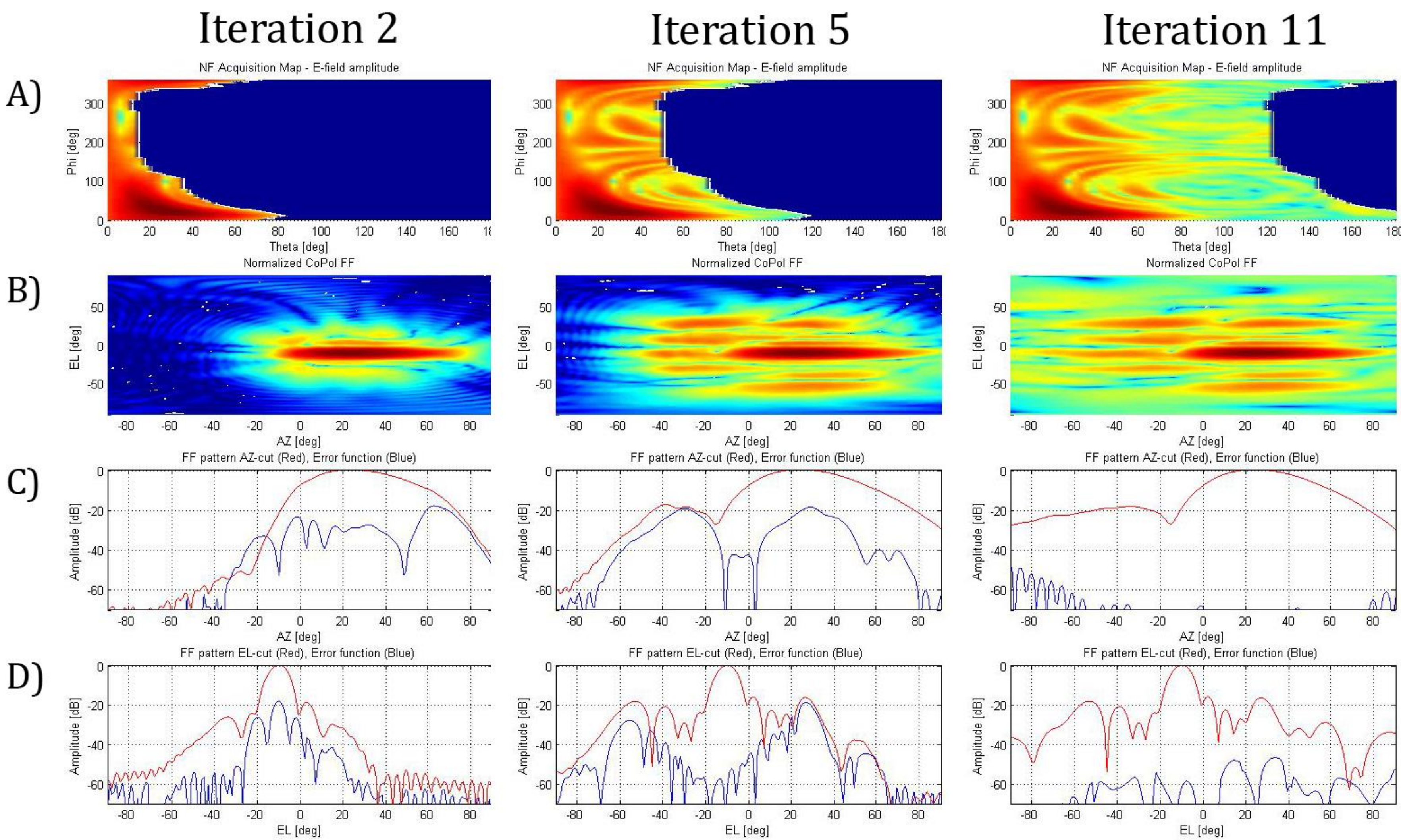

FIGURE 43 - PROGRESSION OF ACQUISITION FOR BSA ANTENNA USING ACQ. RULE #2. A) NF ACQUISITION MAP, B) NORMALIZED COPOL FF, C) AZIMUTH COPOL CUT AND ERROR FUNCTION, D) ELEVATION COPOL AND ERROR FUNCTION

By looking at Figure 44, we again appreciate the fact that all three acquisition rules are converging towards a same value of 20.65 dBi. Here we clearly see the advantage of acquisition rule #2 over acquisition rule #1. With the initial iteration, the acquisition rule #2 is already very close to the final value, and with less than 25% of the measurement sphere acquired the directivity is within $\pm$0.1 dB of the final value. Acquisition rule #1 takes 38% of the measurement sphere to be within that same range. Acquisition rule #0 does slightly better than acquisition rule #2 by converging in 22% of the measurement sphere. Since acquisition rule #1 is an increasing cap, it is interesting to see the peak in directivity when the acquisition rule samples the region of the main beam. Refer to Figure 21 to recall the NF pattern of the BSA antenna.

Looking at the delta directivity in Figure 45, it is difficult to clearly identify a halting point, since the function is very oscillatory for acquisition rule #0 and #1. Nonetheless, after 35% of the measurement sphere for all three acquisition rules we see that the directivity is stable enough to stop the acquisition.

The maximum pattern error for this antenna is more difficult to interpret that for the FAN antenna and the ISO antenna. The curves are different for the three acquisition rules. If the selected threshold of the decision function is set to -40 dB, the acquisition rule #0 would stop at 79%, the acquisition rule #1 at 61% and acquisition rule #2 at 74% of the measurement sphere. As one can see in this case, if another threshold was selected, the order from the fastest convergence to the slowest would be different.

The difference in acquisition rules is much more pronounced when looking at side lobe level, as seen in Figure 47. Acquisition rule #0 reaches within 0.1 dB of the final value of the side lobe level at 52%, acquisition rule #1 at 26%, and acquisition rule #2 at 34% of the measurement sphere. Hence here the acquisition rule #1 reaches the final value the fastest. The reason being that the side lobe is well located for acquisition rule #1 to go over it quickly.

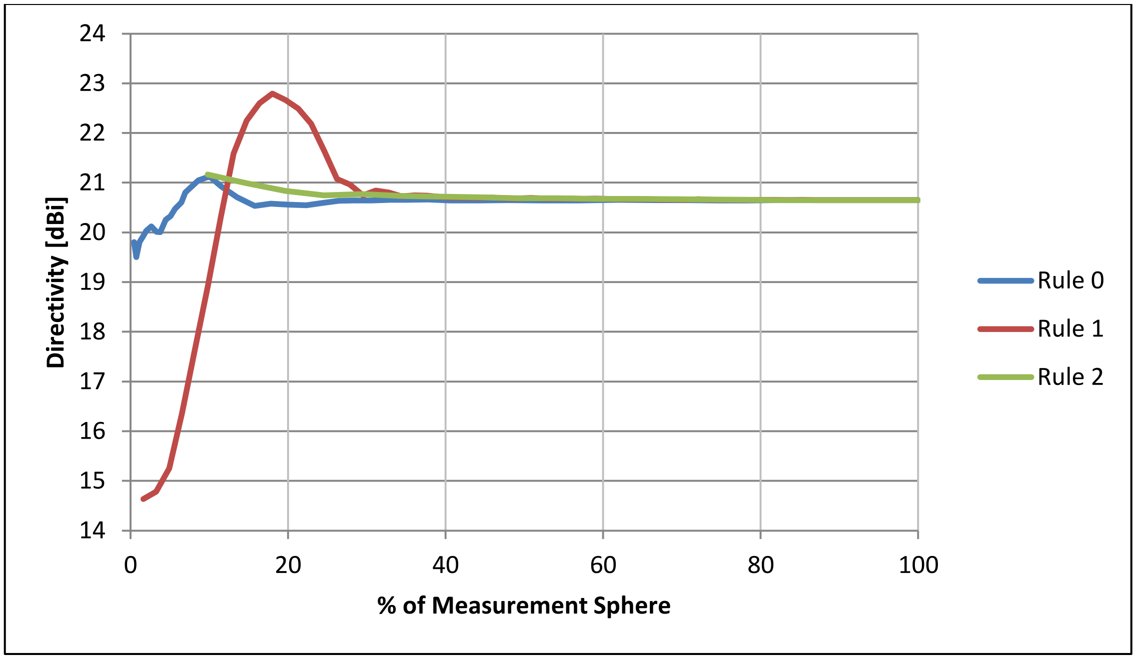

FIGURE 44 - ACQUISITION RULE COMPARISON OF DIRECTIVITY FOR BS ANTENNA

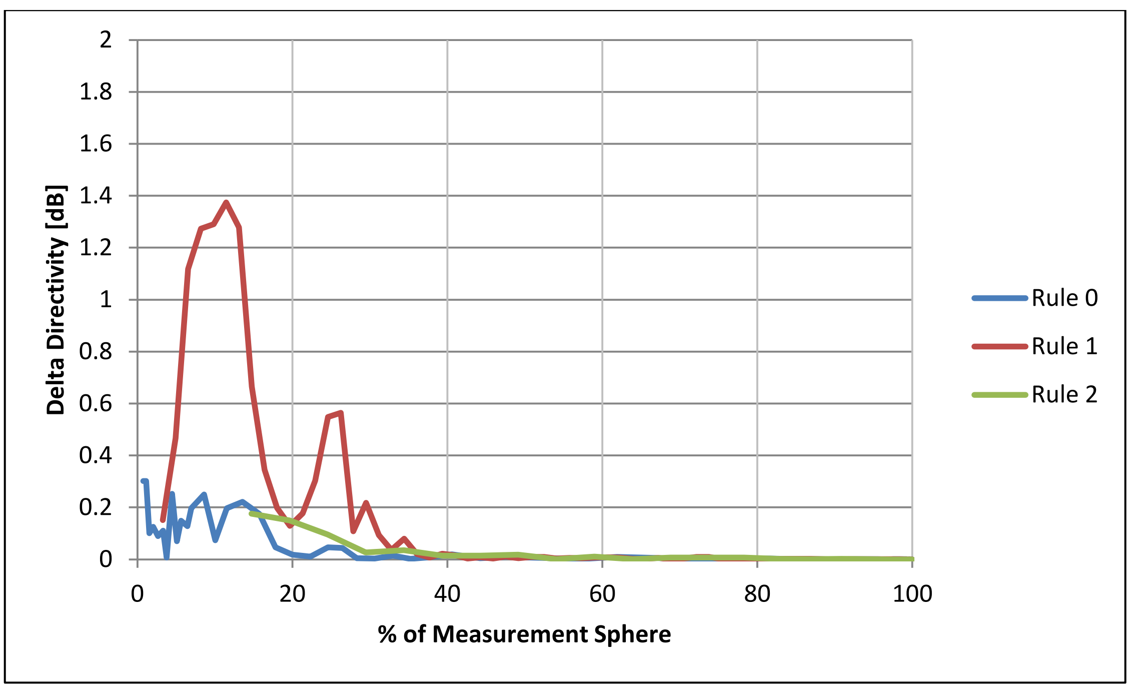

FIGURE 45 - ACQUISITION RULE COMPARISON OF DELTA DIRECTIVITY FOR BS ANTENNA

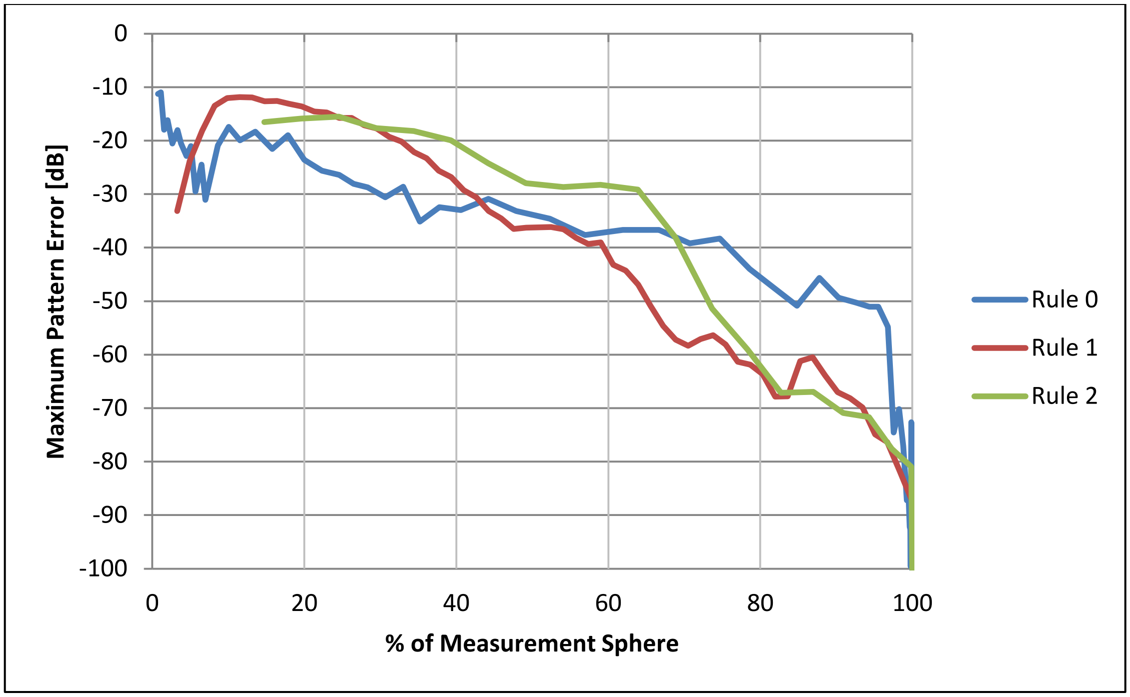

FIGURE 46 - ACQUISITION RULE COMPARISON OF MAXIMUM PATTERN ERROR FOR BS ANTENNA

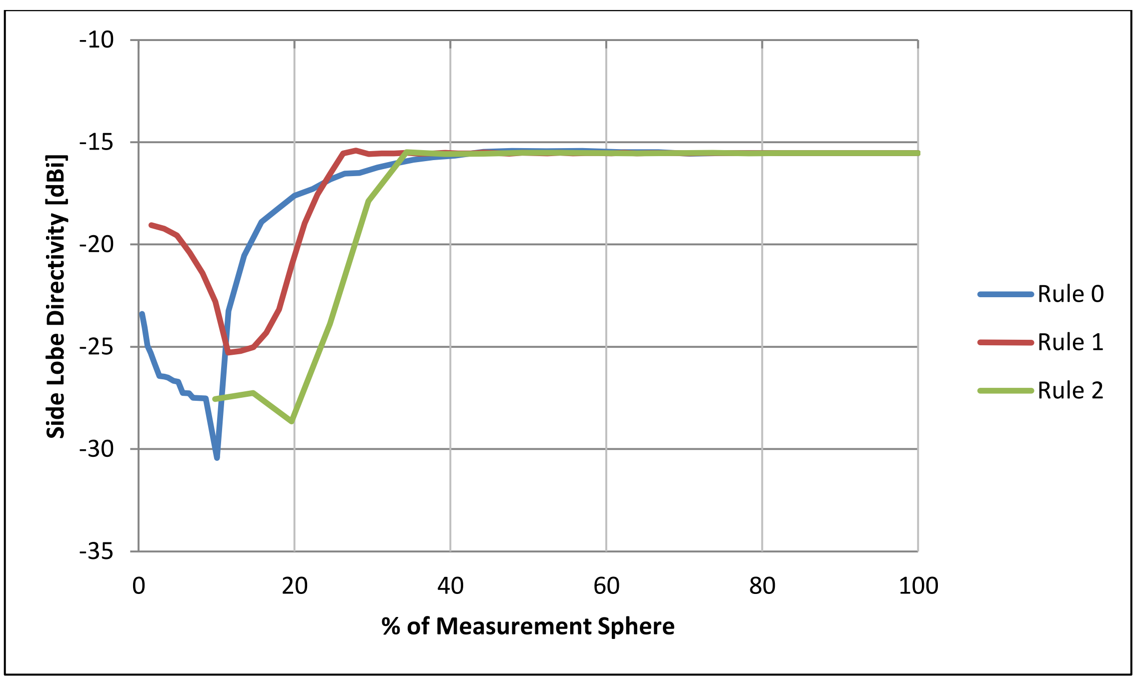

FIGURE 47 - ACQUISITION RULE COMPARISON OF SIDE LOBE DIRECTIVITY FOR BS ANTENNA

6.3.4 - Compiled Results and Comments on Acquisition Rules Studied

To compare the various acquisition rules against the three antennas tested, the results were compiled in Table 2 to put into perspective what has been written so far in Section 6.3. Recall that the selected decision functions were :

- Main beam absolute directivity within $\pm$0.1 dB of the final directivity after oscillation, if any.
- Delta directivity less than 0.1dB. Unused for decision function, more will be said on that point in Section 6.4.
- Maximum pattern error of less than -40 dB between iterations.
- Side lobe directivity within $\pm$0.1 dB of the final value after oscillations, if any.

The Table 2 is filled with the percentage of the measurement sphere acquired when a particular acquisition rule reaches the decision function criterion. A coloring scheme outlines which of the three acquisition rules perform better for an antenna using a specific decision function.

	Directivity Within $\pm$0.1 dB	**Delta Directivity**	**Maximum Pattern Error -40 dB**	**Side Lobe Directivity Within $\pm$0.1 dB**
FAN – Rule 0	41%	*	73%	37%
FAN – Rule 1	36%	*	58%	44%
FAN – Rule 2	39%	*	72%	22%
ISO – Rule 0	42%	*	61%	14%
ISO – Rule 1	44%	*	61%	35%
ISO – Rule 2	43%	*	62%	43%
BS – Rule 0	22%	*	79%	52%
BS – Rule 1	38%	*	61%	26%
BS – Rule 2	25%	*	74%	34%

TABLE 2 - PERCENTAGE OF MEASUREMENT SPHERE TO REACH THE DECISION FUNCTION FOR FAN, ISO AND BS ANTENNAS ACQUIRED USING RULE #0, #1 AND #2

Looking at the FAN antenna, it is clear that the acquisition rule #0 in this case is the worst choice for fast convergence; the absolute directivity and pattern error were the slowest to converge and the side lobe directivity is in 2^{nd} place. Acquisition rule #1, on the other hand, offers the best performance. It takes slightly more than a third of the measurement sphere to obtain the final directivity value and slightly more than half the sphere to get a pattern with maximum error less than -40dB.

For the ISO antenna, this time acquisition rule #0 is clearly the best choice one can make. For every decision function this acquisition rule is the fastest to converge, but of course it is not a practical scheme. Note that the difference is marginal between all three acquisition rules when we look at the absolute directivity. The difference is also marginal for the maximum pattern error. For side lobe level, acquisition rule #1 is certainly not the best choice, but we can scarcely reach conclusions about acquisition rule #2 since its first iteration already includes the side lobe.

The BSA antenna, which is a non-North Pole pointing antenna, seems to be best acquired by acquisition rule #1. It is true that this acquisition rule takes more time to converge for the absolute directivity but the advantage is clear when we look at the maximum pattern error and the side lobe level. Acquisition rule #2 is second with good values for all decision functions.

With the above information from the three AUTs few points can be made:

- For absolute directivity measurement, in the three cases presented, acquisition rule #2 gives good results, even when the main beam is pointing slightly away from North Pole.
- For an antenna pointing at the North Pole, the performance between one acquisition rule and another is marginal for the absolute directivity decision function.
- When the side lobe level decision function is used the position of the side lobe region on the measurement sphere, and when in the iteration cycle acquisition traverses the side lobe region (on the NF sphere), has an influence. In future work it might be interesting to try to isolate the acquisition of the side lobe independently of the main beam. Then, if the side lobe level is the criterion of interest and its position on the NF sphere is known, one could acquire this sector to exhibit fast convergence for this decision function.
- With the non-North Pole pointing antenna, the selection of acquisition rule seems to be more critical for directivity measurement.

These points having been made, it is possible to say that while the improvement is not significant, acquisition rule #2 seems the best suited acquisition rule for a wide variety of AUT. This acquisition rule provides fair results for antennas which are pointing towards the North Pole or slightly shifted away from it.

Note that the shift away from the North Pole must not be too great for acquisition rule #2 to operate. Recall that this acquisition rule's first iteration starts at North Pole and scans in θ until a threshold is reached. If the main beam is shifted far away from the North Pole and the field amplitude at the pole is below the threshold, the initial iteration for acquisition rule #2 will only acquire the sample at the pole. Subsequent iterations will acquire bands of samples, and thus the acquisition rule #2 will behave just like acquisition rule #1. It is a good thing to have an acquisition rule that will work irrespective of the starting conditions. Now one could ask why not simply increase the threshold to a greater value in this case? If the threshold is too high, a very large portion of the measurement sphere will be acquired during the first iteration, thus making the adaptive algorithm irrelevant since already most of the measurement sphere will be sampled.

Part of the difficulty with acquisition rule #2 is the selection of the threshold value for the initial iteration. Without having additional knowledge about the AUT, it is difficult to choose an appropriate threshold. If the threshold is too low, no 'privileged' direction will be selected and hence, as stated, acquisition rule #2 will behave just like acquisition rule #1. For that reason when little is known about the AUT, one should use acquisition rule #1.

An AUT with low gain pointing at the North Pole won't benefit by being acquired with acquisition rule #2. Acquisition rule #1 will suffice since low gain pattern does not present a 'privileged' direction in space. In the event that a low gain antenna is pointing away from North Pole but a good portion of energy is still radiated through the pole, it might be beneficial to use acquisition rule #2. While the first iteration might already acquire all the necessary points for satisfying the selected accuracy, only a small number of unnecessary samples will be acquired.

An AUT with high gain pointing at the North Pole should benefit from being acquired with acquisition rule #2. Since high gain is synonymous with fast variation in space, the NF pattern of the AUT can have various shapes; which can benefit from being acquired using a shaped acquisition map. In the case of a high gain antenna pointing far away from the pole acquisition rule #2 won't work as it should. It might again behave just like acquisition rule #1. In this case, one should use the information of the location of the main beam found by the NF pre-conditioning as a starting point for a new acquisition rule to take care of that case.

6.4 - Decision Function Study

We now comment on the four decision functions chosen and their quality for automated decision taking. The principal quality sought is the ability to take unambiguous decision for a selected accuracy.

Absolute directivity seems like a good parameter to observe. In many cases the slope of this decision function is either positive or negative; it does not oscillate towards the final value, which simplifies the decision taking. One could combine the absolute directivity decision with the delta directivity. That way it is possible to look for a slope direction change in directivity, and the value of the slope. This was not implemented as a decision function in this work, but it might be of interest for future work.

Delta directivity alone is a poor parameter to monitor. In general it's highly unstable and oscillatory, as it's the derivative of the directivity, and therefore very difficult to use for automated decision taking. For this reason, in Section 6.3, this parameter was left unused since it would give less meaningful results. Although the delta directivity is hardly usable for automated algorithm, it can give useful information to an intelligent operator if it's provided during the acquisition in conjunction with the other decision functions.

Maximum pattern error is interesting for automated decision taking even though the value can be slightly oscillatory during the acquisition. By selecting an appropriate threshold, say -30 dB, -40 dB or even -60 dB, one can ensure that the overall FF pattern doesn`t change more than the selected value. Currently the maximum pattern error is implemented for the complete 3D FF. If only a sector of interest is required, one can only look at the pattern error over that sector.

While for side lobe level it's hard to tell which acquisition rule is best suited to converge the fastest, this decision function criterion seems well suited for automated decision taking. In general the slope is either positive or negative. We have noted that the convergence is a function of the position in space of the side lobe. Therefore one should be knowledgeable of how far the side lobe is from the North Pole before using this decision function.

6.5 - Realisation of a Practical Adaptive SNF System

6.5.1 - Summary of Findings on Pre-Conditioning, Acquisition Rules and Decision Function

Out of the three acquisition rule proposed, it was found that in absence of additional information about the AUT, one should rely on the increasing polar cap (acquisition rule #1) to perform adaptive acquisition. This rule complies with all the guidelines presented in Chapter 4. Also, if the decision function never tells the adaptive algorithm to halt the acquisition, this acquisition rule will acquire the complete measurement sphere; which is equivalent to the current adopted practice. This later fact can be seen as a reassuring point by SNF practitioners.

Some decision functions based on FF parameters of the AUT were studied as a mean to automatically tell the adaptive process that the acquisition should halt. It was found the directivity and the maximum pattern error seems to be good indicators of the completion of the process, while the directivity change and the side lobe level being weaker indicators.

The spherical interpolation of tangential field to the measurement sphere using orthogonal cuts is a topic of interest to get better approximation of the NF array for pre-conditioning. Three methods were implemented using linear interpolation of spherical components, using linear interpolation of Cartesian components, and using spherical wave expansion. It was found that the SWE method was a poor approach and that linear interpolation using spherical components is the best for NF pre-conditioning.

6.5.2 - Physical Implementation

In order to deliver the concepts presented in this work to the users, an implementation was developed for the DFL[15] facilities. A user interface to enable the selection of acquisition rules, the

[15] David Florida Laboratory, part of Canadian Space Agency, Ottawa, Canada

decision functions used and the use, or not, of NF pre-conditioning was created. The finding of Section 6.5.1 are ported to this implementation. The input interface, which can be seen in Figure 48, has a sequential flow. Instead of starting the acquisition with NSI2000, the implementation shows a form asking for inputs in the following way:

1- Prior to starting the adaptive acquisition application, set NSI2000 parameters for the acquisition (e.g. setting the frequencies, the probe distance to the AUT, steps in θ and ϕ, etc.).
2- Determine which acquisition rule to use. Only acquisition rule #1 is integrated currently; as no other studied acquisition rule were found to be useful, as described in Section 6.3.4.
3- Choose to go with manual or automated decision functions. If the manual option is selected, the user must halt the acquisition when he thinks enough information has been obtained. If the automated option is preferred, then the script checks at each iteration to see if the criteria are met, and if so stops the acquisition.
4- The decision function criteria are to be chosen by the user. The parameters of each decision function can be set by the user:
    a. The maximal directivity within a certain value for *n* iteration(s).
    b. The change in directivity being lower than a certain value for *n* iteration(s).
    c. The maximum pattern error being lower than a certain value for *n* iteration(s).
5- The NF pre-conditioning can be selected at will by the user. As already discussed the pre-conditioning takes more time to acquire the required cuts, but might settle some parameters faster. The interpolation function used is the linear interpolation method #1 for reasons presented in Section 6.2.
6- The user launches the adaptive acquisition, and if the form is properly filled the adaptive acquisition starts.

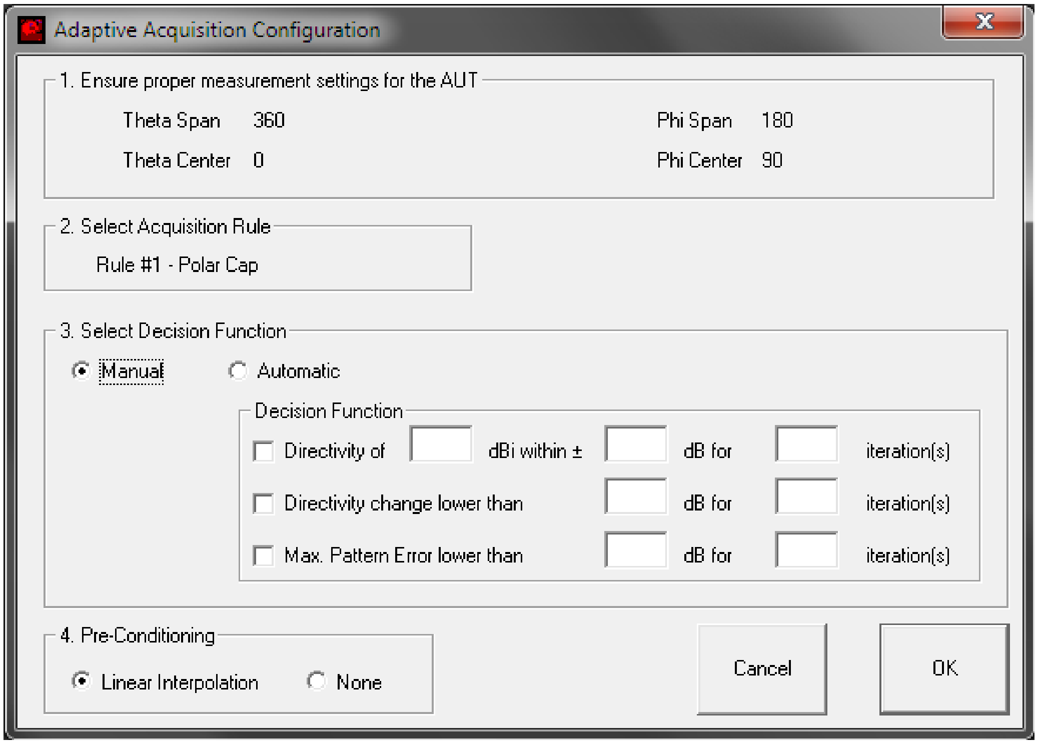

FIGURE 48 - NSI2000 INPUT INTERFACE FOR ADAPTIVE ACQUISITION CONFIGURATION

If the user has selected pre-conditioning, the set-up then starts acquiring the two orthogonal cuts that are necessary to perform interpolation. The acquisition then acquires datapoints in accordance with acquisition rule #1. Between each rings acquired, the FF is computed and the parameters of interests are devised; thus each new ring is defined as an iteration. Portraits of the fields and the derived parameters are presented to the user *via* a Matlab interface and *via* the usual NSI2000 plots. The Matlab output display is presented in Figure 49. This window presents the normalised NF θ- and ϕ-polarization plots, the normalised co-polarized FF as well as the directivity and the maximum pattern error evolution.

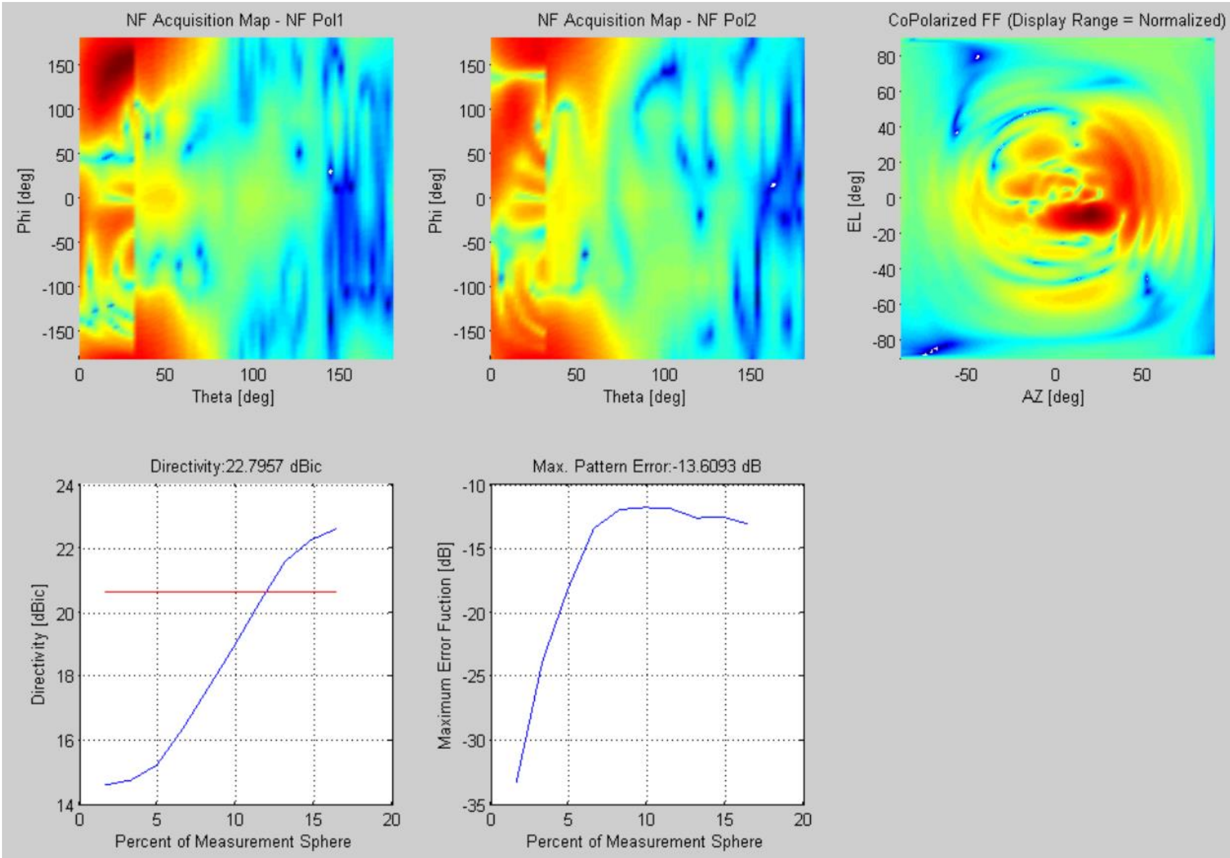

FIGURE 49 - MATLAB DISPLAY INTERFACE ON AN ADAPTIVE ON-GOING ACQUISITION

Then, if the automated mode is selected, at each iteration the chosen decision function(s), is (are) computed. If a parameter is satisfied, then the acquisition is halted and the user is notified with the final directivity, the last directivity change between iteration and the last maximal pattern error value.

It is also possible for the user to replay the acquisition evolution on the Matlab interface as at each iteration the arrays (NF θ-polarisation, NF ϕ-polarisation and the co-polarised FF) are saved.

6.6 - Concluding Remarks

In this chapter we presented the simulation study done on the fundamentals concepts of adaptive acquisition algorithm. The pre-conditioning study suggests that this technique is useful for the adaptive work, as it helps FF parameters such as the directivity to converge faster towards the final value. It was then found that in most cases the acquisition rule #1 – Increasing cap, is the best suited for the acquisition of an AUT without having *a priori* knowledge about its patterns. The study of the decision functions shed some light on the best parameters to monitor during an acquisition. The directivity of the main beam and the maximum pattern error are both good indicators of the progress of the acquisition. On the other hand, the delta directivity and the side lobe directivity are both weaker indicators. From these results, a practical interface for NSI2000 implementation of the adaptive acquisition concepts was created.

Chapter 7 - General Conclusions

7.1 - Contributions to SNF Antenna Measurements

This work presents the study done on the simulation and implementation of adaptive spherical near-field antenna measurement techniques in partnership with the David Florida Laboratory[16]. The usage of adaptive technique permits a test time reduction by acquiring only the right number of sample points to compute the parameters of an antenna with the desired accuracy. The processing power of modern computers enables the NF-to-FF computation to be done repeatedly; the premise of this work is based on that fact. The general concept of adaptive algorithm is defined, implemented in simulation using a software interface written between NSI2000 and Matlab, and deployed as a user interface for physical testing.

One contribution this work brings to the near-field antenna measurements domain is the ability to monitor the evolution of some NF and FF parameters while the acquisition is on-going. Traditionally the test engineer is "blind" until the probe has scanned the complete measurement sphere, which can take hours in certain cases. The ability to observe the fields as the measurements are occurring provides the operator with a good indication on how the test is progressing. This fact can certainly help for quick diagnosis and problem finding in SNF chambers, and might alone warrant implementation of portions of the software developed. An interesting aspect of this work is the ability to integrate the presented concepts without significantly modifying existing systems. No hardware change is necessary and the software suite is developed using NSI2000 and Matlab, which are wildly available in the SNF antenna test community.

Even though only the acquisition rule #1 was eventually physically implemented, as it was found to be the only one well-suited for any type of AUT, this work brings a new aspect to near-field measurement. The adaptive algorithm with this acquisition rule is worthwhile for SNF measurements as it was shown to allow one to reduce the percentage of the measurement sphere (with confidence) that has to be acquired. This indeed, reduces the acquisition time required to conduct the antenna testing, which was the goal. Not only can the operator see the evolution of the results as acquisition is happening, but also decide when the acquisition should stop. The decision

[16] Spacecraft assembly, integration and testing centre operated by the Canadian Space Agency in Ottawa, Canada

functions allow the operator to monitor some parameters of interests and halt the acquisition as they settle. Therefore the acquisition happens in a more controlled manner using the presented adaptive acquisition algorithm.

To further reduce the testing time, in certain cases, it might be worthwhile to use a more advanced acquisition rule such as acquisition rule #2. As shown, this rule requires certain knowledge about the AUT prior to use it. Hence, a test engineer might need to scan the complete measurement sphere before using this acquisition rule, and properly set the initial threshold. This can serve well in a production environment where multiple comparable antennas are manufactured.

7.2 - Future work

We now realise that a third acquisition rule (say rule #3), might be desirable. Rule #3 would perform acquisition along the curvilinear constant angle lines on the sphere, and would be similar to that used for adaptive PNF methods [Rens 12]. A representation of this acquisition rule is drawn in Figure 50. However, it will be such that it will not be possible to use it with North-Pole pointing NF data, and in fact will only work reliably if the NF data in fact points away from the North-pole by a significant amount. It was this fact that initially discouraged us from proposing an acquisition rule such as #3, until we realised that one simply needs to have different rules for different AUT pointing situations. This rule also presents some difficulty in the implementation. This is due to the fact that as the algorithm tells the probe to move closer to the pole, the “almost-square” grid present near the equator changes to an “almost-triangular” grid near the poles. Thus from an algorithm point of view this renders the acquisition rule difficult to implement while following the basic guide-lines presented in Section 4.4. Also, if the probe is asked to go over the pole by the acquisition rule, a geometrical ambiguity is present and further complicates the implementation. Some lessons may be learned from robotics as they often have to deal with such ambiguity to control the position of an arm.

Some more advance acquisition rule and decision function could certainly be the basis of some extended work. The combination of two decision functions might lead to more definite improvements in the percentage of the NF sphere that needs to be acquired. If a dynamic threshold value were to be used, it might be possible to get a shaped path acquisition rule such as rule #2 to not reduce to pre-defined rules such as rule #1 in certain cases.

An irregular spherical grid where points are separated by a near-equal distance (geodesic grid) could allow the creation of a much simpler acquisition rules as no pole singularity would be present. However, this would not be able to make use of the SWE technique for NF-to-FF transformation.

It might also be interesting to test and compare the effect of pre-conditioning using both longitudinal and equatorial cuts, with three cuts being acquired. This might lead to better pre-conditioned NF arrays, which in turn can lead to reduced test time. However, the interpolation of vector quantities over a spherical surface using the existing longitudinal cut data along with data from the equatorial cut would not be a simple process.

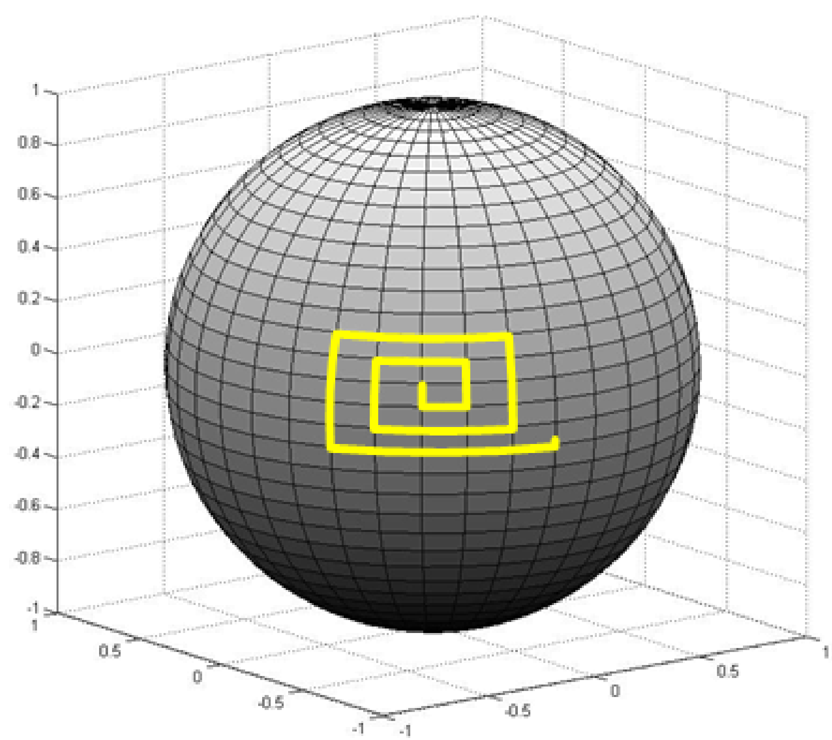

FIGURE 50 - SKETCH REPRESENTATION OF ACQUISITION RULE #3

References

[Alva 06] Y. Álvarez, F. Las-Heras & M.R. Pino, "Integral equation algorithms for equivalent currents distribution retrieval over arbitrary three-dimensional surfaces", in Proc. 1st European Conf. on Antenna and Propag . (EuCap), Nov. 2006

[Alva 07a] Y. Álvarez, F. Las-Heras, M.R. Pino & M.H. Alvarez, "Sources reconstruction techniques for the diagnosis and characterization of antennas of complex geometry," Proc. 3rd International Conf. on Near-field Imaging and Characterization (ICONIC), Jun. 2007, pp. 182-187

[Alva 07b] Y. Álvarez, F. Las-Heras & M.R. Pino, "Reconstruction of equivalent currents distribution over arbitrary three-dimensional surfaces based on integral equation algorithms", Trans. on Antennas Propag., vol. 55, no. 12, Dec. 2007, pp. 3460-3468

[Alva 08] Y. Alvarez, F. Las-Heras & M.R. Pino, "On the Comparison Between the Spherical Wave Expansion and the Sources Reconstruction Method," Trans. on Antennas Propag., vol. 56, no. 10, Oct. 2008, pp. 3337-3341

[Appe 86] J. Appel-Hansen, J.D. Dyson, E.S. Gillespie & T.G. Hickman, “Antenna Measurements”, Chapter 8 in A.W. Rudge, K. Milne, A.D. Olver & P. Knight (Eds.), *The Handbook of Antenna Design*, Peter Peregrinus Ltd, 1986

[Bala 05] C.A. Balanis, *Antenna Theory : Analysis and Design*, Wiley, 2005

[Bala 12] C. A. Balanis, *Advanced Engineering Electromagnetics*, Second Ed., Wiley, 2012

[Beau 12] V. Beaulé, D.A. McNamara, D.J.V. Rensburg, L. Shafai & S. Mishra, “Exploration of the Feasibility of Adaptive Spherical Near-field Antenna Measurements”, in Proc. Antenna Measurement Techniques Association Conf. (ATMA), Seattle (WA), USA, Oct. 2012

[Beau 13] V. Beaulé, D.A. McNamara, D.J.V. Rensburg & L. Shafai, “Exploration of the Feasibility of Adaptive Spherical Near-Field Antenna Measurements – Part II”, in Proc. Antenna Measurement Techniques Association Conf. (ATMA), Columbus (OH), USA, Oct. 2013

[Belo 62] S.L. Belousov, *Tables of Normalized Associated Legendre Polynomials*, Pergamon Press, Oxford, 1962

[Betj 12] P. Betjes, Applications Engineer, NSI, Private Communication, Nov. 2012

[Blad 07] J. van Bladel, *Electromagnetic Fields,* 2nd ed., IEEE Press/Wiley, 2007

[Bouw 54] C.J. Bouwkamp & H.B. Casimir, “On Multipole Expansion in the Theory of Electromagnetic Radiation”, Physica, Vol. 20, 1954, pp. 539-554

[Bucc 06] O. M. Bucci & M. D. Migliore, "A New Method for Avoiding the Truncation Error in Near-field Antennas Measurements," Trans. on Antennas Propag., vol. 54, no. 10, Oct. 2006, pp. 2940-2952

[Cano 11] F. J. Cano-Facila & S. Pivnenko, "A New Method to Reduce Truncation Errors in Partial Spherical Near-field Measurements," in Proc. 5th European Conf. on Antenna and Propag. (EuCap), Rome, Italy, 2011, pp. 3259-3263

[Cost 11] S. Costanzo & G. Di Massa, "Advanced Numerical Techniques for Near-Field Antenna Measurements," Chapter 15 in *Numerical Simulations of Physical and Engineering Processes*, J. Awrejcewicz (Eds.) InTech, 2011, pp. 321-338

[Dire 12] R.H. Direen & H.G. Direen, “Spherical Near-field Measurments: Going Off Grid”, in Proc. Antenna Measurement Techniques Association Conf . (ATMA), Seattle, USA, 2012

[Edmo 74] A.R. Edmonds, *Angular Momentum in Quantum Mechanics*, 2nd ed., Princeton University Press, Princeton New Jersey, 1974

[Gonz 09] R.C. Gonzalez, R.E. Woods & S.L. Eddins, *Digital Image Processing Using MATLAB*, Gatesmark Publishing, 2009

[Guler 95] M. G. Guler & E. B. Joy, "High resolution spherical microwave holography", IEEE Trans. Trans. on Antennas Propag., Vol. 43, May 1995, pp. 464 -472

[Hans 88] J. E. Hansen, *Spherical Near-field Antenna Measurements*, Peter Peregrinus Ltd, 1988

[Hess 82] D.W. Hess & J.J. Tavormina, “An Algorithm with Enhanced Efficiency for Computing the Far-field from Near-field data on a Partial Spherical Surface”, URSI, University of Colorado, Jan. 1982, pp.185

[Hind 06] G. Hindman & A. Newell, “Simplified Spherical Near-Field Accuracy Assessment”, in Proc. Antenna Measurement Techniques Association Conf. (ATMA), Cambridge (MA), USA, 2006

[Jame 69] J.R. James & L.W. Longdon, “Prediction of Arbitrary Electromagnetic Fields from Measured Data”, Alta Frequenza, Vol. 38, May 1969, pp. 286-290

[Jens 70] F. Jensen, “Electromagnetic Near-field – Far-field Correlations”, Ph.D. Thesis, Laboratory of Electromagnetic Theory, Technical University of Denmark, July 1970

[Jens 75] F. Jensen, “On the Probe Compensation for Near-field Measurement on a Sphere”, Archiv für Elektronik und Übertragungstechnik”, vol.29, No.7/8, July 1975, pp. 305-308

[Jens 04] F. Jensen & A. Frandsen, "On the Number of Modes in Spherical Wave Expansions," TICRA (www.ticra.com), Danmark, Technical Papers 2004

[Jone 64] D.S. Jones, *The Theory of Electromagnetism*, Section 8.16, MacMillan, New York, 1964

[Kern 60] D.M. Kerns & E.S. Dayhoff, “Theory of Diffraction in Microwave Interferometry”, J. Res. Natl. Bur. Stand. 64B, 1960, pp. 1-13

[Lars 80] F.H. Larsen, “Probe-Corrected Spherical Near-field Antenna Measurements”, Ph.D Thesis, Electromagnetics Institute, Technical University of Denmark, Dec. 1980

[Las 97] F. Las-Heras, B. Galocha & J.L. Besada, "Equivalent source modeling and reconstruction for antenna measurement and synthesis", IEEE AP-S Int. Symp. Digest, vol. 1, 1997, pp. 156-159

[Las 99a] F. Las-Heras, "Sequential reconstruction of equivalent currents from spherical acquisition", IEEE Electronics Letters, vol. 35, no. 3, Feb. 1999, pp. 211-212

[Las 99b] F. Las-Heras & B. Galocha, "Planar source reconstruction and far field calculation from near field hemispherical acquisition", in Proc. Antenna Measurement Techniques Association Conf. (ATMA), Montery Bay (CA), USA, 1999

[Las 06] F. Las-Heras, M.R. Pino, S. Loredo, Y. Alvarez & T.K. Sarkar, "Evaluating near-field radiation patterns of commercial antennas", Trans. on Antennas and Propag., vol. 54, no. 8, Aug. 2006, pp. 2198-2207

[Ludw 69] A.C. Ludwig, “Calculation of Scattered Patterns from Asymmetrical Reflectors”, Ph.D. Dissertation, University of Southern California, Los Angeles (CA), 1969

[Ludw 71] A.C. Ludwig, "Near-Field Far-Field Transformation Using Spherical-Wave Expansions," Trans. on Antennas and Propag, vol. 19, no. 2, Mar. 1971, pp. 214 - 220

[Lope 08] Y. A. Lopez, C. Cappellin, F. Las-Heras & O. Breinbjerg, "On the Comparison of the Spherical Wave Expansion-To-Plane Wave Expansion and the Sources Reconstruction Method for Antenna Diagnostics," Progress In Electromagnetics Research (PIER), vol. PIER-87, 2008, pp. 245-262

[Mart 11] E. Martini, S. Maci & L.J. Foged, "Spherical near field measurements with truncated scan area", in Proc. 5th European Conf. on Antenna and Propag. (EuCAP 2011), Rome, Italy, Apr. 2011

[Matw 13a] Mathworks Documentation Center, Image Processing Toolbox, Image Enhancement, Morphological Filtering, STREL, http://www.mathworks.com/help/images/ref/imdilate.html, Mar. 2013

[Matw 13b] Mathworks Documentation Center, Image Processing Toolbox, Image Enhancement, Morphological Filtering, IMDILATE, http://www.mathworks.com/help/images/ref/strel.html, Mar. 2013

[NSI 06] Near-Field Systems Inc. (2006). Near-Field 101. (www.nearfield.com)

[Paris 78] D. Paris, W. Leach & E.B. Joy, “Basic theory of probe-compensated near-field measurements”, Trans. on Antennas and Propag., vol. 26, no. 3, 1978

[Petre 91] P.Petre, T.K.Sarkar, S.Ponnapalli & B.Szekeres, "Integral equation solution for near-field to far-field transformation”, Proc. Int. Conf. Computation in Electromagnetics, Nov. 1991, pp. 218-221

[Ponn 91a] S.Ponnapalli, "Near-field to far-field transformation utilizing the conjugate gradient method", Progress in Electromagnetics Research (PIER), vol. 5, 1991, pp. 391-422

[Ponn 91b] S.Ponnapalli, T.K.Sarkar & P.Petre, "Near-field to far-field transformation using an equivalent current approach”, IEEE Int. AP-S Symp. Digest, 1991, pp. 1458-1461

[Pott 67] P. D. Potter, "Application of Spherical Wave Theory to Cassegrainian-Fed Paraboloids," Trans. on Antennas and Propag., vol. 15, no. 6, Nov. 1967, pp. 727 - 736

[Pott 74] P. D. Potter & A. C. Ludwig, "Applications of Spherical Wave Expansions to Near-Field Problems", IEEE Int. AP-S Symp. Digest, June 1974, pp. 158-160

[Qure 12] M. A. Qureshi, C. H. Schmidt & T. F. Eibert, "Adaptive Sampling Spherical and Cylindrical Near-Field Antenna Measurements", in Proc. Antenna Measurement Techniques Association Conf. (ATMA), Seattle (WA), USA, Oct. 2012

[Rens 11] D.J.V. Rensburg, D. McNamara & G. Parsons, "Adaptive Acquisition Technique for Planar Near-field Antenna," in Proc. Antenna Measurement Techniques Association Conf. (ATMA), Englewood (CO), USA, 2011

[Rens 12] D.J.V. Rensburg & D.A. McNamara, “Adaptive Acquisition Techniques for Planar Near-field Antenna Measurements - Part 2”, in Proc. Antenna Measurement Techniques Association Conf. (ATMA), Seattle (WA), USA, Oct. 2012

[Rica 72] L.J. Ricardi & M.L. Burrows, “A Recurrence Technique for Expanding a Function in Spherical Harmonics”, Trans. on Computers, Vol 21, No.6, June 1972, pp.583-585

[Rudg 86] A.W. Rudge, K. Milne, A.D. Olver & P. Knight, *The Handbook of Antenna Design*, Second Ed., Chapter 2-3, Peter Peregrinus Ltd, 1986

[Sark 99] T.K. Sarkar & A. Taaghol, “Near-field to Near/Far-Filed Transformation for Arbitrary Near-Field Geometry Utilizing an Equivalent Electric Current and MoM”, Trans. on Antennas and Propag., vol. 47, Mar. 1999, pp.566-573

[Schm 08] C.H. Schmidt, M.M. Leibfritz & T.F. Eibert, “Fully probe-corrected near-field far-field transformation employing plane wave expansion and diagonal translation operators”, Trans. on Antennas and Propag., vol. 56, Mar. 2008, pp.737-746

[Schm 09], C.H. Schmidt, & T.F. Eibert, “Multilevel Plane Wave Based Near-Field Far-Field Transformation for Electrically Large Antennas”, Antennas and Propag. Magazine, Vol. 57, No. 5, May 2009, pp.1382 - 1390

[Schm 10] C.H. Schmidt, T.A. Laitinen & T.F. Eibert, “Fast Fourier transform preprocessing for accelerated plane wave based spherical near-field far-field transformation”, Proc. URSI Electromagnetic Theory Symposium, 2010, pp.784-787

[Schm 11a] C.H. Schmidt & T.F. Eibert, "Assessment of irregular sampling near-field far-field transformation employing plane-wave field representation", Antennas and Propag. Magazine, Vol.53, No.3, June 2011, pp.213 - 219

[Schm 11b] C.H. Schmidt, T.F. Eibert & T.A. Laitinen, "Hybrid fast Fourier transform - Plane wave based near-field far-field transformation for 'body of revolution' antenna measurement grids : The cylindrical case", IEEE Int. AP-S Symp. Digest, USA, July 2011, pp.1628-1631

[Star 98] H. Stark & Y. Yang, *Vector Space Projections: A Numerical Approach to Signal and Image Processing, Neural Nets, and Optics*, Wiley, 1998

[Stra 41] J. A. Stratton, *Electromagnetic Theory*, Chapter VII, McGraw-Hill Inc., New York, 1941

[Stut 97] W.L. Stutzman & G.A. Thiele, *Antenna Theory and Design*, Wiley, 1997

[Taag 96] A. Taaghol & T.K. Sarkar, "Near-field to near/far-field transformation for arbitrary near-field geometry utilizing an equivalent magnetic current", Trans. on Electromagnetic Compatibility, vol. 38, no. 3, Aug. 1996, pp. 536-542

[Ticr] SNIFTD : Software Package for Spherical Near-Field Far-Field Transformations with Full Probe Correction, TICRA Engineering Consultants, Denmark(www.ticra.com)

[Vola 07] J.L. Volakis, *Antenna Engineering Handbook*, McGraw-Hill Inc., New York, 2007

[Wack 74] P.F. Wacker, "Near-field Antenna Measurements Using a Spherical Scan: Efficient Data Reduction With Probe Correction", Conference on Precision Electromagnetic Measurements, IEEE Conference Publication No.113, London, England, 1974, pp.286-288

[Wack 75] P.F. Wacker, "Non-Planar Near-field Measurements: Spherical Scanning", Report NBSIR75-809, NIST, Electromagnetics Division, Boulder (CO), USA, June 1975

[Witt 84] R.C. Wittmann, "Probe Correction in Spherical Near-field Scanning, Viewed as an Ideal Probe Measuring an Effective Field", IEEE Int. AP-S Symp. Digest, Vol. 2, Boston (MA), USA, 1984, pp.674-677

[Witt 02] R.C. Wittmann, C.F. Stubenrauch & C.F. Francis, "Spherical-Scanning Measurements Using Truncated Data Sets", in Proc. Antenna Measurement Techniques Association Conference (ATMA), Tiburon (CA), USA, 2002

[Wood 80] P.J. Wood, *Reflector Antenna Analysis and Design*, Peter Peregrinus Ltd, 1980

[Yagh 84] A.D. Yaghjian, “Simplified Approach to Probe-Corrected Spherical Near-Field Scanning”, Electronics Letters, Vol.20, No.5, Mar. 1984, pp.195-196

[Yagh 85] A.D. Yaghjian & R.C. Wittmann, “The Receiving Antenna as a Linear Differential Operator: Application to Spherical Near-field Scanning”, Trans. on Antennas and Propag., Vol. 33, No. 11, Nov. 1985, pp.1175-1185

[Yagh 86] A.D. Yaghjian, “An overview of near-field antenna measurements”, Trans. on Antennas and Propag. , vol. 34, no. 1, Jan. 1986, pp. 30-45

[Yang 11] T. Yang & W.A. Davis, "A direct matrix approach to 3-D antenna radiation-pattern estimation from partially-scanned spherical near-field data", 2011 URSI General Assembly and Scientific Symp., Istanbul, Turkey, Aug. 2011

Appendix A – Spherical Wave Expansion (SWE) Fundamentals

To represent fields at a point in space, one can decompose the total field into a summation of spherical waves [Stra 41]. Analogous to Fourier series techniques, the spherical wave expansion relies on a complex weighted summation of an orthogonal basis; the vector spherical wave functions. The basis function is a spherical wave front with a sinusoidal variation in θ and in ϕ related to the order (harmonic) of the wave. The higher the order of the spherical wave, the more rapidly the amplitude will change with a variation in θ and in ϕ; the vector spherical wave function can be viewed as a spatial frequency. Let`s now build the formulations and the relations needed to represent the spherical wave expansion up to the topic of interest, SNF measurement. Note that the temporal dependence $e^{-j\omega t}$ is implied in this work. With this choice of temporal dependence, the type c=3 radial functions (spherical Hankel function of 1st kind) will belong to outward propagating mode satisfying the radiation condition at infinity. Some authors prefer to use $e^{j\omega t}$, therefore in this case the type c=4 radial functions will be outward propagating.

Maxwell's equations for the fields in a medium that is linear, isotropic and homogeneous can be written as

$$\nabla x \vec{H} = -j\omega\varepsilon\vec{E} + \vec{J} \tag{a.1}$$

and

$$\nabla x \vec{E} = j\omega\mu\vec{H} - \vec{M} \tag{a.2}$$

where, μ is the permeability of the medium

ε is the permittivity of the medium

In a source-free region, Maxwell's equations imply that both $\vec{E}$ and $\vec{H}$ satisfy the vector wave equation

$$\nabla\, x\, \left(\nabla\, x\, \vec{C}\right) - k^2\vec{C} = 0 \tag{a.3}$$

where, k is the wave number defined as $k = \frac{2\pi}{\lambda}$

Being defined in spherical coordinates, a generating function can be obtained by solving the scalar wave equation

$$(\nabla^2 + k^2)f = 0 \tag{a.4}$$

From that generating function f, two vector functions $\overrightarrow{m}$ and $\overrightarrow{n}$ can be defined as

$$\overrightarrow{m} = \nabla f \; x \; \vec{\rho} \tag{a.5}$$

and

$$\vec{n} = k^{-1}\nabla \; x \; \overrightarrow{m} \tag{a.6}$$

with $\overrightarrow{\rho} = \rho\hat{\rho}$, as presented in geometry of Figure 4.

The vector wave functions $\overrightarrow{m}$ and $\overrightarrow{n}$ are well suited to represent electromagnetic field $\vec{E}$ and $\vec{H}$ since they are related by curl operator. [Bouw 54] showed that in a source-free region enclosed between two fictitious concentric spheres, only TE and TM waves to $\hat{\rho}$ can exist and therefore eq.a.5 and eq.a.6 constitute a complete solution for possible fields.

[Stra 41] presents a generating function obtained from the separation of variables solution of (a.4)

$$f^{(i)}_{\begin{Bmatrix} e \\ o \end{Bmatrix}(m,n)}(\rho,\theta,\varphi) = z_n^{(i)}(k\rho)P_n^m(\cos\theta)\begin{Bmatrix} cos \\ sin \end{Bmatrix}(m\varphi) \tag{a.7}$$

By employing this generating function, one can derive the vector wave functions $\overrightarrow{m}$ and $\overrightarrow{n}$ as

$$\begin{aligned}\overrightarrow{m}^{(i)}_{\begin{Bmatrix} e \\ o \end{Bmatrix}(m,n)} &= \{\mp\}\frac{m}{\sin\theta}z_n^{(i)}(k\rho)P_n^m(\cos\theta)\begin{Bmatrix} sin \\ cos \end{Bmatrix}(m\varphi)\hat{\theta} \\ &-z_n^{(i)}(k\rho)\frac{\partial P_n^m(cos\,\theta)}{\partial\theta}\begin{Bmatrix} cos \\ sin \end{Bmatrix}(m\varphi)\hat{\varphi}\end{aligned} \tag{a.8}$$

and

$$\vec{n}^{(i)}_{\left\{\begin{smallmatrix} e \\ o \end{smallmatrix}\right\}(m,n)} = \frac{n(n+1)}{k\rho} z_n^{(i)}(k\rho) P_n^m(\cos\theta) \left\{\begin{matrix} cos \\ sin \end{matrix}\right\} (m\varphi)\hat{\rho}$$

$$+ \frac{1}{k\rho} \frac{\partial \rho z_n^{(i)}(k\rho)}{\partial \rho} \frac{\partial P_n^m(\cos\theta)}{\partial \theta} \left\{\begin{matrix} cos \\ sin \end{matrix}\right\} (m\varphi)\hat{\theta} \qquad \text{(a.9)}$$

$$\{\mp\} \frac{m}{k\rho \sin\theta} \frac{\partial \rho z_n^{(i)}(k\rho)}{\partial \rho} P_n^m(\cos\theta) \left\{\begin{matrix} sin \\ cos \end{matrix}\right\} (m\varphi)\hat{\varphi}$$

where,

$\left\{\begin{matrix} e \\ o \end{matrix}\right\}$ is the even or odd azimuthal (ϕ) dependence

n-index is an integer representing the polar (θ) wave number

m-index is an integer representing the azimuth (ϕ) wave number

k is the wave number

{ } is the "top or bottom" operator to choose according to whether there is an even (top) or odd (bottom) azimuthal (ϕ) dependence

$P_n^m(\cos\theta)$ is the Legendre function

(*i*)-index represents the type of spherical Bessel function governing the radial dependence. In such case, (*i*) takes a value from 1 to 4, where

$z_n^1(k\rho) = j_n(k\rho)$, spherical Bessel function. Represents standing waves.

$z_n^2(k\rho) = y_n(k\rho)$, spherical Neumann function. Represents standing waves.

$z_n^3(k\rho) = h_n^1(k\rho)$, spherical Hankel function of 1st kind. Sufficient for outgoing wave solution for finite source .

$z_n^4(k\rho) = h_n^2(k\rho)$, spherical Hankel function of 2nd kind. Sufficient for incoming wave solution for finite source.

It is then possible to expand the fields using spherical vector wave functions as Jone 64]

$$\vec{E}(\rho,\theta,\varphi) = -\sum_m \sum_n (a^{(i)}_{\left\{\substack{e\\o}\right\}(m,n)} \vec{m}^{(i)}_{\left\{\substack{e\\o}\right\}(m,n)} + b^{(i)}_{\left\{\substack{e\\o}\right\}(m,n)} \vec{n}^{(i)}_{\left\{\substack{e\\o}\right\}(m,n)}) \tag{a.10}$$

and

$$\vec{H}(\rho,\theta,\varphi) = -\frac{k}{j\omega\mu}\sum_m \sum_n (a^{(i)}_{\left\{\substack{e\\o}\right\}(m,n)} \vec{n}^{(i)}_{\left\{\substack{e\\o}\right\}(m,n)} + b^{(i)}_{\left\{\substack{e\\o}\right\}(m,n)} \vec{m}^{(i)}_{\left\{\substack{e\\o}\right\}(m,n)}) \tag{a.11}$$

where,

a is the complex coefficient of TE waves [V/m]

b is the complex coefficient of TM waves [V/m]

[Jens 70] presents a more concise notation, as well as power normalization, for spherical waves. In order to formulate $\overrightarrow{m}$ and $\overrightarrow{n}$ in this single notation, the operator $\vec{f}^{(c)}_{smn}$ is introduced. To be consistent with [Jens 70] notation, we use the *c*-index instead of the *i*-index to represent the Bessel function governing the radial dependence for the rest of this section. The convention is that s = 1 denotes $\overrightarrow{m}$, and s = 2 denotes $\overrightarrow{n}$. Also, for convenience, $e^{jm\varphi}$ replaces $\left\{\begin{matrix} cos \\ sin \end{matrix}\right\}(m\varphi)$. Thus, $\vec{f}^{(c)}_{1mn} = \vec{m}^{(c)}_{(m,n)}$, and $\vec{f}^{(c)}_{2mn} = \vec{n}^{(c)}_{(m,n)}$. To get a power-normalized form, we define that any spherical outgoing wave (c=3) with an amplitude of 1 radiating ½ [W].

This results in the power-normalized generating function being

$$F^{(c)}_{mn}(\rho,\theta,\varphi) = \frac{1}{\sqrt{2\pi}}\frac{1}{\sqrt{n(n+1)}}\left(-\frac{m}{|m|}\right)^m z^{(c)}_n(k\rho)\bar{P}^{|m|}_n(\cos\theta)e^{jm\varphi} \tag{a.12}$$

where, $\bar{P}^{|m|}_n(\cos\theta)$ is the normalized Legendre function presented by [Belo 62].

The factor $\frac{1}{\sqrt{2\pi}}\frac{1}{\sqrt{n(n+1)}}\left(-\frac{m}{|m|}\right)^m$ ensures power-normalized values as well as phase coherence of the spherical harmonics defined by [Edmo 74]. Also note that we define

$$\left(-\frac{m}{|m|}\right)^m = 1 \quad for\ m = 0 \tag{a.13}$$

With such power-normalized generating functions, the vector spherical wave functions, now denoted by $\vec{F}_{1mn}^{(c)}$ and $\vec{F}_{2mn}^{(c)}$ are

$$\vec{F}_{1mn}^{(c)}(\rho,\theta,\varphi) = \nabla F_{mn}^{(c)}(\rho,\theta,\varphi) x\vec{\rho}$$

$$= \frac{1}{\sqrt{2\pi}}\frac{1}{\sqrt{n(n+1)}}\left(-\frac{m}{|m|}\right)^m \left\{ z_n^{(c)}(k\rho)\frac{jm\bar{P}_n^{|m|}(\cos\theta)}{sin\theta} e^{jm\varphi}\hat{\theta} - z_n^{(c)}(k\rho)\frac{\partial\bar{P}_n^{|m|}(cos\,\theta)}{\partial\theta} e^{jm\varphi}\hat{\varphi} \right\} \tag{a.14}$$

and

$$\vec{F}_{2mn}^{(c)}(\rho,\theta,\varphi) = k^{-1}\nabla \mathrm{x} \vec{F}_{1mn}^{(c)}(\rho,\theta,\varphi)$$

$$= \frac{1}{\sqrt{2\pi}}\frac{1}{\sqrt{n(n+1)}}\left(-\frac{m}{|m|}\right)^m \left\{ \frac{n(n+1)}{k\rho} z_n^{(c)}(k\rho)\bar{P}_n^{|m|}(\cos\theta) e^{jm\varphi}\hat{\rho} + \frac{1}{k\rho}\frac{\partial k\rho z_n^{(c)}(k\rho)}{\partial k\rho}\frac{\partial\bar{P}_n^{|m|}(\cos\theta)}{\partial\theta} e^{jm\varphi}\hat{\theta} + \frac{1}{k\rho}\frac{\partial k\rho z_n^{(c)}(k\rho)}{\partial k\rho}\frac{jmP_n^m(\cos\theta)}{\sin\theta} e^{jm\varphi}\hat{\varphi} \right\} \tag{a.15}$$

These power-normalized spherical wave functions are dimensionless. We can write the compact expansion of the fields as

$$\bar{E}(\rho,\theta,\varphi) = \frac{k}{\sqrt{\eta}}\sum_{csmn} Q_{smn}^{(c)}\,\vec{F}_{smn}^{(c)}(\rho,\theta,\varphi) \tag{a.16}$$

$$\bar{H}(\rho,\theta,\varphi) = -jk\sqrt{\eta}\sum_{csmn} Q_{smn}^{(c)}\,\vec{F}_{(3-s)mn}^{(c)}(\rho,\theta,\varphi) \tag{a.17}$$

where $Q_{smn}^{(c)}$ is the power-normalized complex coefficient related to $a_{\left\{\substack{e\\o}\right\}(m,n)}^{(i)}$ and $b_{\left\{\substack{e\\o}\right\}(m,n)}^{(i)}$.

The relation of the complex coefficients Q to a and b is similar to the relation of $\vec{f}_{smn}^{(c)}$ to $\vec{m}_{(m,n)}^{(c)}$ and $\vec{n}_{(m,n)}^{(c)}$, that is $Q_{1mn}^{(c)} = a_{(m,n)}^{(c)}$ and $Q_{2mn}^{(c)} = b_{(m,n)}^{(c)}$. The wave function $\vec{F}_{smn}^{(c)}$ being dimensionless, the factor in front of the summations in (a.16) and (a.17) is required to obtain watts$^{1/2}$ unit from the wave coefficient $Q_{smn}^{(c)}$.

Note that in general the proper choice of c must ensure a complete and orthogonal representation of finite, continuous and single-value solutions to Maxwell's equations in source-free regions. For the problem under consideration (SNF measurements), the spherical waves must satisfy radiation condition at infinity, thus c = 3. This choice is sufficient to produce a unique solution.

It is good at this point to look at the summation notation

$$\sum_{csmn} = \sum_{c=3}^{4}\sum_{s=1}^{2}\sum_{n=1}^{\infty}\sum_{m=-n}^{n} \tag{a.18}$$

As we can see in (a.18), the number of modes required to represent the fields at a point is infinite. But it can be shown that only a finite numbers of modes will propagate, the rest will exponentially decay. The maximum value retained for the sum, for both m and n, are noted by the indices *M* and *N* respectively. The summation over s, m and n is often viewed as an (m, n) coordinate on two planes (one for s = 1 and one for s = 2). Also, we let the c-value be fixed to either c = 3 or c = 4 depending on the application. However at this point in (a.18), we let c to be summed from 3 to 4 to keep the generality of this formulation.

The spherical wave expansion idea can be given a physical meaning by visualizing the modes as taking place in a free-space spherical waveguide. Many properties of cylindrical waveguides find their counterparts in spherical waveguides. To gain a deeper understanding of this concept, the interested reader is refer to [Hans 88, pp.15-17]. Here, the analogy of interest from cylindrical waveguides is the cut-off phenomenon, also occurring for spherical waveguides. In a cylindrical waveguide, some modes may be above the cut-off and will propagate, while others are below the threshold and will decay exponentially - the evanescent modes. As the size of the waveguide increases, a larger number of modes can propagate. For the spherical waveguide the transition between propagation and evanescence for a mode occurs around a radial distance of $\rho_{trunc} = n/k$; as $\rho \gg \rho_{trunc}$ the mode will propagate. By inspection, we observe that $\bar{P}_n^{|m|}(\cos\theta)$ vanishes for $|m| > n$, therefore $M \leq N$. For an antenna circumscribed entirely by a minimum sphere of radius ρ_0, the radiated field must in theory be represented by an infinite numbers of modes as previously mentioned. However, modes with $n > k\rho_0$ will be heavily attenuated outside the minimum sphere. As mentioned in [Hans 88, pp.17]

> "This is a consequence of the cut-off property of the radial functions for the outwards propagating modes. The radial functions are very large (and dominantly imaginary) for [ρ] smaller than the cut-off distance n/k. For [ρ] larger than *n/k*, the amplitude of the radial functions behaves as [ρ^{-1}] to a good approximation."

Hence the key is that only modes satisfying $n < k\rho_0$ are of importance in the source-free region; the summation can then be truncated at n = N. As stated by [Ludw 71], 99.9% of the power is always contained in modes for which $n \leq k\rho_0$. This leads to the formulation of an empirical rule that links the number of meaningful modes to the physical size of the source,

$$N = k\rho_0 + n_1 \tag{a.19}$$

where, ρ_0 is the radius of the minimum sphere enclosing completely the sources, as defined in Figure 51. The factor n_1 is an integer based on the location in the coordinate system and the accuracy required [Hans 88, pp.17].

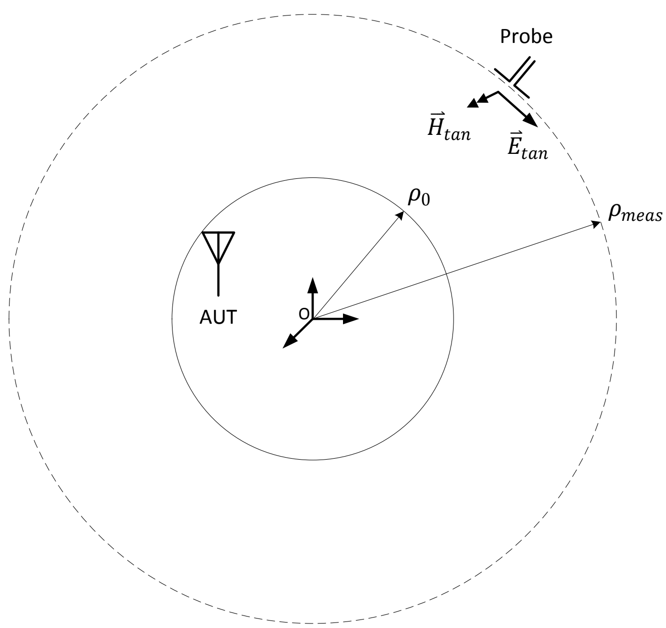

FIGURE 51 - GEOMETRY OF SNF MEASUREMENTS

A few important points must be made here:

- As the minimum sphere radius ρ_0 becomes smaller, the number of modes required to represent the total field diminishes. Therefore, if the AUT is electrically small only a small number of modes are required.
- If the AUT is not centered at the origin of the coordinate system, the minimum sphere is larger and thus more modes are required to represent the solution. As we will see shortly, by centering the antenna we ensure that a minimum number of modes is required.
- From this perspective, one can see why only electrically large antennas can be directive. Low-order modes have a slow spatial variation, while high-order modes have a faster variation in θ or ϕ. The gain being a large spatial variation of fields, the antenna must be electrically large to propagate high order modes that can abruptly change in space.

From the value of *N*, one can easily determine the total number of wave modes needed to represent an outgoing wave, namely

$$2N(N+2) \tag{a.20}$$

With mode coefficients and spherical wave functions power-normalized, it is possible find the power radiated using only the mode coefficients, as

$$P_{rad} = \frac{1}{2}\sum_{smn}\left|Q_{smn}^{(3)}\right|^2 \quad [\mathrm{W}] \tag{a.21}$$

which can be re-written as

$$P_{rad} = \frac{1}{2}\sum_{n=1}^{N} P_{rad}^{(n)} \tag{a.22}$$

where

$$P_{rad}^{(n)} = \frac{1}{2}\sum_{sm}\left|Q_{smn}^{(3)}\right|^2 \tag{a.23}$$

is the power spectrum. From these expressions, [Jens 04] came up with the idea of studying the relationship between the order of the mode and the power truncated during an acquisition. Since, a relation exists between the spatial sampling and the numbers of mode being represented[17], it is possible to sum the power truncated by using only a limited numbers of mode versus using an infinite numbers of mode. This leads to a better appreciation of the factor n_1 in (a.19), which was historically fix to 10 for computational reasons. Now this factor can be linked to an acceptable power truncation, which should be ideally lower than the noise floor of the measurement chamber.

More can be said about the properties of the modes, the orthogonally characteristics and also their transformations, but the essential for this work is presented. The interested reader is referred to [Hans 88, Appendix A1] [Bala 12, Section 3.4.3 and 10.4] and [Rudg 86] for further details.

At this point we will link SWE theory to practical SNF measurements. As previously mentioned, in the case of interest only the outgoing wave (c = 3) is used, and therefore for clarity will no longer be shown explicitly. To summarize up to now, the E-field at a point in source-free space can be represented as a weighted sum of spherical waves as

$$\vec{E}(\rho,\theta,\varphi) = \frac{k}{\sqrt{\eta}} \sum_{s=1}^{2} \sum_{n=1}^{N} \sum_{m=-n}^{n} Q_{smn} \vec{F}_{smn}(\rho,\theta,\varphi) \qquad \text{(a.24)}$$

where,

k is the wave number

η impedance of the medium

Q_{smn} is the modal coefficient

$\bar{F}_{smn}$ is the power-normalized spherical wave function

s has a value of 1 for TM fields and 2 for TE fields

m is limited by $|m| \leq n$

n is limited by the extent of the source to $1 \leq n \leq N$

[17] Refer to (a.40) and (a.41)

N is an integer that represents the number of modes propagating given the radius of the minimum sphere enclosing the source (the AUT in SNF measurements)

Now that we have a proper formulation for the expansion of the fields, we must solve the following problem:

A finite radiation source is present in space and completely contained within a minimum sphere of radius ρ_0. An electromagnetic field $\vec{E}(\rho,\theta,\varphi), \vec{H}(\rho,\theta,\varphi)$ exists in a region outside of this minimum sphere. Given only the tangential electrical field on a surface of radius $\rho_{meas} > \rho_0$, determine the expansion coefficients for (a.24).

To do so, we define a spherical surface where the measurement occurs, the measurement sphere; the surface on which the probe will travel and measure the tangential fields. This sphere has a radius ρ_{meas} as depicted in Figure 51. The radius of this sphere is larger than the minimum sphere, $\rho_{meas} > \rho_0$, encloses all sources, and is concentric to the minimum sphere ρ_0.

If only outgoing waves are needed, as in the case of SNF measurements, only $\vec{E}_{tan}$, the tangential component of the E-field, on the measurement surface is required to fully expand the fields into spherical components. If both incoming and outgoing waves are required, both $\vec{E}_{tan}$ and $\vec{H}_{tan}$ are necessary. To understand why only the tangential components are needed, we refer to the scheme proposed in [Ludw 69] and [Ludw 71]. The equivalence principle gives a very good insight of why this is so, refer to Section 3.3.1 for a short explanation.

We must now measure the fields in order to evaluate the coefficients Q_{smn}. To acquire the tangential field on the measurement surface, a linear-polarized probe measures a component of the field (θ or ϕ) on the complete sphere. Then the probe is rotated on his axis (noted by χ) by 90 degrees to measure the remaining component. Therefore two orthogonal components are acquired (θ, ϕ), which is sufficient to recover the tangential component of the field on the surface. The geometry of the probe is presented in Figure 52.

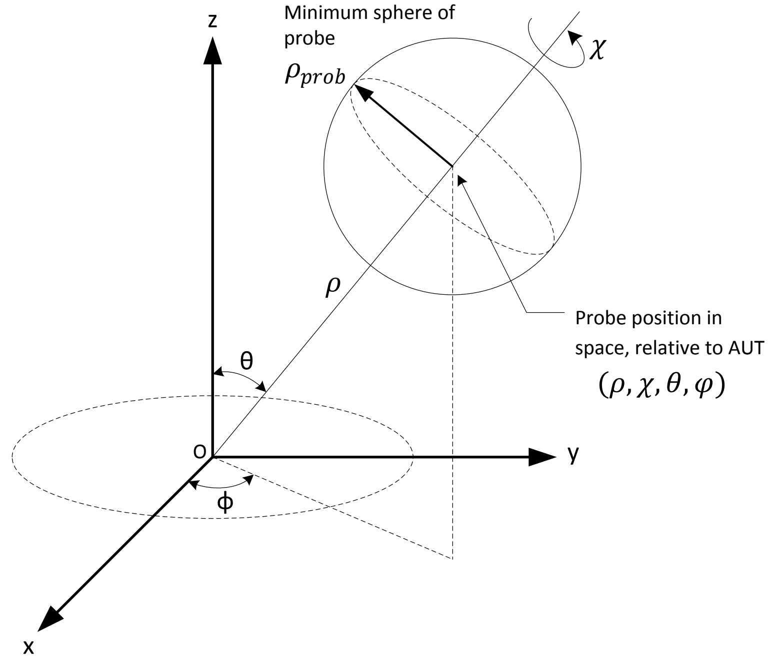

FIGURE 52 - PROBE GEOMETRY IN SPACE

Once $\vec{E}_{tan}$ has been measured over the sphere surrounding the AUT, the coefficients of the SWE must be computed. We will start, for explanation purpose, with an electric dipole as our probe; which is rarely the case for modern measurement. Based on expansion of the fields, one can devise the signal received due to the transmission coefficients of the AUT (which are unknown),

$$w_\theta^e(\rho_{meas}, \chi_\theta, \theta, \varphi) = \frac{\sqrt{6\pi}}{2} \upsilon \sum_{s=1}^{2} \sum_{n=1}^{N} \sum_{m=-n}^{n} T_{smn} \vec{F}_{smn}^{(3)}(\rho_{meas}, \theta, \varphi). \hat{\theta} \tag{a.25}$$

$$w_\varphi^e(\rho_{meas}, \chi_\varphi, \theta, \varphi) = \frac{\sqrt{6\pi}}{2} \upsilon \sum_{s=1}^{2} \sum_{n=1}^{N} \sum_{m=-n}^{n} T_{smn} \vec{F}_{smn}^{(3)}(\rho_{meas}, \theta, \varphi). \hat{\varphi} \tag{a.26}$$

where,

$w_{\{\theta,\varphi\}}^e(\rho, \chi_{\{\theta,\varphi\}}, \theta, \varphi)$ is the signal received by an electric dipole located at (ρ, θ, ϕ) in space and rotated on its axis by an amount χ.

χ_θ and χ_φ represent, respectively, the polarization in $\hat{\theta}$ or $\hat{\varphi}$ on the measurement sphere.

The factor $\frac{\sqrt{6\pi}}{2}$ comes from the form factor of the probe, in this case a dipole. The form factor being the ratio between the received potential in presence of an electric field.

υ is the excitation of the transmit antenna, the AUT, in [V]

T_{smn} are the transmission coefficients of the AUT, related to the notation used so far by

$$Q_{smn}^{(3)} = \upsilon T_{smn} \tag{a.27}$$

With these two equations, and some manipulations: multiplying by the vector wave function in both polarization and integrating over θ and ϕ, yields

$$\upsilon T_{smn} = \frac{2}{\sqrt{6\pi}} \frac{(-1)^m}{\left[R_{sn}^{(3)}(k\rho_{meas})\right]^2} \int_{\varphi=0}^{2\pi} \int_{\theta=0}^{\pi} \{w_\varphi^e \hat{\theta} + w_\varphi^e \hat{\varphi}\}.\vec{F}_{s,-m,n}^{(3)}(\rho_{meas}, \theta, \varphi)\sin(\theta)d\theta d\varphi \tag{a.28}$$

where $R_{sn}^{(3)}(k\rho)$ is the radial dependence of the spherical wave function whose complete expression can be found in [Hans 88, (A1.6)].

This form enables one to compute the transmission coefficients, and hence the SWE coefficients, of the AUT based on the received tangential electric field measured. The cost of computation in this case is to perform the double integral. Again, once the coefficients are known the fields can be found at any points in space outside the minimum sphere, including the far-field.

We next go away from the simple dipole as our probe. When the probe is more involved, one has to take into account the receiving coefficients of the probe as well. In this case the transmission equation between the probe and the AUT is

$$w(\rho_{meas}, \chi, \theta, \varphi) = \upsilon \sum_{\substack{smn \\ \mu}} T_{smn} e^{jm\varphi} d_{\mu m}^n(\theta)\, e^{j\mu\chi} P_{s\mu n}(k\rho_{meas}) \tag{a.29}$$

with the probe response constant

$$P_{s\mu n}(k\rho_{meas}) = \frac{1}{2}\sum_{\sigma v} C_{\sigma\mu v}^{sn(3)}(k\rho_{meas})\, R_{\sigma\mu v}^{p} \tag{a.30}$$

where,

$w(\rho,\chi,\theta,\varphi)$ is the received signal at the probe.

$e^{jm\varphi} d_{\mu m}^{n}(\theta) e^{j\mu\chi}$ are the rotation coefficients of spherical wave functions

$P_{s\mu n}(k\rho_{meas})$ expresses the probe response constant, at a point in space, to a specified mode of given amplitude.

(σ,μ,v) are mode descriptors for the probe, analogous to *s*, *m*, *n* for the AUT. Here caution is required as μ shall not be confused with the medium permeability. This notation is chosen to reflect the work of [Hans 88]

$C_{\sigma\mu v}^{sn(3)}(k\rho_{meas})$ are the translation coefficients of the spherical wave functions [Hans 88, Appendix A3]

$R_{\sigma\mu v}^{p}$ are the receiving coefficients of the probe, which are analogous to the transmission coefficients of the AUT

Similarly to the AUT, the coefficients of the probe can take are the following values:

$$\sigma = 1{,}2$$

$$\mu = -v_{max} \,..\, v_{max}$$

$$v = |\mu|$$

The maximum value of μ depends on the degree of azimuthal symmetry of the probe. However, for a probe that is relatively small and sufficiently far away from the AUT this can be approximated by $\mu = \pm 1$. This approximation will come handy in the formulations to follow. From SWE theory, one can also see that as the probe tends to get smaller, fewer modes are needed to represent the probe. The concept of a minimum sphere can be applied to the probe as well, the radius of that sphere being denoted by ρ_{prob}, in Figure 52.

In the case of a general probe, the transmission expression solution is relatively similar, yet more complex, to what has been presented previously for the dipole. The solution to that expression was proposed by [Jens 75] and [Wack 74] independently. The solution is carried out in three steps, exploiting the orthogonality the exponential function along with the finite spatial Fourier transform. For more details on the process, the reader is referenced to [Hans 88, pp.105]. The analytical solution is

$$vT_{1mn}P_{1\mu n}(\rho_{meas}) + vT_{2mn}P_{2\mu n}(\rho_{meas}) = w_{\mu m}^{n}(\rho_{meas}) \qquad \text{(a.31)}$$

with

$$w_{\mu m}^{n}(\rho_{meas}) = v\sum_{s=1}^{2} T_{smn}P_{s\mu n}(k\rho_{meas}) \qquad \text{(a.32)}$$

This equation constitutes a system with as many equations for unknowns vT_{1mn} and vT_{2mn} as there are different values for μ, the azimuthal index; thus the system has a unique solution. As previously mentioned, if the probe is sufficiently small and sufficiently far away from the AUT, the μ-index can be approximated by $\mu = \pm 1$. This is the case even if the probe does not have perfect rotational symmetry (e.g. rectangular waveguide). The probe modes $\mu = \pm 1$ will dominate if the measurement sphere is large enough, that is if the distance to the AUT is sufficiently large. When a $\mu = \pm 1$ probe is present the system takes the forms

$$vT_{1,m,n}P_{1,1,n}(\rho_{meas}) + vT_{2,m,n}P_{2,1,n}(\rho_{meas}) = w_{1,m}^{n}(\rho_{meas}) \qquad \text{(a.33)}$$

and

$$vT_{1,m,n}P_{1,-1,n}(\rho_{meas}) + vT_{2,m,n}P_{2,-1,n}(\rho_{meas}) = w_{-1,m}^{n}(\rho_{meas}) \qquad \text{(a.34)}$$

If the probe can’t be approximated by $\mu = \pm 1$, a larger system of equations must be solved. The rest of this appendix uses the mentioned approximation for the probe.

While the last form doesn't directly solve for the coefficients, it is possible to derive a solution by separation of variables, leading to the three-fold integral transform (one for each spatial components)

$$w_{\mu m}^{n}(\rho_{meas}) = \frac{2n+1}{2} \int_{\theta=0}^{\pi} w_{\mu m}(\rho_{meas}, \theta) d_{\mu m}^{n}(\theta) \sin(\theta)\, d\theta \tag{a.35}$$

$$w_{\mu m}(\rho_{meas}, \theta) = \frac{1}{2\pi} \int_{\varphi=0}^{2\pi} w_{\mu}(\rho_{meas}, \theta, \varphi) e^{-jm\varphi} d\varphi \tag{a.36}$$

$$w_{\mu}(\rho_{meas}, \theta, \varphi) = \frac{1}{2\pi} \int_{\chi=0}^{2\pi} w(\rho_{meas}, \chi, \theta, \varphi) e^{-j\mu\chi} d\chi \tag{a.37}$$

where $w(\rho_{meas}, \chi, \theta, \varphi)$ is the received signal at the probe.

To evaluate these integrals numerical integration is used, which requires some type of sampling. We note that the integrals (a.38) and (a.39) are both Fourier integrals of periodic function which may be evaluated by a Discrete Fourier Transform (DFT), and thus by the well-known Fast Fourier Transform (FFT). The expression (a.37) can also be evaluated by Fourier techniques; however, there is no periodicity in space.

To solve a problem numerically, at some point some discretization must be performed. Just as the sampling theorem applies for reconstruction of a temporal signal, the theorem applies as well in space; to resolve a mode of a certain order one must sample points in space with a separation that is small enough. That is, the physical location of the probe must be positioned precisely and acquire the tangential field. The minimal separation between two samples in θ and ϕ is denoted by Δθ and Δϕ, respectively.

Before we tackle the three integrals defined in (a.37) to (a.39), we must link the important concept of spatial sampling to the evaluation of these integrals. As the order of the mode increases the spatial variation frequency increases as well. Thus, the step Δθ and Δϕ must satisfy a spatial version of the Nyquist criterion to resolve a certain mode order. That criterion is

$$\varDelta\theta = 2\pi/(2N+1) \tag{a.38}$$

$$\varDelta\varphi = 2\pi/(2N+1) \tag{a.39}$$

Therefore, as high-order modes are needed without aliasing, the sampling must become denser. Conversely, by specifying steps in Δθ and Δϕ one can calculate the highest mode that can be resolved.

At this point suppose we have measured the tangential electric fields on the sphere with appropriate spacing to resolve a sufficient number of modes, and that we are seeking a way to evaluate the integrals (a.37) to (a.39) to retrieve the coefficients. We now tackle independently each integral. Note that the solution of (a.39) is part of the integrand in (a.38) and that similarly the solution of (a.38) is part of the integrand in (a.37). Therefore, we must solve in this order (a.39), (a.38) and then (a.37). Once (a.37) is evaluated, it is possible to solve the linear system presented in (a.33).

For measurement in χ, the probe is rotated on its axis by an angular positions separated by Δχ from $0 \leq \chi \leq 2\pi$. A direct solution of the expression (a.39), the proof is presented in [Hens 88, pp.110], is easily derived for the two harmonics[18] of the probe

$$w_1(\rho_{meas}, \theta, \varphi) = \frac{1}{2}\left\{w(\rho_{meas}, 0, \theta, \varphi) - jw(\rho_{meas}, \frac{\pi}{2}, \theta, \varphi)\right\} \tag{a.40}$$

$$w_{-1}(\rho_{meas}, \theta, \varphi) = \frac{1}{2}\left\{w(\rho_{meas}, 0, \theta, \varphi) + jw(\rho_{meas}, \frac{\pi}{2}\theta, \varphi)\right\} \tag{a.41}$$

Here only measurement in $\chi = 0$ and $\chi = \frac{\pi}{2}$ are required to solve this system. If a probe presents a larger μ-factor than $\mu = \pm 1$, only two measurements in χ are still required as it is possible to generate the larger solution system from these two orthogonal measures.

For measurement in ϕ, the probe is moved to angular positions separated by Δϕ from $0 \leq \varphi \leq 2\pi$. The angular separation is determined from the number of harmonics 2N + 1. Therefore, the number of samples to take to resolve a sufficient number of modes in ϕ is $J_\varphi \geq$

[18] Recall that we use $\mu = \pm 1$ to simplify the comprehension of these expressions.

$2N + 1$, so that $\Delta\varphi = 2\pi/J_{\varphi}$. We refer to a specific sample in ϕ as $w_{\mu}(\rho_{meas}, \theta, j\Delta\varphi)$. The ϕ integration is performed as

$$w_{\mu\{m=0,1,..,N,-N,..,-1\}}(\rho_{meas}, \theta) = IDFT\{w_{\mu}(\rho_{meas}, \theta, \{j = 0, 1, ..J_{\varphi} - 1\}\Delta\varphi)\} \quad \text{(a.42)}$$

where, IDFT is the Inverse Discreet Fourier Transform.

For measurement in θ, the solution is a bit more involved since the integrand is not periodic; θ is defined as $0 \leq \theta \leq \pi$. But with some clever manipulations the function can be expanded. Note that just as for ϕ angles the probe is moved to angular positions separated by Δθ with $J_{\theta} \geq 2N + 1$ and thus $\Delta\theta = 2\pi/J_{\theta}$. The proof for the evaluation of the expression (a.37) is not presented here since it`s cumbersome and doesn't increase the comprehension of the process; the reader can refer to [Hans 88, pp.113-116]. It suffice to say that the computation of $w_{\mu m}^{n}(\rho_{meas})$ must be carried out for all n, m and μ, which is require to solve the linear system (a.33) and find the transmission coefficients of the AUT.

Efforts were devoted to improve methods to evaluate the integral (a.37). [Jame 69] evaluate integrals using Simpson's rule for cases with low numbers of modes (N=3). For larger N, which is necessary to represents antennas with higher gain values, the fact that θ and ϕ integrals, can be carried out separately must be used. Also, since the integrand of (a.37) is not periodic, Simpson's rule or the trapezoidal rule cannot be expected to provide an exact solution. Like many numerical analyses, with a sufficient number of samples one can expect a sufficiently accurate answer. [Ludw 69] and [Wood 80] both worked on integrals using the previously mentioned techniques. A Gaussian quadrature rule leads to an exact solution of the integrals, but the samples on the sphere must be selected at specific non-equidistant values in θ, which is seen as a disadvantage. Of course the Gaussian quadrature provides exact solution only if the integrands are polynomials, the band-limited nature of the integral enables to fulfil that criterion, details are presented in [Hans 88, pp.141-142]. [Rica 72] and [Wack 75] discovered the possibility to apply Fourier transformation in θ, which is an efficient way to handle the θ integral. [Lars 80] improved the technique to reduce memory usage, which was very limited at the time; this method is now known as the Wacker-Larsen approach. Further work on reduction of the computing burden was carried out extensively in many studies, [Yagh 84], [Yagh 85], [Witt 84] and [Hess 82].

Once the $w_{\mu m}^{n}(\rho_{meas})$ values are found for $\mu = \pm 1$, one can solve for the transmission coefficients $T_{1,m,n}$ and $T_{2,m,n}$ of the AUT. These coefficients are sufficient to characterize the AUT completely. With these coefficients, one can then do some post-processing and find the field either at a finite distance from the AUT, or in the far-field, by evaluating the field expressions at a point in space. Techniques and formulations exist to derive far-field antenna parameters from the transmission coefficients when required by using the asymptotic form of the Hankel functions [Hans 88, pp.123-125].

To summarize, the objective is to solve for the SWE coefficients of an AUT from the acquired tangential electric field over a measurement sphere. The fields in space outside the minimum sphere, thus also in the FF, can be written as a weighted sum of coefficients multiplied by the spherical wave functions. By solving integrals transmission equations, which relates the transmission coefficients of the probe and the AUT, the position of the probe in space and the signal received at the probe, we can derive the SWE coefficients of our system. As a final note, some techniques can reconstruct the sources from the coefficients and find the fields inside the measurement sphere and even show the field amplitude and phase directly on the AUT [Guler 95].

Appendix B – Software Framework Layout

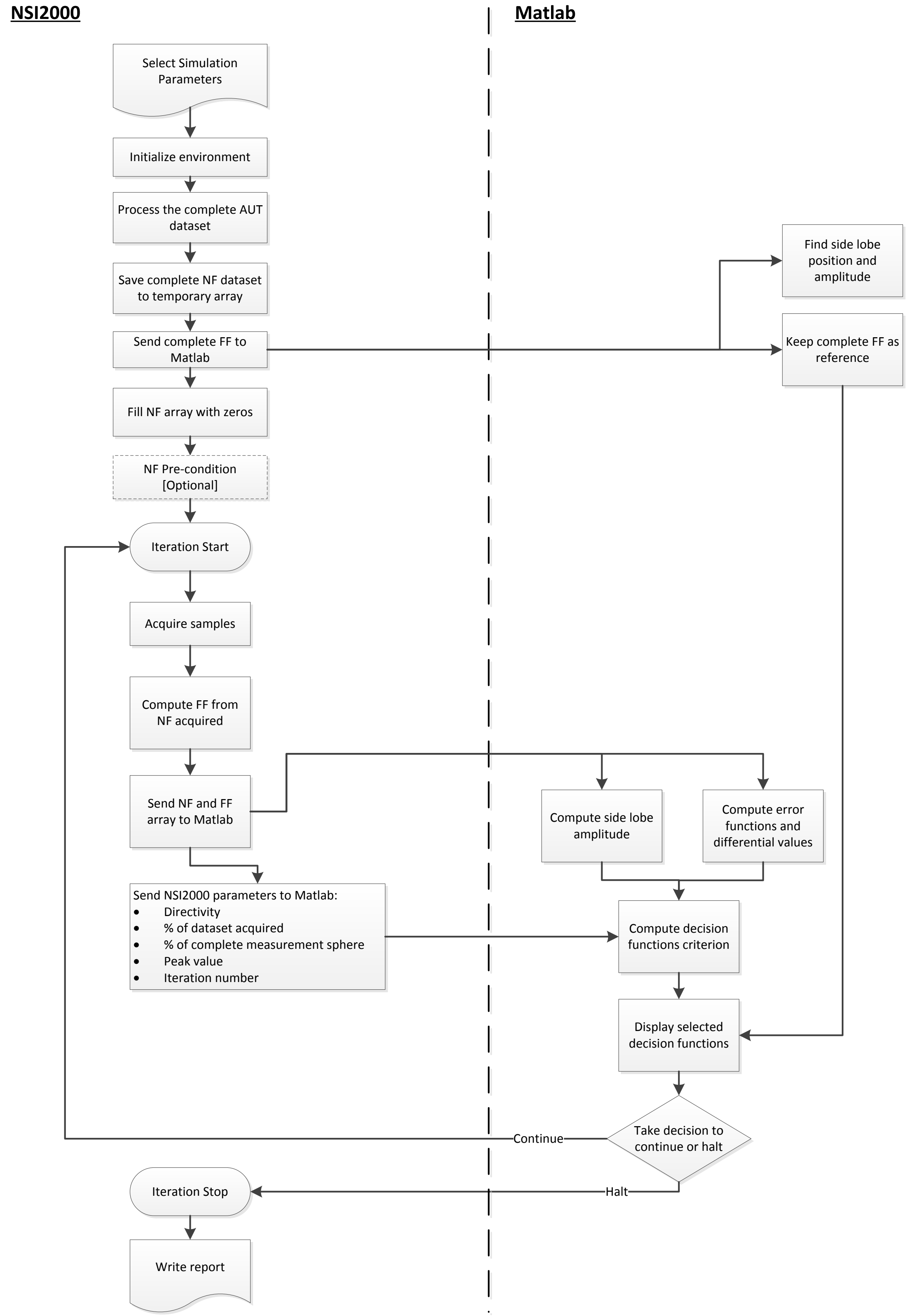

Appendix C – File Tree of Adaptive SNF Solution

```
./Adaptive SNF
├─ /AUT
│     FAN.nsi
│     ISO.nsi
│     BS.nsi
├─ / Matlab
│  ├─ /PreCond
│  │     DispPreCondResults.m
│  │     PreCond_BaseStation.m
│  │     PreCond_FanBeam.m
│  │     PreCond_ISO.m
│  │     suplabel.m
│  ├─ /Utilities
│  │     GetHVCuts.m
│  │     SideLobeFind.m
│  │     SideLobeFinder.m
│  │     SideLobeLister.m
│  └─ /Visualizer
│        DispEvolv.m
│        ExtractNF_FF.m
│        NF_Evolution.m
│        NF_Matrix_View.m
│        SideLobeTracker.m
├─ /NSI
│     AdaptiveAcquisition.bas
└─ /Results
   ├─ /Isoflux – Rule 1 (22 March 2013)
   │     WorkSpace.mat
   └─ Results.xlsx
```

Appendix D – Timing Test Results

	Description	Values				
AUT	AUT identifier	**FPA**	**SGH**	**DIP**	**FAN1**	**FAN2**
NF Pts	NF_VPTS NF_HPTS	201 151	31 121	61 31	73 37	91 46
NF Pts Tot	Number of NF points	30351	3751	1891	2701	4186
FF Pts	FF_VPTS FF_HPTS	401 401	401 401	401 401	401 401	401 401
FF Pts Tot	Number of FF points	160801	160801	160801	160801	160801
		Timing (s)				
Test 1	NSI NF processing	0.0703125	0.03125	0.015625	0.015625	0.015625
Test 2	NSI FF processing	3.976563	1.632813	1.054688	1.117188	1.609375
Test 3	Send NF to Matlab	1.585938	0.1875	0.1015625	0.15625	0.234375
Test 4	Get NF from Matlab	1.75	0.203125	0.109375	0.1484375	0.2265625
Test 5	Send FF CoPol Amp to Matlab	5.140625	5.015625	5.015625	5.046875	5.070313
Test 6	Send FF Dir to Matlab + compute diff + get result	0.0234375	0	0	0	0.0078125
Test 7	Run SidelobeFinder in Matlab on FF sent + retrieve max val	0.0234375	0.0078125	0.015625	0.0078125	0.015625
Test 8	Compute Error Function in Matlab on FF sent + retrieve max val	0.03125	0.03125	0.015625	0.015625	0.015625

Appendix E – Linear Interpolation NF Pre-Conditioning Foundations

In this appendix we settle the mathematical and geometrical foundations required to solve the following problem:

> Provided with orthogonal cuts of NF measured tangential E-field on a measurement sphere, estimate the tangential field at any other points on that same sphere.

The geometry used is presented in Figure 53. Note that only a portion of a full measurement sphere is presented for ease of representation. In an actual implementation the whole sphere is used.

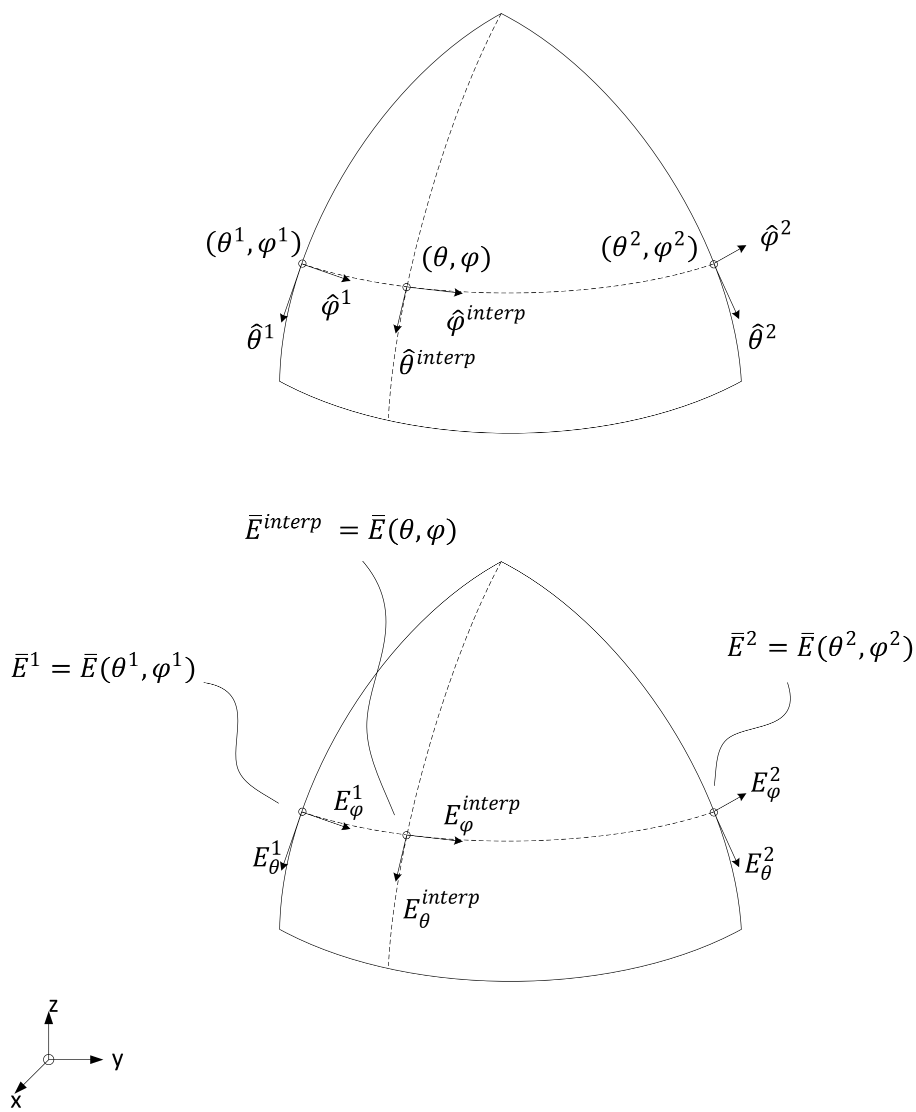

FIGURE 53 - GEOMETRY OF NF ARRAY INTERPOLATION. TOP: POINTS OF INTEREST. BOTTOM: FIELDS OF INTEREST.

The orthogonal cuts used in this work are consistent with Section 5.5 and are the following:

- Cutting the sphere at ϕ = 0°, thus letting θ go from 0° to 360°
- Cutting the sphere at ϕ = 90°, thus letting θ go from 0° to 360°

Hence, both cuts are passing through the North Pole and the equatorial cut is no acquired.

To settle the various presented points on diagram, we textually list them here:

<u>Points of interest:</u>

(θ, φ) -> Point to interpolate

(θ^1, φ^1) -> Known point 1, on cut ϕ = 0°

(θ^2, φ^2) -> Known point 2, on cut ϕ = 90°

<u>Unit vector at points of interest:</u>

$(\hat{\theta}^{interp}, \hat{\varphi}^{interp})$

$(\hat{\theta}^1, \hat{\varphi}^1)$

$(\hat{\theta}^2, \hat{\varphi}^2)$

<u>Input for the NF pre-conditioning algorithm:</u>

$(E_\theta^1, E_\varphi^1)$

$(E_\theta^2, E_\varphi^2)$

<u>Output for the NF pre-conditioning algorithm:</u>

E_θ^{interp}

E_φ^{interp}

Fields at points of interest:

$$\bar{E}^1 = \bar{E}(\theta^1, \varphi^1)$$

$$\bar{E}^1 = E_\theta^1 \hat{\theta}^1 + E_\varphi^1 \hat{\varphi}^1 = E_x^1 \hat{x} + E_y^1 \hat{y} + E_z^1 \hat{z}$$

$$E_\theta^1 = E_\theta(\theta^1, \varphi^1)$$

$$E_\varphi^1 = E_\varphi(\theta^1, \varphi^1)$$

$$E_x^1 = E_x(\theta^1, \varphi^1)$$

$$E_y^1 = E_y(\theta^1, \varphi^1)$$

$$E_z^1 = E_z(\theta^1, \varphi^1)$$

$$\bar{E}^2 = \bar{E}(\theta^2, \varphi^2)$$

$$\bar{E}^2 = E_\theta^2 \hat{\theta}^2 + E_\varphi^2 \hat{\varphi}^2 = E_x^2 \hat{x} + E_y^2 \hat{y} + E_z^2 \hat{z}$$

$$E_\theta^2 = E_\theta(\theta^2, \varphi^2)$$

$$E_\varphi^2 = E_\varphi(\theta^2, \varphi^2)$$

$$E_x^2 = E_x(\theta^2, \varphi^2)$$

$$E_y^2 = E_y(\theta^2, \varphi^2)$$

$$E_z^2 = E_z(\theta^2, \varphi^2)$$

$$\bar{E}^{interp} = \bar{E}(\theta, \varphi)$$

$$\bar{E}^{interp} = E_\theta^{interp} \hat{\theta}^2 + E_\varphi^{interp} \hat{\varphi}^2 = E_x^{interp} \hat{x} + E_y^{interp} \hat{y} + E_z^{interp} \hat{z}$$

$$E_\theta^{interp} = E_\theta(\theta, \varphi)$$

$$E_\varphi^{interp} = E_\varphi(\theta, \varphi)$$

$$E_x^{interp} = E_x(\theta, \varphi)$$

$$E_y^{interp} = E_y(\theta, \varphi)$$

$$E_z^{interp} = E_z(\theta, \varphi)$$

We next look at the two linear interpolation techniques used in this work.

Method 1 – Described in Section 5.5.2:

$$E_\theta^{interp} = linspace(E_\theta^1, E_\theta^2)$$

$$= E_\theta^1 + (E_\theta^2 - E_\theta^1)\frac{\varphi - \varphi^1}{\varphi^2 - \varphi^1}$$

$$= \left\{real\{E_\theta^1\} + (real\{E_\theta^2\} - real\{E_\theta^1\})\frac{\varphi - \varphi^1}{\varphi^2 - \varphi^1}\right\} + j\left\{imag\{E_\theta^1\} + (imag\{E_\theta^2\} - imag\{E_\theta^1\})\frac{\varphi - \varphi^1}{\varphi^2 - \varphi^1}\right\}$$

$$E_\varphi^{interp} = linspace\left(E_\varphi^1, E_\varphi^2\right)$$

$$= E_\varphi^1 + (E_\varphi^2 - E_\varphi^1)\frac{\varphi - \varphi^1}{\varphi^2 - \varphi^1}$$

$$= \left\{real\{E_\varphi^1\} + (real\{E_\varphi^2\} - real\{E_\varphi^1\})\frac{\varphi - \varphi^1}{\varphi^2 - \varphi^1}\right\} + j\left\{imag\{E_\varphi^1\} + (imag\{E_\varphi^2\} - imag\{E_\varphi^1\})\frac{\varphi - \varphi^1}{\varphi^2 - \varphi^1}\right\}$$

Note that the decomposition in real and imaginary parts is only shown to emphasise how the linear interpolation occurs on a complex number. The *linspace* function is simply the linear interpolation function used within Matlab.

Method 2 – Described in Section 5.5.3:

Decompose spherical components of each known point in Cartesian components:

$$E_{\theta}^{1} = E_{\theta_x}^{1}\hat{x} + E_{\theta_y}^{1}\hat{y} + E_{\theta_z}^{1}\hat{z}$$

$$E_{\varphi}^{1} = E_{\varphi_x}^{1}\hat{x} + E_{\varphi_y}^{1}\hat{y} + E_{\varphi_z}^{1}\hat{z}$$

$$E_{\theta}^{2} = E_{\theta_x}^{2}\hat{x} + E_{\theta_y}^{2}\hat{y} + E_{\theta_z}^{2}\hat{z}$$

$$E_{\varphi}^{2} = E_{\varphi_x}^{2}\hat{x} + E_{\varphi_y}^{2}\hat{y} + E_{\varphi_z}^{2}\hat{z}$$

$$E_{x}^{1} = E_{\theta_x}^{1} + E_{\varphi_x}^{1}$$

$$E_{y}^{1} = E_{\theta_y}^{1} + E_{\varphi_y}^{1}$$

$$E_{z}^{1} = E_{\theta_z}^{1} + E_{\varphi_z}^{1}$$

$$E_{x}^{2} = E_{\theta_x}^{2} + E_{\varphi_x}^{2}$$

$$E_{y}^{2} = E_{\theta_y}^{2} + E_{\varphi_y}^{2}$$

$$E_{z}^{2} = E_{\theta_z}^{2} + E_{\varphi_z}^{2}$$

Interpolate Cartesian components separately:

$$E_{x}^{interp} = linspace(E_x^1, E_x^2)$$

$$= E_x^1 + (E_x^2 - E_x^1)\frac{\varphi - \varphi^1}{\varphi^2 - \varphi^1}$$

$$E_{y}^{interp} = linspace(E_y^1, E_y^2)$$

$$= E_y^1 + (E_y^2 - E_y^1)\frac{\varphi - \varphi^1}{\varphi^2 - \varphi^1}$$

$$E_{z}^{interp} = linspace(E_z^1, E_z^2)$$

$$= E_z^1 + (E_z^2 - E_z^1)\frac{\varphi - \varphi^1}{\varphi^2 - \varphi^1}$$

<u>Project back the Cartesian components to spherical components:</u>

$$E_\theta^{interp} = \cos\theta\cos\varphi\, E_x^{interp} + \cos\theta\sin\varphi\, E_y^{interp} - \sin\theta\, E_z^{interp}$$

$$E_\varphi^{interp} = -\sin\varphi\, E_x^{interp} + \cos\varphi\, E_y^{interp}$$

With this approach a radial component E_ρ^{interp} will emerge. In this case, we simply ignore this component, thus assigning $E_\rho^{interp} = 0$. This procedure is believed to create a systematic error. Again, the *linspace* function is simply the linear interpolation function used within Matlab.